ERDC/GSL TR-02-16

US Army Corps
of Engineers®
Engineer Research and
Development Center

Discrimination and Identification of UXO by Geophysical Inversion of Total-Field Magnetic Data

Stephen D. Billings, Leonard R. Pasion,
and Douglas W. Oldenburg

September 2002

Geotechnical and Structures
Laboratory

The contents of this report are not to be used for advertising, publication, or promotional purposes. Citation of trade names does not constitute an official endorsement or approval of the use of such commercial products.

The findings of this report are not to be construed as an official Department of the Army position, unless so designated by other authorized documents.

PRINTED ON RECYCLED PAPER

ERDC/GSL TR-02-16
September 2002

Discrimination and Identification of UXO by Geophysical Inversion of Total-Field Magnetic Data

by Stephen D. Billings, Leonard R. Pasion, Douglas W. Oldenburg

Geophysical Inversion Facility
Department of Earth and Ocean Sciences
University of British Columbia
Vancouver, B.C., V6T 1Z4, Canada

Final report

Prepared for U.S. Army Corps of Engineers
Washington, DC 20314-1000

Monitored by Geotechnical and Structures Laboratory
U.S. Army Engineer Research and Development Center
3909 Halls Ferry Road
Vicksburg, MS 39180-6199

Contents

List of Figures

Preface

The study documented herein was undertaken as part of the Work Unit "Innovative Geophysical Technologies for Enhanced Buried Unexploded Ordnance (UXO) Discrimination" (AF25, 6.2) and funded by the U.S. Army Engineer Research and Development Center (ERDC), Vicksburg, MS, under the Environmental Quality Technology (EQT) Program. Dr. Dwain K. Butler, Geotechnical and Structures Laboratory (GSL), is Principal Investigator for the work unit, Dr. John M. Cullinane, Environmental Laboratory (EL), is EQT Program Manager, and Dr. Ernesto R. Cespedes, EL, is UXO Focus Area Manager for EQT. Dr. David W. Pittman was Acting Director, GSL. The work was performed at the University of British Columbia (UBC), Vancouver, British Columbia, Canada. Funding of the UBC effort was by means of Army Research Office Grant 41262-EV. Dr. Russell Harmon, Terrestrial Sciences Program Manager, administered the UBC grant.

Dr. Stephen D. Billings, Mr. Leonard R. Pasion, and Dr. Douglas W. Oldenburg, UBC, performed the work during the period 1 April 2001 through 31 March 2002. The work exploits a forward model, based on the multipole expansion of the induced magnetic field in a spheroid model of UXO, in an inversion algorithm to recover the parameters of a spheroid model fit to measured total field magnetic data. Prolate spheroids are proposed as an approximate model for UXO by a several authors (McFee 1989; Altshuler 1996; Butler et al. 1998). The total magnetic field inversion algorithm is applied to datasets from Guthrie Road, Montana, and Former Fort Ord, California. Based on results on the inversions, discrimination and identification approaches are proposed. Application of the discrimination and identification algorithms to total field magnetic data illustrates the potential to significantly reduce the cost of UXO cleanup by discrimination of false alarm anomalies from UXO anomalies.

At the time of publication of this report, Dr. James R. Houston was Director, ERDC. Commander and Executive Director of ERDC was COL John W. Morris III, EN.

1 Introduction

Unexploded ordnance pose a significant public safety hazard in many parts of the world. They occur on or near the surface and down to depths of several meters below the ground. One source of UXO's are armed conflicts both old and more recent in regions such as Europe (World Wars I and II), South-East Asia, Afghanistan, Yugoslavia and parts of Africa. They are also a significant problem in countries such as Canada and the United States, where they are present in areas used for military training and firing ranges; largely as vestiges of World War II and the Cold War. It is estimated that 15 million acres of the United States are contaminated by UXO (FAC, 1996), with a clean-up time-frame in the decades and a staggering cost estimate, using existing technology, in the tens to hundreds of billions of dollars (GAO, 2001).

The most well established techniques for ordnance detection are magnetics and electromagnetics (Bulter et al., 1998). These methods are very effective at locating buried metallic objects such as UXO. However, discriminating between intact UXOs and uninteresting objects such as metallic debris and shrapnel is a significant challenge (Bulter et al., 1998). Often little or no effort is invested in discrimination and, consequently, many holes are excavated for each ordnance item recovered. For example, Putnam (2001) reports that from 49,521 anomalies excavated at Kaho'olawe, Hawaii, only 3% (or 1,486) turned out to be UXO. In this report we analyze magnetics data collected at Guthrie Road, Helana Valley, Montana (Youmans and Daehn, 1999). 840 holes were excavated with 83 UXOs recovered, thus there was a 10% success rate. It is perhaps a reflection of the state of our ability to discriminate that this survey was considered a success by all parties involved.

The simplest form of discrimination is to threshold the collected data in some way (for magnetics this is usually achieved by first calculating the analytic signal and then thresholding, Roest et al. (2001)). As the threshold level is decreased, the number of items that need to be excavated increases. As demonstrated by the Ordnance Detection and Discrimination Study at the Former Fort Ord (Asch and Staes, 2001), for such techniques to yield a high probability of detection, a very high false alarm rate results.

Location of UXOs involves the successful detection and identification of compact metallic objects. Therefore, a better method for discrimination is to parameterize the characteristics of the target in some way (e.g. by its location, orientation, shape, size and material properties) and develop a good forward model that allows predicted data to be generated from a given target realization. Inversion can then be used to find the set of target parameters that best fits the data. The target parameters are then used to make decisions regarding discrimination (UXO versus non-UXO) and identification (what is the ordnance type).

A previous report (Pasion and Oldenburg, 2001) considered the development of an inversion methodology for time-domain electromagnetic data. In this report, we consider the development of a methodology for total-field magnetics data. Previous work in this area has been conducted by (amongst others) the Canadian Defence Research Establishment (McFee, 1989) and the Naval Research Laboratory (Nelson et al., 1998) and private companies.

Spheroids have been proposed as an approximate parameterization of ordnance by several authors (McFee, 1989; Altshuler, 1996; Bulter et al., 1998). While the spheroid

does not capture the top-bottom asymmetry of many ordnance items, close agreement between observed anomalies over test stands and spheroid fits have been demonstrated (McFee, 1989; Bulter et al., 1998). Furthermore, the magnetic anomaly from a solid spheroid has been shown to be very similar to a hollow spheroid (Altshuler, 1996). Therefore, we will use solid spheroids as the basis of our magnetic modelling of UXO's.

The response of a spheroid (in fact any compact body) can be decomposed into a series of moments by a multipole expansion (Stratton, 1941). The response of the dipole component dominates the anomalies caused by most buried ordnance due to the rapid falloff with distance of the other components. Consequently, the main inversion routine developed in this report attempts to recover the dipole moment and position that best matches an observed anomaly. The recovered dipole moment is then used to rank items according to the likelihood they are UXO. We prefer such a ranking over a definitive statement such as ordnance or non-ordnance because it is not possible to make such a black and white distinction.

The recovered dipole moment can also be used for ordnance identification. There is some ambiguity in this process because the dipole moment is the product of magnetization with volume. Due to self-demagnetization effects the magnetization can change significantly as the orientation of the body relative to the Earth's field changes. Thus orientation can be traded with volume to produce the same or similar dipole moment. By recognizing that there are a finite number of ordnance types present in an area (we build up a library), this ambiguity can be reduced significantly.

To attempt to constrain the orientation we develop two further inversion routines. The first uses the octupole component of the spheroid, and finds the optimum orientation and fit for each of the items in our library. That item with the best fit is assumed to be the source of the anomaly. The second method aims to recover the dipole and quadrupole moments of an arbitrary axially symmetric body.

No inversion methodology would be complete without an analysis of the uncertainties in the recovered parameters. The last section of the report considers the development of a linearized error analysis. We also investigate the distribution of the residuals so that we can test our assumption of Gaussian statistics.

2 Magnetic field of a spheroid

The forward modelling task may be stated as follows; calculate the magnetic anomaly at the arbitrary point $(\hat{x}, \hat{y}, \hat{z})$ given a spheroid of diameter a, aspect ratio e (i.e. $length = ae$) and permeability μ oriented at an angle of θ degrees to the horizontal with an azimuth of ϕ degrees clockwise from North, at a depth z below the surface and at the horizontal position (x, y). The geometry of this situation is shown in Figure 1. Full characterization of the anomaly caused by a spheroid requires the Earth's field plus the eight parameters $(x, y, z, \theta, \phi, a, e, \mu)$. For the Earth's field we use geographical coordinates; $\mathbf{B_o} = (B_{ox}, B_{oy}, B_{oz})$, i.e. x is positive to the East, y is positive to the North and z is positive upwards. Note that this differs from the definition used to specify the International Geomagnetic Reference Field (IGRF) where x is positive to the North, y is positive to the East and z is positive downwards.

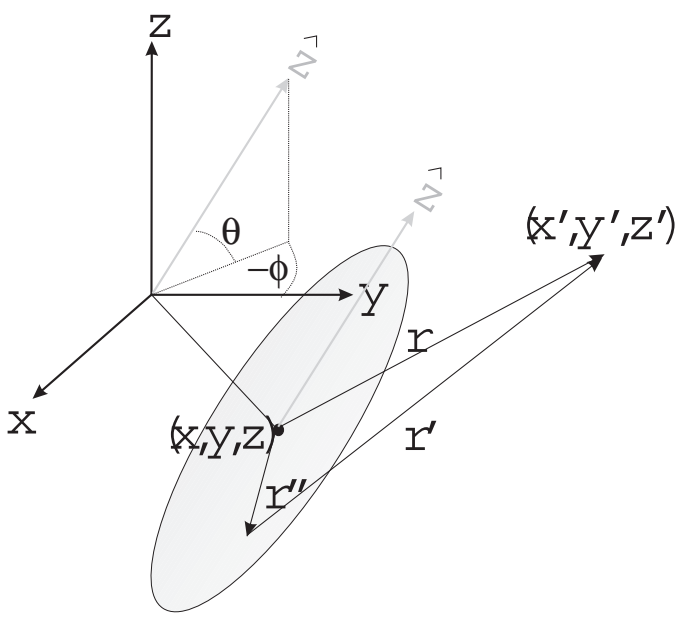

Figure 1: Geometry for modelling the response of a spheroid.

The magnetic anomaly of a buried ferrous item arises from both remnant $\mathbf{M}_{rem}$ and induced magnetization $\mathbf{M}_{in}$; the total magnetization $\mathbf{M}$ is then

$$\mathbf{M} = \mathbf{M}_{rem} + \mathbf{M}_{in} \tag{1}$$

Remnant magnetism is present even in the absence of an inducing field and is due to magnetic moments being locked into alignment once the steel casing cools to below the Curie temperature in the presence of an external field. We will discuss this type of magnetism latter but for now we will concentrate on the induced magnetism that arises because magnetic domains in a ferrous material tend to align with the direction of the Earth's field. The ease with which the moments align, and hence the strength of the magnetism, depends on the magnetic permeability of the steel. For a compact body such as a spheroid, demagnetization effects become important. This phenomena refers

to the extent that the induced field is reduced due to the shape of the spheroid. It arises due to the boundary conditions that the field must satisfy across a discontinuity in magnetic permeability. A solution of the boundary value problem (Stratton, 1941) shows that the demagnetization factors are

$$F_i = \frac{\mu_r - 1}{1 + \alpha_i(\mu_r - 1)/2} \tag{2}$$

where μ_r is the relative permeability ($\mu = \mu_r \mu_o$, where $\mu_o = 4\pi \times 10^{-7}$ H/m is the permeability of free space) and the α_i's are factors which depend on the shape of the spheroid (see Appendix A). Once the relative permeability exceeds a few hundred units, the induced magnetization becomes virtually independent of susceptibility. This can easily be seen from Equation 2 with large μ_r because then

$$F_i \approx \frac{2}{\alpha_i} \tag{3}$$

This allows us to eliminate μ_r from our calculations because steel typically has susceptibilities of several hundred to over a thousand (Lide, 2001).

The demagnetization factors, together with the Earth's field $\hat{\mathbf{B}}_\mathbf{o}$ (in spheroid centered coordinates), determine the strength of the induced magnetization,

$$\hat{\mathbf{M}}_{in} = \mu_o^{-1} \mathbf{F} \hat{\mathbf{B}}_\mathbf{o} \tag{4}$$

where we have written $\mathbf{F}$ as a 3×3 diagonal matrix with (F_2, F_2, F_3) along the diagonal (remember $F_1 = F_2$). An important consequence of demagnetization is that the induced magnetism can change significantly with orientation. For instance, with $e = 4$ we find $F_2 = 2.1$ and $F_3 = 12.7$, so that the magnetization when the spheroid semi-major axis is aligned with the field is approximately 6 times greater than when it is perpendicular.

Equation 4 returns $\hat{\mathbf{M}}_{in}$ in spheroid centered coordinates and assumes $\hat{\mathbf{B}}_\mathbf{o}$ is also spheroid centered. To use geographical coordinates we utilize the Euler rotation tensor

$$\mathbf{A} = \begin{bmatrix} \cos\psi & -\sin\psi & 0 \\ \sin\theta\sin\psi & \sin\theta\cos\psi & \cos\theta \\ \cos\theta\sin\psi & \cos\theta\cos\psi & -\sin\theta \end{bmatrix} \tag{5}$$

to rotate $\mathbf{B_o}$ to spheroid centered coordinates and then use its inverse $\mathbf{A}^T$ to rotate $\hat{\mathbf{M}}_{in}$ to geographical coordinates,

$$\mathbf{M}_{in} = \mu_o^{-1} \mathbf{A}^T \mathbf{F} \mathbf{A} \mathbf{B_o} \tag{6}$$

With this uniform magnetization, the magnetic field of the spheroid is given by the expression

$$\mathbf{B} = \frac{1}{4\pi} \int_S \frac{1}{r'} \mathbf{M}_{in} \cdot \mathbf{dS} \tag{7}$$

where r' is the distance from the source to the observation point (Figure 1). An exact solution of this equation using prolate spheroidal harmonics is known (Stratton, 1941) but we chose to use a multipole expansion; the details can be found in Appendix A and McFee (1989). The first non-zero moment is the dipole $\mathbf{m}$ which is given by

$$\mathbf{m} = V \mathbf{M}_{in} = \frac{\pi}{6} e a^3 \mathbf{M}_{in} \tag{8}$$

where V is the volume of the spheroid. The magnetic field from the dipole term is then

$$\mathbf{B} = \frac{\mu_o}{4\pi r^3}\left(\frac{3}{r^2}[\mathbf{x}\cdot\mathbf{m}]\mathbf{x} - \mathbf{m}\right) \tag{9}$$

The octupole is the next non-zero moment and is a rank 3 tensor with 27 components. Symmetry reduces the number of independent components to 6. The specification of the octupole term is quite complicated, so we leave the details to Appendix A and just note that its field dies off as r^{-5}.

The rapid falloff of the octupole term with distance means that once the sensor distance exceeds a few body lengths, the field is essentially dipolar. For example, Figure 2a plots the dipole and octupole fields from a spheroid model of a 105-mm ordnance ($a = 0.105$ m, $e = 3.7$) orientated at 45^o to the vertical, along horizontal lines at a height of ae and $2ae$ above the ordnance. The responses are normalized by the maximum dipole response at that height. At a height of ae the peak of the octupole term is a little over 15% of the peak of the dipole term. For the height $2ae$ the octupole peak is less than 5% the size of the dipole peak. Figure 2b shows how this ratio rapidly decreases with increasing height above the ordnance.

Considering that real magnetic profiles are contaminated by noise, observing the octupole response in the presence of the dipole response will generally be very difficult. It may be possible when the sensor is very close to the ordnance, or when the noise levels are low and the spatial positioning extremely accurate. We now examine the consequence of the dipolar nature of the observed fields on both discrimination and identification.

Discrimination using magnetometry

The induced dipole moment of a sphere is constrained to lie in the direction of the applied field. On the other hand, the angle the induced dipole moment of a spheroid makes with the Earth's field will vary with its orientation. The angle ψ between the induced moment and the applied field will be (see Appendix B)

$$\psi = \arccos\left[\frac{F_2\sin^2\theta + F_3\cos^2\theta}{\sqrt{F_2^2\sin^2\theta + F_3^2\cos^2\theta}}\right] \tag{10}$$

where θ is the angle of the spheroid semi-major axis with the Earth's field and F_2 and F_3 are the demagnetization factors of the spheroid. In Figure 3a we show the variation in the angle ψ as the orientation θ changes for a spheroid with an aspect-ratio of 5. The angle ψ achieves a maximum value that depends on the shape of the spheroid. For a given aspect ratio, the spheroid orientation θ that results in the maximum value for ψ is (see Appendix B)

$$\theta = \arctan\left(\sqrt{\frac{F_3^3 + F_3F_2^2 - 2F_2F_3^2}{F_2^3 + F_2F_3^2 - 2F_3F_2^2}}\right) \tag{11}$$

The maximum angle for a given aspect ratio is then obtained by substituting Equation (11) into (10). The variation of this maximum angle with shape is shown in Figure 3b. Most UXO's have eccentricities between 3 and 7, so that 55^o is an upper bound on the angle. This suggests a possible method for discrimination (Altshuler, 1996).

When an ordnance hits the ground but does not explode, the impact is usually sufficient to cause shock demagnetization; the shock of impact causes magnetic domains

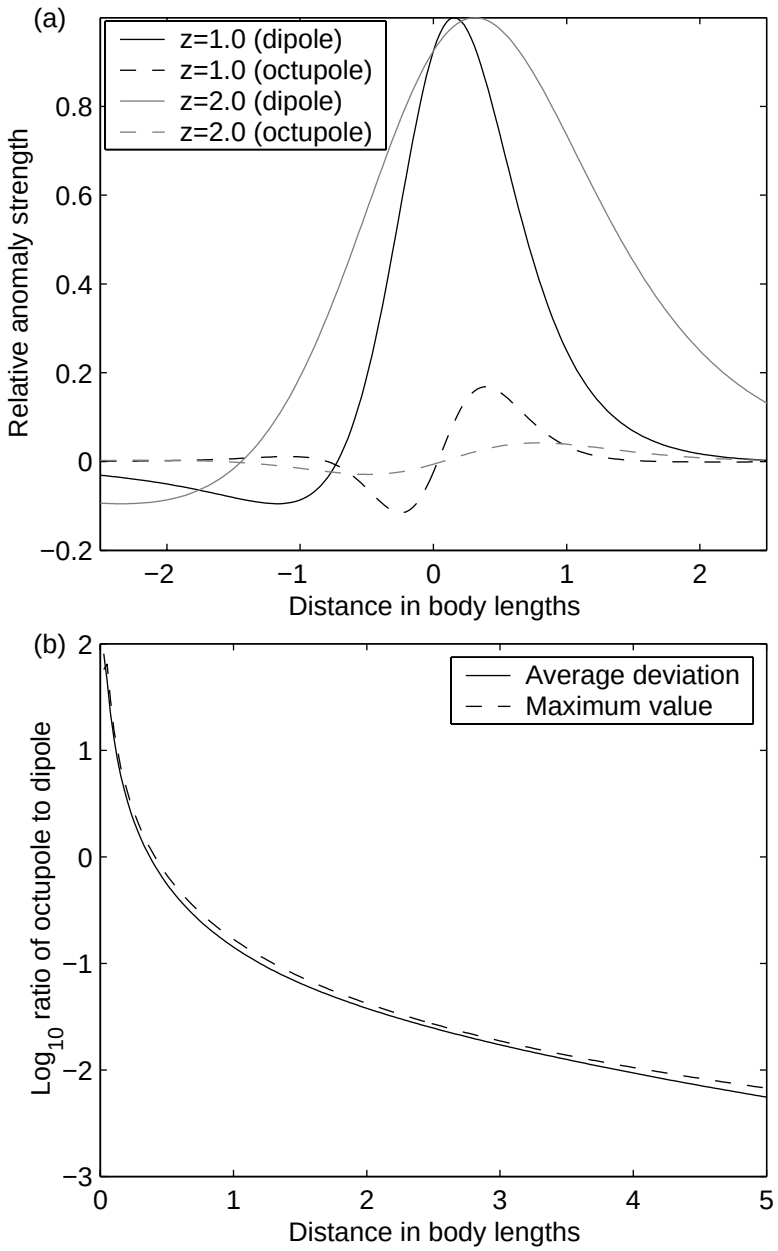

Figure 2: (a) Dipole and octupole terms at one and two body lengths distance; (b) Log_{10} of the ratio of the octupole to dipole terms for a 105-mm projectile at 45^o inclination

within the ordnance to become randomly aligned, thus erasing any remnant magnetization. On the other hand, when the ordnance explodes, the shrapnel is heated, deformed and cooled in the presence of the Earth's field and can acquire permanent magnetism. Putting all of the above together, it is conjectured that ordnance should not have a dipole moment that exceeds an angle of 60^o from the Earth's field. The success of this method of discrimination in reducing false alarms has been demonstrated in Nelson et al. (1998). However, they did note that subsequent events (such as lightning strikes)

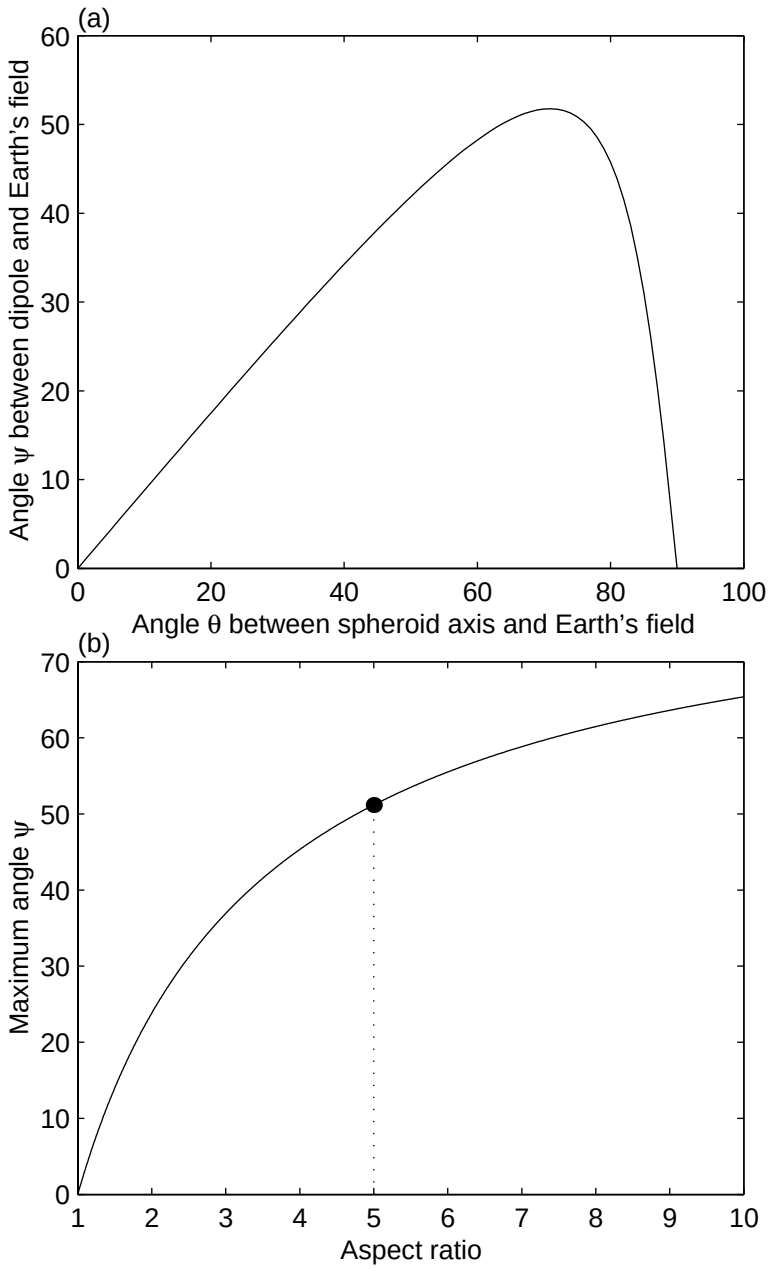

Figure 3: (a) Change in the moment angle as the orientation varies for an aspect ratio of 5; and (b) Maximum angle between the induced dipole moment of a spheroid and the Earth's field

can cause the ordnance to acquire a remnant magnetization and hence degrade the performance of the discrimination method. Also, the assumption that ordnance are fully demagnetized on impact may be violated in practice. We shall return to this point later, but for now assume that the initial conjecture is valid.

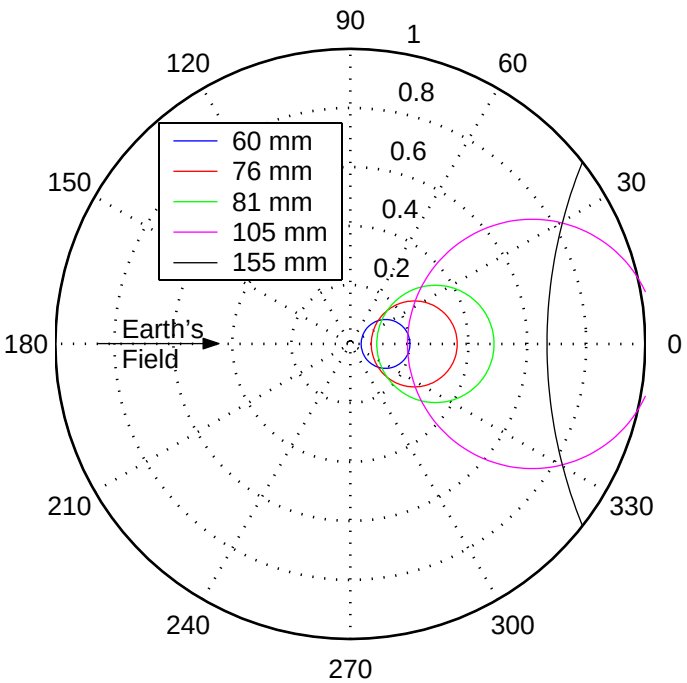

Figure 4: Magnitude of dipole moment (Am^2) and angle from Earth's field for 60, 76, 81, 105 and 155-mm projectiles

Ordnance identification using magnetometry

We now turn to the issue of identifying (or classifying) ordnance items from their dipole field. For a given spheroid, the induced dipole moment will be dependent on the angle θ that the spheroid axis makes with the Earth's field. There is no azimuthal dependence due to the spheroid's symmetry. By varying the orientation θ we are able to trace the change in dipole magnitude and angle with respect to the applied field. Figure 4 shows these curves as polar plots for five different ordnance items; a 60-mm mortar, a 76-mm projectile, an 81-mm mortar, a 105-mm projectile and a 155-mm projectile. Fitting a dipole to observed data will produce a single point in this polar plot that needs to be matched to an ordnance item. The curves for the 76-mm projectile and the 81-mm mortar are very similar in certain parts of the plot, indicating that discriminating between these items may be very difficult. Further, certain orientations lead to identical dipole moments of both these items to the 60-mm mortar and the 105-mm projectile.

The analysis in the last paragraph indicates that there can be ambiguity in identification using magnetometry. This fact is rigorously established in Appendix C where it is shown that for a given spheroid at a particular orientation, there are an infinite number of other spheroids that could have produced the same dipole moment. For example, Figure 5 and Table 1 show the family of spheroids that can produce the same dipole moment as a 105-mm projectile orientated at 45^o to the Earth's field. The 90-mm projectile lies very close to this curve emphasizing the difficulty in separating these two items. The folding over of this curve to encompass spheroids of larger dimension is of more concern to classification; the 155-mm lies quite close to this branch of the curve.

There is also a family of oblate spheroids that could produce the same dipole moment; as could objects of different shapes. This inherent ambiguity has a significant impact on the methods we develop for ordnance classification in the remainder of this report.

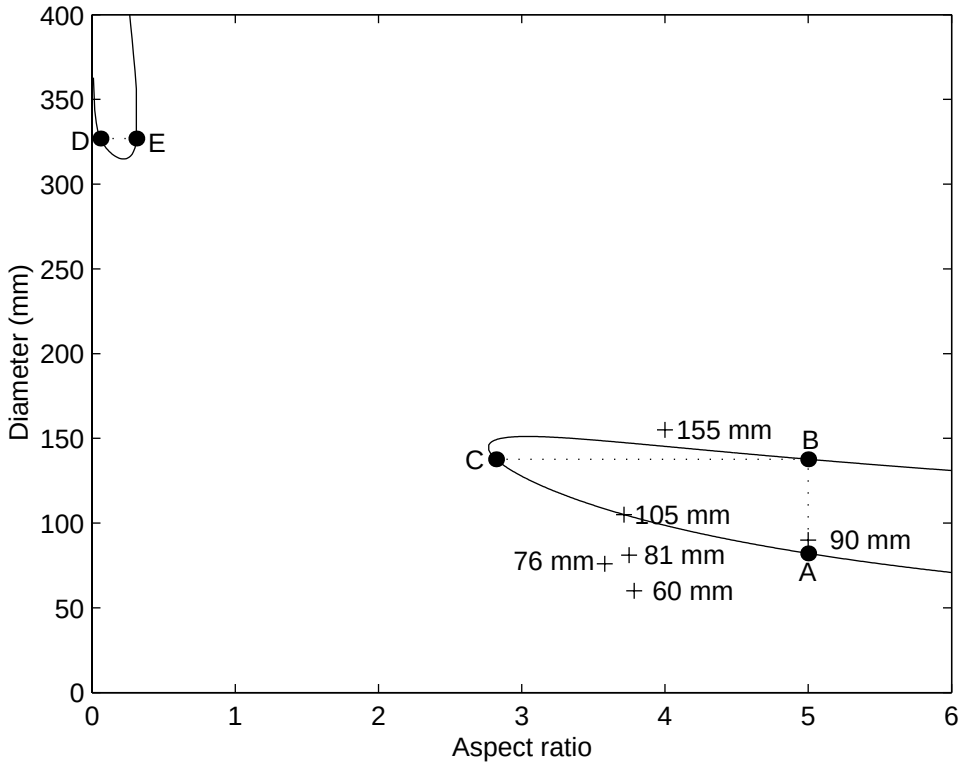

Figure 5: Spheroid dimensions that can produce the same dipole as a 105-mm shell at 45^o inclination to the Earth's field. The dimensions and orientation angles corresponding to the labelled points are shown in Table 1.

	Diameter (mm)	**Aspect ratio**	**Angle (degrees)**
A	82	5	40.5
B	138	5	84.0
C	138	2.82	57.2
D	327	0.06	53.4
E	327	0.31	33.4

Table 1: Spheroid dimensions, and their angles relative to the Earth's field, that produce the same dipole moment as a 105-mm projectile at 45^o inclination.

3 Inversion method for parameter estimation

The previous section demonstrated that, in many situations, it would be difficult to recover more than the dipole component of a spheroid's magnetic anomaly. Therefore, rather than attempting a direct inversion for the spheroid location and dimension, we apply a two-step procedure:

1. Invert for the best-fitting dipole moment and location;
2. Use the recovered dipole moment for discrimination and ordnance identification.

Due to possible difficulties in properly removing the regional and local geologically derived fields from a magnetic survey, we also allow for a dc-shift in our dipole model; this means that seven parameters are required to characterize each anomaly.

Inversion goal: Find the location $\mathbf{x} = (x, y, z)$, dipole moment $\mathbf{m} = (m_x, m_y, m_z)$ and dc-shift d, that produces the best fit to a set of N total-field observations, $\{d^{obs}(\mathbf{x}_i), i = 1, \ldots, N\}$.

We follow the usual convention in inverse problems and use $\mathbf{m}$ to specify the seven model parameters (it should be clear from the context whether $\mathbf{m}$ refers to the model parameters or the dipole moment). We formulate the inverse problem as a weighted, least-squares optimization procedure where the goal is to solve

$$\min_{\mathbf{m} \in \Re^n} \phi(\mathbf{m}) \tag{12}$$

The objective function is

$$\phi(\mathbf{m}) = \frac{1}{2}(F(\mathbf{m}) - \mathbf{d}^{obs})^T W (F(\mathbf{m}) - \mathbf{d}^{obs}) \tag{13}$$

where $F(\mathbf{m})$ is the forward model that produces the predicted data, $\mathbf{d}^{obs}$ is the observed data and W is the data-weighting matrix (ideally the data weighting matrix is the inverse covariance matrix of the errors). We assume independent, gaussian errors, so that the data-weighting matrix is diagonal with entries $W_{ii} = 1/\sigma_i^2$. The objective function may then be rewritten as

$$\phi(\mathbf{m}) = \frac{1}{2} \sum_{i=1}^{N} \left[\frac{F_i(\mathbf{m}) - \mathbf{d}_i^{obs}}{\sigma_i} \right]^2 = \frac{1}{2} \sum_{i=1}^{N} r_i(\mathbf{m})^2 \tag{14}$$

where $r_i(\mathbf{m})$ is the i-th normalized residual, and we are assuming that there are N observations.

Inversion method

We use the interior-reflective Newton method (Branch et al., 1999) to find the best fitting model parameters. The algorithm is a trust region method which means that the vector $\mathbf{s}_k$ that updates the current model, i.e.,

$$\mathbf{m}_{k+1} = \mathbf{m}_k + \mathbf{s}_k \tag{15}$$

is chosen from a quadratic model of the objective function within a region where this model can be trusted (hence the term trust region method). A quadratic approximation to $\phi(\mathbf{m})$ is

$$\phi(\mathbf{m}_k + \mathbf{s}_k) \approx \phi(\mathbf{m}_k) + \nabla\phi(\mathbf{m}_k)\mathbf{s}_k + \frac{1}{2}\mathbf{s}_k^T\nabla^2\phi(\mathbf{m}_k)\mathbf{s}_k \tag{16}$$

For a least squares problem we have

$$\nabla\phi(\mathbf{m}) = J^T(\mathbf{m})\mathbf{r}(\mathbf{m}) \tag{17}$$

where J is the Jacobian matrix which expresses the gradient of the residuals with respect to each model parameter,

$$J_{ij}(\mathbf{m}) = \frac{\partial r_i(\mathbf{m})}{\partial m_j} \tag{18}$$

and the Hessian matrix, H, is given by

$$H(\mathbf{m}) = \nabla^2\phi(\mathbf{m}) = J^T(\mathbf{m})J(\mathbf{m}) + \sum_{i=1}^{N}\mathbf{r}_i(\mathbf{m})\nabla^2\mathbf{r}_i(\mathbf{m}) \tag{19}$$

The Hessian can be difficult to calculate because it requires second-order derivatives. In least-squares problems a Gauss-Newton approximation is often used, whereby the second term in the above equation is ignored. This is a good approximation when the residuals are small and means that the Hessian can be obtained essentially for free once the Jacobian has been calculated.

The trust region method involves finding the $\mathbf{s}$ (we drop the subscripts denoting iteration number and the dependence on $\mathbf{m}$ for clarity), that satisfies

$$\min\left\{\frac{1}{2}\mathbf{s}^T J^T J\mathbf{s} + \mathbf{s}^T J^T\mathbf{r}\right\} \quad \text{such that} \quad \|D\mathbf{s}\| \leq \Delta \tag{20}$$

where D is a diagonal scaling matrix and Δ is a positive scalar that controls the trust-region size. Without the trust region constraint the solution of the above equation can be found from the normal equations

$$J^T J\mathbf{s} = -J^T\mathbf{r} \tag{21}$$

The usual trust-region approach is the Levenburg-Marquart algorithm (Marquardt, 1963) where we solve

$$(J^T J + \lambda I)\mathbf{s} = -J^T\mathbf{r} \tag{22}$$

The positive parameter λ ensures that the solution meets the constraint $\|D\mathbf{s}\| \leq \Delta$ and also improves the condition number of the normal equations.

Instead of minimizing Equation (20) over the full space, the algorithm we use minimizes over a two-dimensional subspace, span$(\mathbf{s}_1, \mathbf{s}_2)$. The first basis of the subspace is chosen as the steepest descent direction

$$\mathbf{s}_1 = -J^T \mathbf{r} \tag{23}$$

and the second is obtained by applying preconditioned conjugate gradients (PCG) to Equation (21). The PCG iterations are terminated when a negative curvature direction is discovered, i.e.,

$$\mathbf{s}_2^T J^T J \mathbf{s}_2 < 0 \tag{24}$$

or until the residual is sufficiently small; this would be an approximate Gauss-Newton step. The philosophy behind the method is to force global convergence (by the steepest descent or negative curvature) while still achieving rapid local convergence (by the Gauss-Newton step).

Bounds on model parameters

The Interior-reflective Newton Method allows bounds to be placed on the model parameters by the user if they are required. We typically impose bounds on the spatial location of the dipole, e.g.

$$-2 < x < 2,\ -2 < y < 2 \text{ and } -4 < z < 0 \tag{25}$$

but do not bound the dipole moment or dc-shift. With lower and upper bounds of $[l_i, u_i]$, the minimization problem of Equation (12) is changed to

$$\min_{\mathbf{m} \in \Re^n} \{\phi(\mathbf{m}) :\ l_i \leq m_i \leq u_i\} \tag{26}$$

This constrained minimization problem can be solved using a modification of the formulation presented above (Branch et al., 1999).

Starting model

Due to the possible presence of local minima it is important to obtain a good first guess of the model parameters. To achieve this goal, we use the approach of McFee and Das (1986), whereby the dipole parameters are analytically obtained from the z-component of the vector field. Typically, the data available comprise the total-field and we first need to estimate the z-component. Most anomalies from ordnance have peak amplitudes of less than 1,000 nT, whereas the Earth's field is on the order of 50,000 nT. The anomalous total field ΔB_t is then approximately,

$$\Delta B_t \simeq \alpha_x \Delta B_x + \alpha_y \Delta B_y + \alpha_z \Delta B_z \tag{27}$$

where $\boldsymbol{\alpha} = (\alpha_x, \alpha_y, \alpha_z)$ is a unit vector in the direction of the Earth's field and $\boldsymbol{\Delta B} = (\Delta B_x, \Delta B_y, \Delta B_z)$ is the vector magnetic anomaly. Almost all of the continental USA and Canada has inclinations exceeding 60^o so that $\alpha_z > 0.85$ and to a first approximation

$$\Delta B_z \simeq \frac{\Delta B_t}{\alpha_z} \tag{28}$$

In regions where the z-component of the field is not so dominant, ΔB_z can be obtained from ΔB_t using well known Fourier transformation techniques (Blakely, 1996).

The McFee and Das (1986) technique involves first locating the maximum and minimum values of the field. Then

- The line joining these two points gives the azimuth of the dipole;
- The distance between the two points is related to the depth of the dipole;
- The locations of the extremum and their relative amplitude can be used to infer the horizontal location (assumed to lie on the line joining the points);
- The relative amplitudes of the extremum are related to the dipole dip angle;
- The maximum anomaly amplitude is proportional to the dipole magnitude; and
- Comparing the fit of the dipole to the observed data, estimates the dc-shift.

For a nearly vertical dipole there is only a well defined maximum (or minimum). In that case, the maximum gives the horizontal location, the half-width relates to the depth and the maximum amplitude scales with the magnitude of the vertical dipole.

Data weighting matrix

For the least-squares data fitting, we weight each data-point d_i^{obs}, with an estimate of the standard deviation at that point, σ_i, through the data-weighting matrix,

$$W_{ii} = \frac{1}{\sigma_i^2} = \frac{1}{(\epsilon + \gamma |d_i^{obs}|)^2} \tag{29}$$

The parameter γ is a percentage error that down-weights the influence of the large data values; typically we chose $1\% \leq \gamma \leq 5\%$. The parameter ϵ ensures that the denominator in the above equation does not get too close to zero when d_i^{obs} approaches zero; typically we choose $\epsilon \sim 1$ nT.

Model parameter scaling

If different model parameters have significantly different scale lengths and typical values (e.g. position ~ 1 m; dipole moment ~ 0.01 Am^2), then small favorable changes in some model parameters may be hidden by the large changes required in others. The ideal is to have a non-dimensionalized model space, where unit changes in each model parameter have about the same impact on the objective function. We therefore scale each model parameter by dividing by the following values,

$$\mathbf{x}_{typ} = (1, 1, 1)\text{m}, \; \mathbf{m}_{typ} = (0.1, 0.1, 0.1)\text{Am}^2 \text{ and } d_{typ} = 5 \text{ n}T \tag{30}$$

4 Application of the inversion method

Currently, the inversion algorithms are implemented in Matlab and comprise part of a GUI driven toolbox for geophysical processing developed at The University of British Columbia. Anomalies are first identified in a data-set using a combination of automatic and manual interpretation. Then, the inversion algorithm is applied to a user specified area about each anomaly (typically around 2×2 m^2 to 3×3 m^2). The algorithm is terminated when the objective function decreases by less than a specified tolerance, or when the gradient falls below a specified value. Both these parameters are user controlled.

Summary reports can be generated, and the results visually inspected as demonstrated in Figure 6. We will illustrate the performance of the inversion algorithm on a large magnetics survey collected as part of an clearance project in the Helana Valley, Montana.

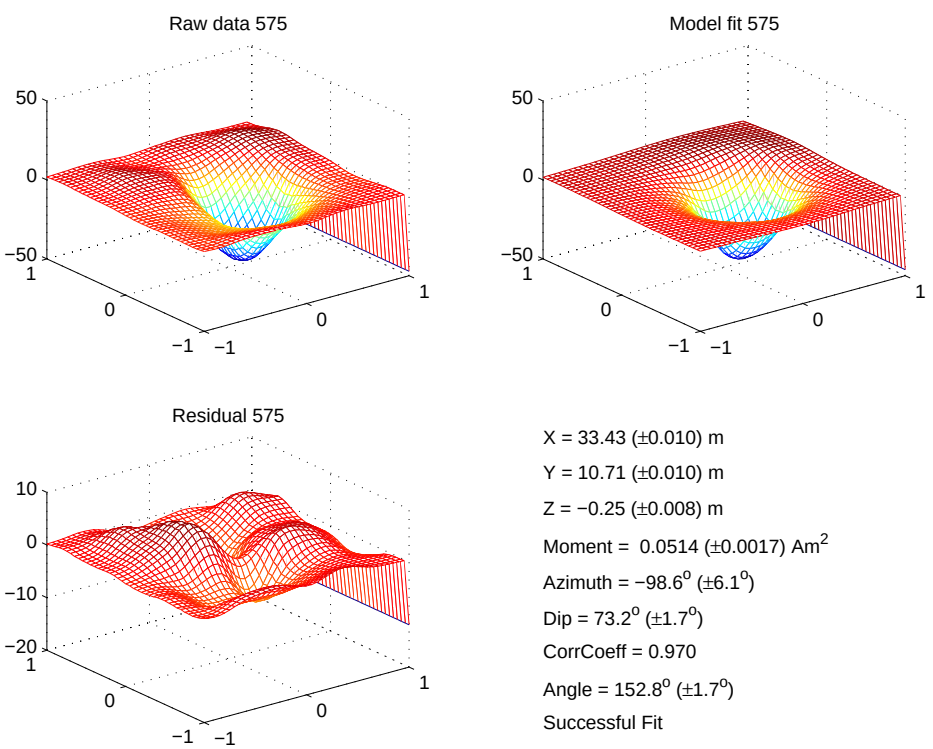

Figure 6: Example result of dipole moment inversion; the numbers in brackets are the estimated standard deviations of the recovered parameters. *Azimuth* and *Dip* refer to the orientation of the dipole in geographic coordinates, while *Angle* is measured between the dipole moment and the Earth's field.

Figure 7: Some of the 81-mm mortars recovered at Guthrie Rd.

The Guthrie Road, Montana dataset

Once open fields, portions of the Helena Valley were used in the 1950s for military training by Montana Army National Guard (MTARNG). The National Guard Bureau funded the remediation project which was divided into two phases focusing on different impact areas: Diamond Springs and Guthrie Road. We consider the data collected in the Guthrie Road area in the summer of 1998. G-tek Australia, conducted a magnetometer survey of the area using an all-terrain vehicle towing an array of eight cesium vapor magnetometers (Clark et al., 1999). The system was equipped with a real-time global positioning system that allowed anomalies to be positioned to within about 20 centimeters.

G-tek found 840 anomalies that were tagged as potential UXO, and these were excavated in the summer of 1999. We analyze 822 of the anomalies (we couldn't locate the data for the remaining 18 anomalies). Table 2 partitions the dig-sheet identifications into six categories; 76-mm projectiles, 81-mm mortars, large pieces of ordnance, shrapnel, metallic debris and geology (including anomalies where no metallic items were found).

A selection of the 81-mm mortars recovered at Guthrie Rd are shown in Figure 7. Most are intact and have not been substantially deformed by the force of impact. However, there are a number of deformed but intact items. These tend to have been practice rounds that were deformed when the black spotter charge detonated on impact. There are also a number of items that have been split into pieces, these were not classified as UXO.

We fitted dipole moments using a percentage error of $\gamma = 5\%$ and a base error of $\epsilon = 1$ nT. The entire run of inversions took around $\frac{1}{2}$ hour on a fairly standard desktop

computer (Pentium Pro Processor with 800 MHz processor and 1 Gb RAM). We use the correlation coefficient c between fitted and observed data to determine the goodness of fit. We found that 85, or around 10% of anomalies had fits with $c < 0.7$ and 162, or around 20% had $c < 0.8$. A break-down according to the dig-sheets of the failed fits is given in Table 2. Most of the failed fits are from items identified as shrapnel, geology or metallic debris, with only one ordnance item having a failed fit. We did not visually inspect every failure, but those we did inspect generally had some type of data issue. These included overlapping acquisition lines that we couldn't remove without undue effort; levelling problems between adjacent lines; and overlapping anomalies. In no case did the inversion algorithm fail where the data quality was good. In the next sections we will describe methods for discrimination and identification and apply them to this data-set.

	76-mm	**81-mm**	**Large pieces**	**Shrapnel**	**Metal**	**Geology**	**Total**
All items	34	49	19	217	377	126	822
Failed fits	0	1	1	13	41	29	85

Table 2: Number of items found during excavation, and the number of fits with $c < 0.7$ (failed fits)

5 UXO Discrimination

The last section described how dipole moments and position are fit to each anomaly. If the data-fit is unsatisfactory the anomaly is marked as such and in a production clean-up would be excavated as potential UXO. From the viewpoint of data interpreters, we are unable to provide any reliable information on the target characteristics. On the other hand, if the fit is satisfactory we attempt to use the recovered dipole moment to discriminate UXO's from non-UXO's. For those items classified as potential UXO the additional step of ordnance identification is attempted as described in the following section.

Our method for ordnance discrimination is based on that described earlier in this report, and is due to Nelson et al. (1998). Briefly, the method relies on the following two factors;

1. Shock demagnetization causes the remnant magnetism of an ordnance to be virtually eliminated;

2. The induced magnetization in a spheroid with $e < 7$ is constrained to lie within about 60^o of the Earth's field (Figure 3).

With a recovered dipole moment of $\mathbf{m}$, our discrimination routine is to calculate the angle between it and the Earth's field, $\mathbf{B}_o$,

$$\psi = \arccos\left(\frac{\mathbf{m} \cdot \mathbf{B}_o}{\|\mathbf{m}\|\|\mathbf{B}_o\|}\right) \tag{31}$$

We can never be certain that all remnant magnetization has been erased by the shock of impact. Additionally, non-ordnance items, whether remnantly magnetized or not, may have dipole angles close to the Earth's field. Consequently, it is not possible to make a definitive ordnance/non-ordnance distinction for all anomalies. Our preferred discrimination method is to rank items according to the likelihood they are due to ordnance. We do this on the basis of the angle ψ; the items with smaller ψ are ranked higher up the list. In a clean-up operation one then excavates according to the list. If resources are available to dig 50% of the anomalies then the first 50% of items in the list are excavated. As a quality control measure a certain number of the lower ranked items should also be excavated.

The Guthrie Road, Montana dataset

In Figure (8a) we plot the dipole magnitude and angle relative to the Earth's field of all the non-ordnance anomalies. Most of the dipoles lie within $\pm 90^o$ of the Earth's field but a large number have angles exceeding 60^o. On the other hand, the dipole angles for the ordnance and large ordnance fragments almost all lie within $\pm 60^o$ of the Earth's field Figure (8b). These results indicate that significant shock demagnetization has occurred to the ordnance. There is only one significant outlier, with an angle of around 70^o.

In Figure (9a) we give a normalized histogram of the angles for the different categories of items. There is a clear concentration of ordnance with dipole angles close to the Earth's field (we include the significant sized ordnance fragments in this category).

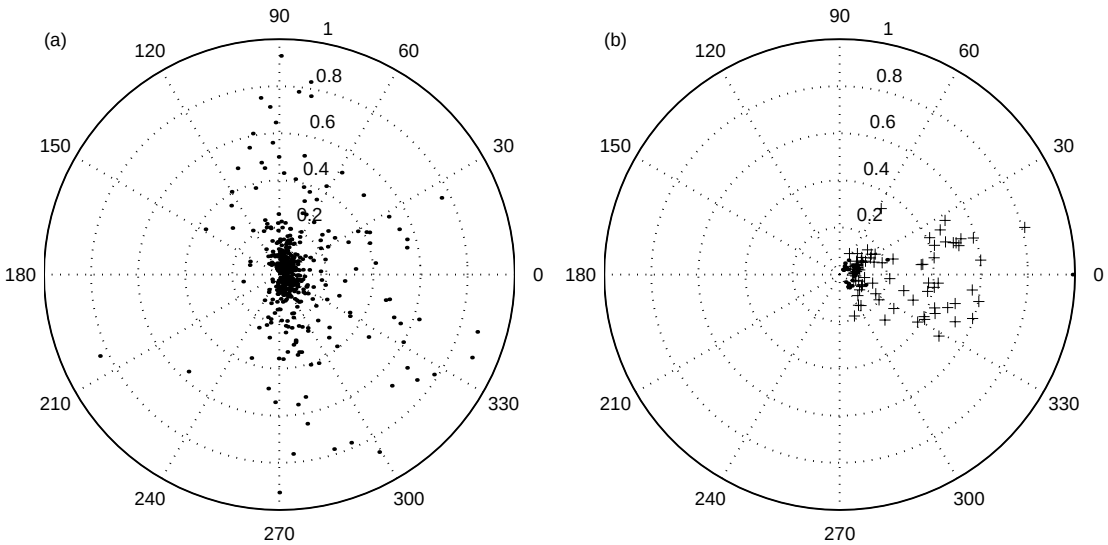

Figure 8: (a) Polar plot of dipole angle and magnitude (Am^2) of non-ordnance items; (b) Same for ordnance (cross) and significant ordnance fragments (dots).

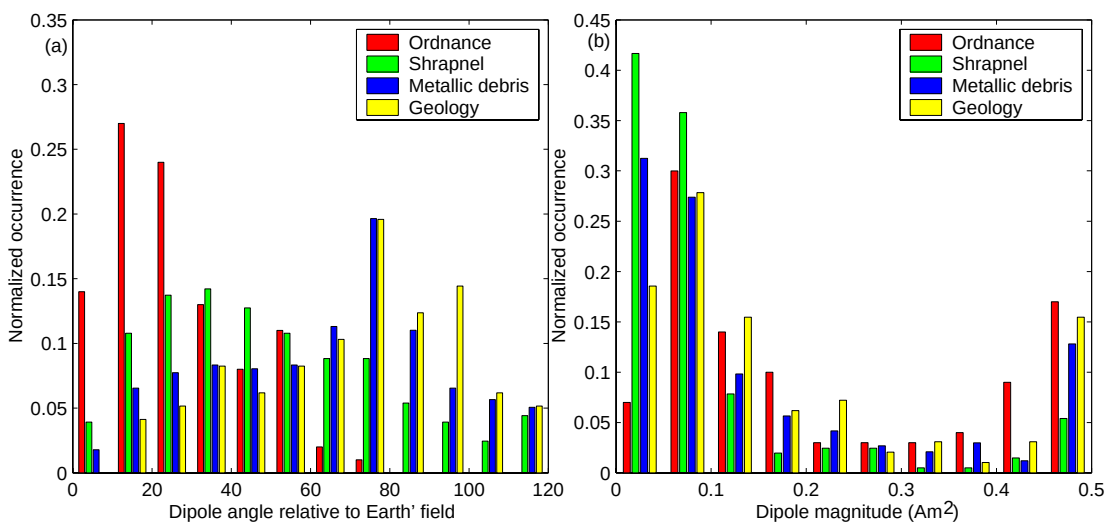

Figure 9: Breakdown of dig-sheets identifications and their (a) dipole angle relative to the Earth's magnetic field; and (b) dipole magntitude.

Shrapnel tends to have relatively low angles, but there are a significant number of items with larger angles. There are two simple mechanisms that could explain this distribution:

1. Shock demagnetization sometimes occurs with shrapnel but not always;

2. Shrapnel acquires a remnant magnetization after impact, in the presence of the Earth's field.

Metallic debris and geological anomalies can have significant remnant magnetism, with a definite peak in the distribution between 60^o and 100^o. We can think of no plausible explanation for this peak in the distribution of dipole angles.

Angle	Dig	Leave	Ordnance found	Ordnance missed	False alarms
55	449	373	78	5	371
60	485	337	81	2	404
65	522	300	82	1	440
70	553	269	82	1	471
75	605	217	83	0	522

Table 3: Guthrie Road discrimination results for intact ordnance items. Discrimination used the dipole angle only.

Angle	Dig	Leave	Ordnance found	Ordnance missed	False alarms
55	449	373	91	11	358
60	485	337	99	3	386
65	522	300	101	1	421
70	553	269	101	1	452
75	605	217	102	0	503

Table 4: Guthrie Road discrimination results, including large pieces of ordnance items. Discrimination used the dipole angle only.

The results of discrimination using different cut-off angles, for intact ordnance items are summarized in Table 3, and for ordnance items and large fragments in Table 4. The tables give the number of items to dig (including the 85 anomalies with poor fits), the number left in the ground, the ordnance found, the ordnance left and the number of false alarms. Figure (10) plots the proportion of items recovered versus the number of holes that need to be excavated. Once the 85 anomalies with poor fits have been dug, there is a high yield of ordnance as the number of holes increases. However, once about 80% of items have been recovered there is a noticeable slow-down in the ordnance yield; a lot of holes need to be dug to recover the last few ordnance items. A total of 560 (68%) of holes are required to recover all ordnance items; this number also recovers all the large ordnance pieces.

Many of the dipole fits for shrapnel and metallic debris have moments with low magnitude (Figure 9b). None of the intact ordnance items has a dipole magnitude less than 0.05 Am^2. However, seven of the large ordnance fragments have dipole moments less than this value. The results of rejecting items as non-ordnance based on the dipole magnitude (as well as a cutoff angle of 75^o) are summarized in Tables 5 (for ordnance only) and 6 (for large fragments as well). With a dipole cutoff of 0.05 Am^2 no intact ordnance items are missed and we can leave 379 items in the ground (46% saving). If we make the reasonable assumption (for this area) that the smallest item likely to be found is a 60-mm mortar, the 0.05 Am^2 cutoff is quite sensible; the minimum dipole moment expected from a 60-mm mortar is around 0.055 Am^2. Ranking items by their magnitude results in a lower initial yield of ordnance (Figure 10) than ranking them by angle. However, the magnitude ranking does not suffer as significant a slow-down in yield, with a crossover occurring once about 80% of items have been recovered. A total of 443 (54%) holes need to be excavated to recover all the ordnance.

One additional discrimination method is examined. It uses the idea of remnant magnetism and requires information on the ordnance items likely to be found in the area. For the Guthrie Rd data we assume that 60 and 81-mm mortars and 76, 90, 105 and 155-mm projectiles may be present in the area and we use the ordnance dimensions

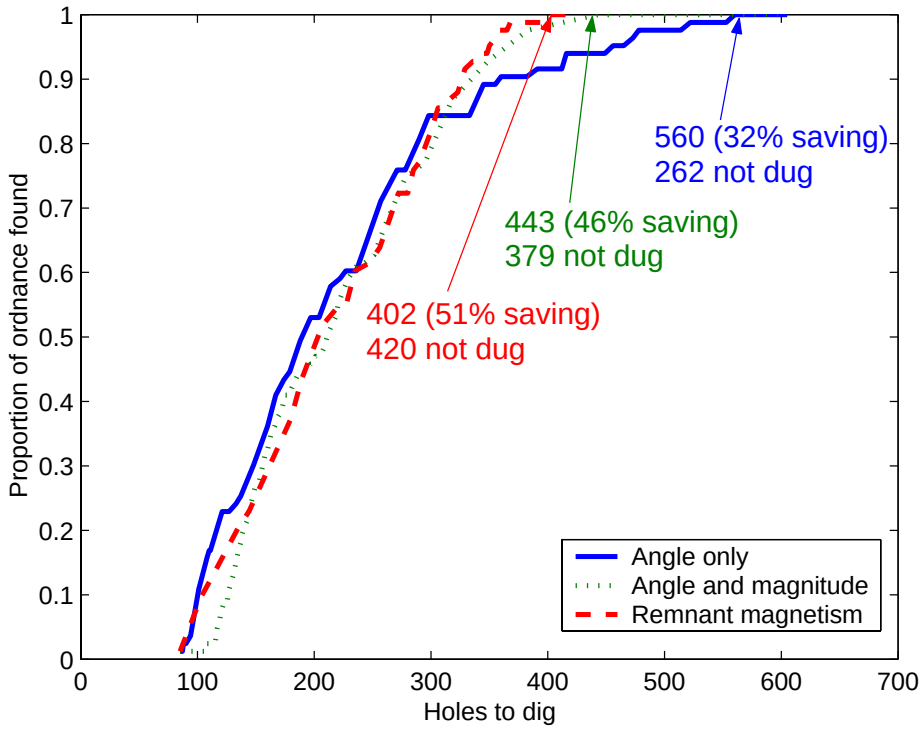

Figure 10: Yield of ordnance with number of holes dug for the three discrimination methods. For all methods it is assumed the 85 anomalies with poor fits are excavated first.

Mag. (A/m)	Dig	Leave	Ordnance found	Ordnance missed	False alarms
0.06	383	439	81	2	302
0.05	443	379	83	0	360

Table 5: Guthrie Road discrimination results for intact ordnance items. Discrimination used the dipole angle (75^o) and magnitude.

listed in Table 7. The method is described in more detail in the next section. Briefly, we determine the minimum percentage of remnant magnetization required to make the recovered dipole moment match of the ordnance items. We then rank the items according to the percentage of remnant magnetism, with lower percentages higher up the list. The method does not apply to large ordnance fragments as these are not considered in our modelling.

The results of discriminating by remnant magnetism are summarized in Table 8. Note, that we also incorporate the angle constraint ($< 75^o$) and the magnitude constraint (> 0.05 Am^2). Allowing up to half of the dipole anomaly to be due to remnant magnetization, we can identify all ordnance items and leave 420 anomalies in the ground (51% saving). The ordnance versus number of holes curve for remnant magnetization (Figure 10) reveals a high yield of ordnance with increasing number of excavations. There is only a very slight slowdown in yield once about 95% of ordnance items have been found. Once 402 (49%) of anomalies are excavated all ordnance items are recovered.

Mag. (Am^2)	Dig	Leave	Ordnance found	Ordnance missed	False alarms
0.06	383	439	90	12	293
0.05	443	379	95	7	348
0.04	493	329	98	4	395
0.03	558	264	100	2	458
0.02	597	225	102	0	495

Table 6: Guthrie Road discrimination results, including large pieces of ordnance items. Discrimination used the dipole angle (75^o) and magnitude.

Item	Diameter (mm)	Aspect ratio
60-mm mortar	60	3.78
76-mm projectile	76	3.57
81-mm mortar	81	3.54
90-mm projectile	90	5.0
105-mm projectile	105	3.71
155-mm projectile	155	4.0

Table 7: Ordnance sizes used for the Guthrie Road identification results.

Remnant (%)	Dig	Leave	Ordnance found	Ordnance missed	False alarms
10	228	594	46	37	182
20	306	516	71	12	235
30	350	472	79	4	271
40	384	438	82	1	302
50	415	407	83	0	332

Table 8: Guthrie Road discrimination results for intact ordnance items. Discrimination used the dipole angle (75^o), magnitude (< 0.05 Am^2) and remnant magnetism.

6 Ordnance identfication

Identification using the recovered dipole moment

For those anomalies classified as potential ordnance, the next step is to try to identify the ordnance type. We established in Appendix B and an earlier part of the report that a given dipole anomaly could have been produced by an infinite number of spheroids (Figure 5). However, for any given site, there are only a finite number of ordnance types that are likely to be found. This is the key observation that allows us to identify ordnance type in the presence of ambiguity.

The dipole induced in a spheroid depends on the angle between the spheroids semi-major axis and the Earth's field. There is no azimuthal dependence due to symmetry. As the ordnance is rotated about the Earth's field the induced dipole moment will trace out a curve such as that shown in Figure (4). This represents all dipole moments that can be produced by the given ordnance item in the absence of remnant magnetism. This mapping procedure can be repeated for all ordnance items suspected of occurring in the area. With N_o ordnance items, a series of curves, $\{\mathbf{m}_k(\theta),\ k = 1, \ldots, N_o\}$, will be generated. For a particular recovered dipole moment $\mathbf{m}$, we calculate the minimum distance between it and each of the dipole curves

$$\Delta m_k = \min_{0 \le \theta < 2\pi} \|\mathbf{m} - \mathbf{m}_k(\theta)\| \tag{32}$$

We assume that any discrepancy is due to remnant magnetism which, as a percentage of the observed moment, will be

$$\gamma_k = 100 \frac{\Delta m_k}{\|\mathbf{m}\|} \tag{33}$$

This allows us to rank the ordnance items according to the likelihood they produced the observed anomaly. The most likely item is that with the lowest percentage remnant magnetism.

The success of the procedure will depend on;

1. The accuracy of the recovered dipole moment (see the error analysis section);
2. The orientation of the ordnance, because some orientations produce dipoles that are close to dipoles potentially produced by other ordnance items;
3. How closely the spheroid approximation matches that for real ordnance; and
4. How much remnant magnetism the ordnance maintains after the shock of impact.

The Guthrie Road, Montana dataset

The dipole moments for those anomalies due to 76-mm projectiles are shown in Figure (11a) and for 81-mm mortars in Figure (11b). Misidentifications for both types of ordnance appear likely due to the overlapping curves for the difference ordnance types. In particular the moments for almost all the 76-mm projectiles are in a region where the

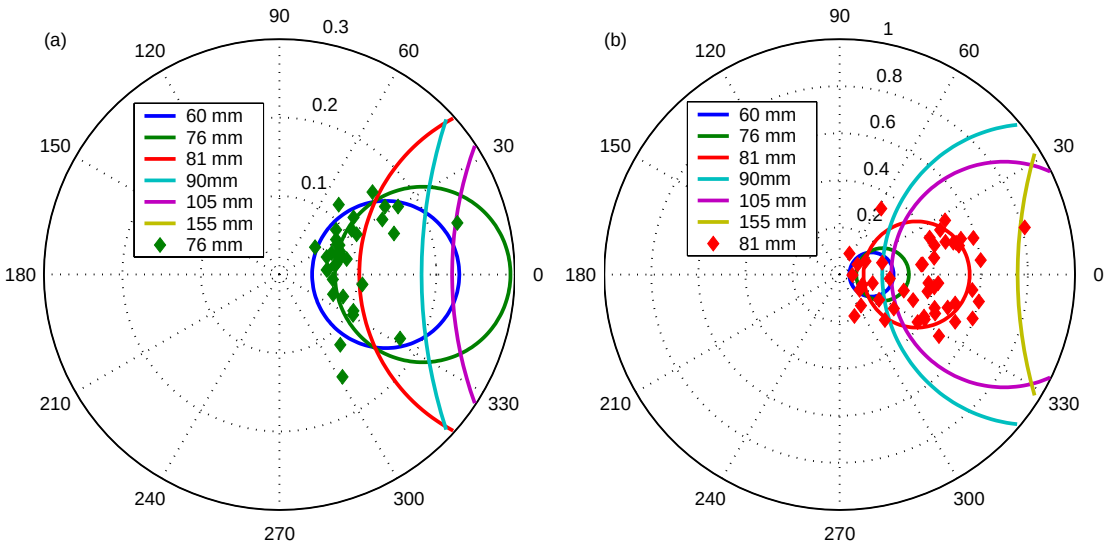

Figure 11: Dipole moments of the Guthrie Road ordnance items for (a) 76-mm projectiles; and (b) 81-mm mortars.

60, 76 and 81-mm calibre ordnances have similar dipole moments. For the 81-mm mortars about half the moments are in a region with only the curve for the 81-mm nearby, while the other half are in the more complex part of the plot. Our dipole identification routine involves finding the ordnance curve that is closest to each recovered moment.

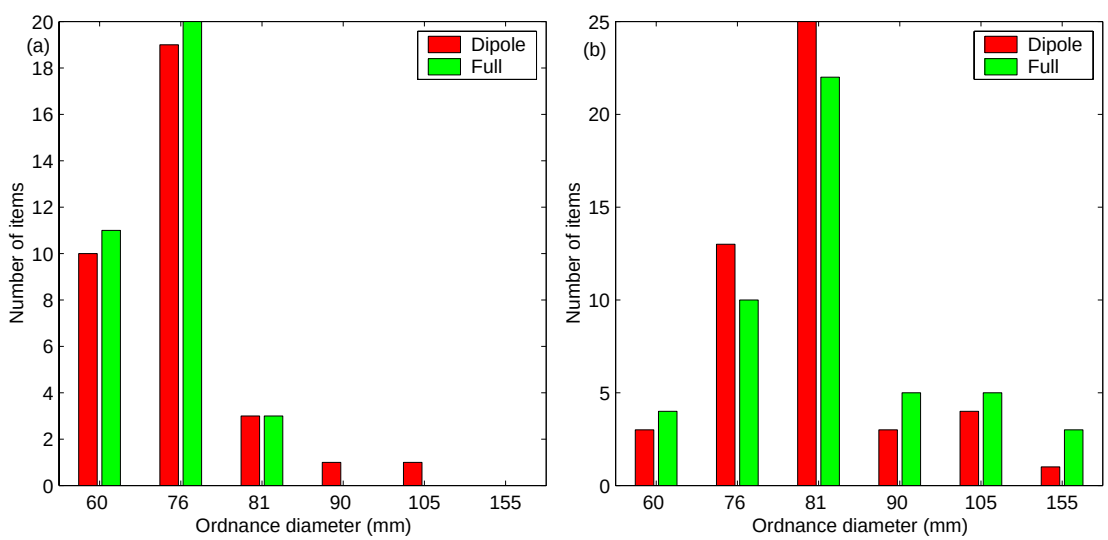

Figure 12: Identification results for the Guthrie Road data using both the dipole and dipole plus octupole methods for (a) 76-mm projectiles; and (b) 81-mm mortars.

Dipole identification results for 76-mm projectiles are given in (Figure 12a) and for 81-mm mortars in Figure (12b). In 19 out of 34 cases (56%) the 76-mm projectile is identified correctly. The most common case of misidentification is as a 60-mm mortar; from Figure (4) we see that this is due to overlapping moments between the 60 and 76-mm ordnances. For 81-mm mortars the identification routine is correct in 25 of 48 cases (52%), so that overall we achieve correct identifications 54% of the time.

Figure 13: One of the practice 81-mm mortars deformed due to the detonation of the spotting charge.

The most common misidentification for the 81-mm mortar is as a 76-mm projectile (13 times). Some of the errors in misidentification could relate to the deformation of certain of the 81-mm practice mortars that occurred when the spotter charge detonated (Figure 13). A spheroid is unlikely to give a very good approximation to this item. Unfortunately, while recovered ordnance items were retained after excavation no records of the anomaly number were kept. Thus, we cannot determine which recovered dipole moments correspond to deformed ordnance.

Assuming we are using the remnant magnetization method for discrimination and use a cutoff of 50%, there will be 235 false alarms; items incorrectly identified as ordnance. Applying the identification method to these false alarms (Figure 14a) is most likely to cause a misidentification as a 60-mm mortar (the moments are generally quite low). Metallic debris is more likely to give a false identification as a large ordnance item than any of the other categories of items (shrapnel, large ordnance pieces and geology).

Seeded test site at The Former Fort Ord, California

The former Fort Ord is located near Monterey Bay in northwestern Monterey County, California. Since 1917, portions of Fort Ord were used by Army units for maneuvers, target ranges, and other purposes. Investigation and ordnance removal actions have been conducted at the former Fort Ord since 1994 when the base closed. In November 1998, the United States Department of the Army instigated an Ordnance Detection and Discrimination Study (ODDS) at Fort Ord (Asch and Staes, 2001).

The purpose of the Seeded Test was to evaluate the detection and discrimination capabilities of selected geophysical instruments when ordnance items are buried or "seeded" below the ground surface in a local site-specific geologic conditions. The seeded test area consists of five separate, adjacent grids, which were cleared of anomalies to pro-

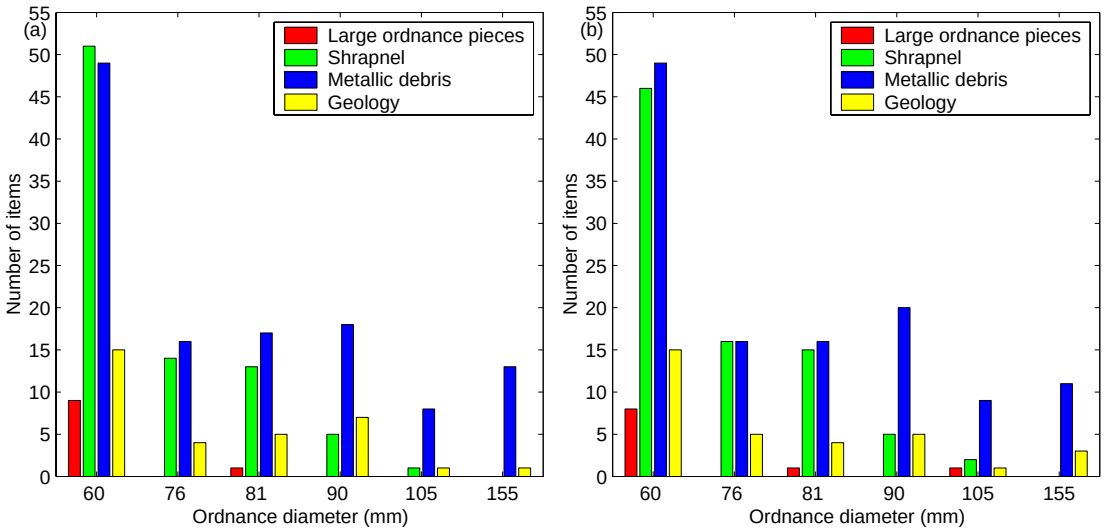

Figure 14: Identification results for the Guthrie Road data for (a) dipole method; and (b) dipole plus octupole method.

vide a controlled testing environment. Two grids are "known" plots where the items, depths and orientations of items are made known to all participants. It is these two known sites (K1 and K2) that we analyze here.

Seventeen different types of ordnance items were buried in the seeded test plots. Some ordnance scrap and other items were also seeded to allow evaluation of discrimination capabilities. Additional areas of the plots were excavated and back-filled without any buried items.

For K1, 5 of the 7 "empty hole" items (618, 619, 621 to 623) did not produce acceptable fits, so they would not have been declared as potential ordnance. The other two "empty holes" had poorly fitting dipoles and would have been identified as scrap. A fragment (595) and a signal illumination flare (612) also produced unacceptable fits.

Discrimination and identification results for the remaining items are summarized in Table 9. Note, that the column marked *Interp* lists the first choice interpretation for each item (e.g. scrap, 22 mm projectile, 60 mm ordnance etc). The column marked *Rank* shows where the actual ordnance item was ranked. For instance, consider the 2.36" rockets. If the *rank* was 1 then the item was identified correctly as a 2.36" rocket (e.g. anomaly 613). If the *rank* was greater than 1 (say 3), then the 2.36" rocket was ranked as the third most likely cause of the anomaly (e.g. anomaly 602).

Two of the four fragments were correctly identified as non-ordnance (using a discrimination cutoff of 60^o). Six of the twelve 35-mm projectiles were incorrectly classified as scrap; this may be due to remnant magnetism. Five of the remaining 35-mm projectiles had the correct identification ranked as one of the top three choices. One of the 2.36" rockets was classified as scrap, the other three had a 2.36" identification ranked in the top three (one was correct). The six signal illumination flares could not be identified correctly, neither could any of the grenades. Overall, the discrimination/identification results for K1 are not very impressive. We believe part of the reason could be due to remnant magnetism (the items were not shock demagnetized prior to emplacement). It may also be a reflection of the generally poor performance of magnetics for small calibre items (Klaff et al., 2002).

Number	Item	z_a (m)	z_r (m)	c	Angle	Interp	Rank
620	Empty Hole	0.00	0.47	0.79	127.4	Scrap	
617	Empty Hole	0.00	0.29	0.75	97.0	Scrap	
599	Fragment	0.30	0.92	0.88	86.1	Scrap	
598	Fragment	0.30	0.62	0.90	114.4	Scrap	
597	Fragment	0.15	0.28	0.97	48.8	Signals	
596	Fragment	0.30	0.41	0.91	55.2	22 mm	
616	35-mm	0.61	0.56	0.93	74.0	Scrap	
608	35-mm	0.46	0.23	0.85	59.0	22 mm	2
607	35-mm	0.30	0.23	0.82	150.1	Scrap	
606	35mm	0.15	0.25	0.98	33.6	37-mm	6
605	35-mm	0.46	0.95	0.91	52.4	Signals	3
604	35-mm	0.61	1.50	0.81	65.3	Scrap	
603	35-mm	0.15	0.37	0.90	55.2	22 mm	2
600	35-mm	0.30	0.43	0.86	68.8	Scrap	
593	35-mm	0.61	0.53	0.92	38.0	22 mm	3
592	35-mm	0.30	0.44	0.97	87.1	Scrap	
591	35-mm	0.61	0.34	0.95	105.6	Scrap	
590	35-mm	0.46	0.38	0.96	37.5	60-mm mortar	2
613	2.36" rocket	0.61	0.65	0.96	57.1	Rocket 2 .36"	1
602	2.36" rocket	0.46	0.59	0.98	55.1	Signals	3
594	2.36" rocket	0.61	0.89	0.96	50.8	Rocket 3 .5"	4
586	2.36" rocket	0.61	2.79	0.96	118.2	Scrap	
615	Signals	0.15	0.26	0.97	39.7	37-mm	2
614	Signals	0.30	0.61	0.82	82.6	Scrap	
611	Signals	0.15	0.33	0.89	43.3	22 mm	3
589	Signals	0.30	1.08	0.89	20.1	22 mm	8
588	Signals	0.30	1.51	0.95	31.6	81-mm mortar	6
610	Hand grenade	0.15	0.08	0.93	49.9	22 mm	12
609	Hand grenade	0.30	0.58	0.77	38.6	22 mm	12
587	Hand grenade	0.30	0.88	0.99	121.5	Scrap	
601	Rifle grenade	0.46	1.33	0.78	77.9	Scrap	

Table 9: Fort Ord identification results for K1, where z_a is the actual burial depth, z_r is the recovered depth, c is the correlation coefficient between observed and predicted data and *angle* is the angle between the Earth's field and the recovered dipole moment.

For the K2 plot, good dipole fits could not be obtained for four items, 555, 556 (both, 25-mm projectiles at 46 cm), 569 (fragment at 30 cm) and 574 (signals at 30 cm). The results for the rest of the items are summarized in Table 10. There were seventeen items correctly identified as ordnance. Six of these were identified as the correct ordnance type and five others had the correct ordnance listed in the top three possibilities. The other six identifications were a long way off and we believe that several of these were remnantly magnetized; in particular all the stokes mortars and the hand grenade.

Identification using the dipole and octupole

Magnetic anomalies from ordnance are usually dominated by the dipole component; however, with high quality data we may be able to obtain useable information from the octupole term. Due to the dipole dominance it would probably not be a good idea to attempt a direct inversion for ordnance dimensions (local minima, non-uniqueness etc). Rather, a better method is to obtain an optimum fit for each ordnance item in

Number	Item	z_a (m)	z_r (m)	c	Angle	Interp	Rank
565	Fragment	0.15	0.14	0.93	92.1	Scrap	
566	Fragment	0.30	0.34	0.98	113.5	Scrap	
567	Fragment	0.15	0.14	0.95	52.3	22 mm	
568	Fragment	0.30	0.28	0.89	37.3	37-mm	
578	Fragment	0.15	0.22	0.92	32.5	60-mm mortar	
579	Fragment	0.30	1.82	0.86	90.1	Scrap	
581	Fragment	0.30	0.57	0.90	36.4	22 mm	
580	25-mm	0.61	0.59	0.82	72.1	Scrap	
553	35-mm	0.61	0.67	0.95	29.1	35-mm	1
559	35-mm	0.61	0.77	0.89	33.2	75-mm	8
575	35-mm	0.30	0.26	0.97	154.0	Scrap	
563	37-mm	0.46	0.20	0.81	55.6	22 mm	3
583	37-mm	0.61	0.93	0.85	47.7	35-mm	5
584	37-mm	0.61	1.03	0.89	61.8	Scrap	
554	2.36" rocket	0.61	0.89	0.97	21.6	90-mm	9
558	2.36" rocket	0.61	0.81	0.94	49.5	105-mm	3
564	75-mm	0.76	0.67	0.96	12.6	75-mm	1
572	75-mm	0.91	1.85	0.86	85.6	Scrap	
560	Signals	0.30	0.50	0.81	124.4	Scrap	
576	Signals	0.15	0.16	0.95	99.8	Scrap	
573	3" Stokes	1.02	0.63	0.86	60.0	35-mm	10
577	3" Stokes	1.02	1.22	0.89	19.2	155-mm	2
585	3" Stokes	0.91	0.66	0.87	16.2	35-mm	9
561	81-mm	0.91	1.13	0.96	39.5	81-mm mortar	1
571	81-mm	0.91	0.85	0.94	34.8	90-mm	2
557	90-mm	0.76	0.82	0.97	21.3	90-mm	1
570	90-mm	0.76	0.73	0.97	20.2	90-mm	1
562	105-mm	1.22	1.16	0.94	59.7	Rocket 2.36"	3
582	105-mm	1.22	1.50	0.96	17.8	105-mm	1
552	Hand grenade	0.30	0.44	0.92	44.4	Signals	12

Table 10: Fort Ord identification results for K2, where z_a is the actual burial depth, z_r is the recovered depth, c is the correlation coefficient between observed and predicted data and *angle* is the angle between the Earth's field and the recovered dipole moment

our library, and declare the ordnance with the best fit as the most likely source of the anomaly. For each item in the library this procedure involves determination of six model parameters $(x, y, z, \theta, \phi, d)$, where (x, y, z) is location, θ is the ordnance dip angle relative to horizontal, ϕ is the azimuth angle relative to geographic North and d is the dc-shift.

We again use a least-squares formulation and the interior-reflective Newton method. The data-weighting and parameter bounds are identical to that used for the dipole inversion (i.e. we only bound the spatial location). For scale factors we use

$$\mathbf{x}_{typ} = (1, 1, 1)\text{m}, (\theta_{typ}, \phi_{typ}) = (\pi/2, \pi/2)\ radians\ and\ d_{typ} = 5\text{n}T \tag{34}$$

To determine the starting model, we first do a dipole inversion and go through the dipole identification process. For each ordnance item, the identification process will return the dip angle θ and azimuth ϕ that achieved the closest fit to the dipole. These can be used as the starting orientation with the dipole location used as the starting location, similarly for the dc-shift. Rather than doing an inversion for every item in the library we only consider those 3-5 ordnance items with the best dipole fits.

The Guthrie Road, Montana dataset

We only apply the dipole/octupole identification procedure to those anomalies flagged as potential UXO by the remnant magnetization technique (with a cutoff of 50% remnant magnetism). The quality of the fits obtained for the optimum ordnance were around the same as the dipole fits; sometimes they were slightly worse and sometimes slightly better.

Identification results for the dipole/octupole method for 76-mm projectiles are given in Figure (12a) and for 81-mm mortars in Figure (12b). For 76-mm projectiles the correct identification is achieved for 20 of 34 cases, one better than the dipole method. However, for the 81-mm mortar correct identification is only achieved for 22 of 48 cases, three less than the dipole method.

Misidentification results for false alarms are given in Figure (14b). The distribution of items is very similar to that achieved with the dipole method.

We believe that there are three reasons why the dipole/octupole identification method does not improve the original dipole identification method.

1. The octupole response is quite small and does not provide significant additional constraints on the the geometry;

2. The equivalent spheroid is not an accurate enough approximation of an ordnance item for the octupole contribution to have a positive effect; and

3. The ordnance items are slightly remnantly magnetized which changes the relationship between ordnance orientation and the direction of magnetization.

Identification using the dipole and quadrupole

Thus far, the identification routines we have developed have relied solely on a spheroid model of ordnance. However, this assumption is overly simplistic since most ordnance items do not have that degree of symmetry. In particular, the front and tail ends of ordnance tend to be different: the front is often tapered to provide better aerodynamics and target penetration, while the tail end is often flat (the tails of mortars don't matter because they are usually made of aluminum). Therefore, a more realistic model of ordnance is an axially symmetric body without front-back symmetry; such a body has a multipole expansion with both a dipole term and a non-zero quadrupole term (recall that the quadrupole was zero for a spheroid due to symmetry).

Our intent with this new identification method is to try to use the information in the quadrupole to constrain the orientation of the body (ϕ, θ). As we discovered when using the dipole method, the principal source of ambiguity in identification is our inability to constrain the orientation of the body. In particular, when the object's dimension is changed, one can compensate by changing the object orientation and produce the same or a very similar dipole moment. If we could constrain the orientation then we could better constrain the ordnance dimension.

The basis of the idea is that there will be no quadrupole contributions perpendicular to the axis of symmetry but there will be contributions along the symmetry axis. We therefore construct a model with these characteristics and use an inversion procedure to recover a model with the best orientation. Concomitant with this process we also recover parameters that depend on the shape of the body, as we now explain.

The dipole moment of an axially symmetric body can be written in the form,

$$\mathbf{m} = \mu_o^{-1}\mathbf{A}^T\mathbf{F}\mathbf{A}\mathbf{B_o} \tag{35}$$

where $\mathbf{A}$ is the usual Euler rotation tensor and $\mathbf{F}$ is a 3×3 diagonal matrix with (F_2, F_2, F_3) along the diagonal. We are assuming axial-symmetry so that $F_1 = F_2$. The demagnetization factors, F_i, given in the above equation, are VF_i times those previously given in Equation 2, where V is the volume of the body. These volume modified demagnetization factors contain all the information on the body's dimensions that we are attempting to recover.

We are assuming the body is axially symmetric (about the z-axis), therefore the quadrupole tensor components in the x-y plane are zero (see Appendix A for a derivation). The body is asymmetric about the x-y plane so that the quadrupole tensor has non-zero components in the z-direction. The tensor is symmetric $\hat{\mathbf{M}}_q = \hat{\mathbf{M}}_q^T$ and is therefore defined by the equation,

$$\hat{\mathbf{M}}_q = \begin{bmatrix} 0 & 0 & m_{q1} \\ 0 & 0 & m_{q2} \\ m_{q1} & m_{q2} & m_{q3} \end{bmatrix} \tag{36}$$

where m_{q1}, m_{q2} and m_{q3} are dependent on the shape and magnetization of the body. The above equation is in body-centered coordinates. The quadrupole tensor may be rotated into the Earth's frame of reference using the following equation,

$$\mathbf{M}_q = \mathbf{A}\hat{\mathbf{M}}_q\mathbf{A}^T \tag{37}$$

The magnetic field due to this quadrupole tensor can be calculated using Equation (A-11). Ignoring the octupole and any higher order moments, full specification of an axially-symmetric body therefore involves the following 11 parameters

$$[x, y, z, \phi, \theta, F_2, F_3, m_{q1}, m_{q2}, m_{q3}, d] \tag{38}$$

where we have again allowed a dc-shift, d.

To invert for the 11 parameter model we use the same least-squares formulation and Interior-reflective Newton method described previously. The parameter scalings are the same as those given in Equation (34), with the additional parameters scaled as

$$\mathbf{F}_{typ} = (0.01, 0.01)\mathrm{m}^3 \; and \; m_{qtyp} = (0.01, .01, .01)\mathrm{A}m^3 \tag{39}$$

Once the model parameters have been recovered we return to our spheroid model of ordnance and find the object dimensions that reproduce the recovered volume demagnetization factors, F_2 and F_3. This is straightforward because the aspect ratio, e solely determines the ratio F_2/F_3, while the diameter and aspect ratio together determine the magnitudes of F_2 and F_3. On occasion we find that F_2 converges towards zero while F_3 appears to converge to a sensible value. In that case, we fix the aspect ratio at a typical value $3 < e < 5$ and just solve for the diameter.

The Guthrie Road, Montana dataset

We applied the quadrupole inversion method to all 737 anomalies at Guthrie Rd that had good dipole fits. Perhaps self-evidently the fits and correlation coefficients for the dipole/quadrupole model were better than for the dipole model alone. Figure 15

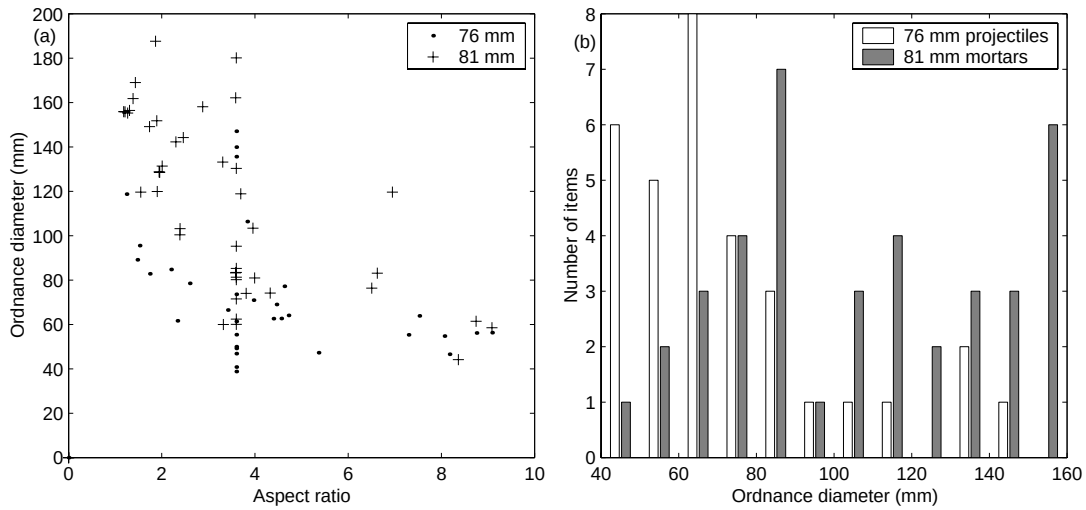

Figure 15: Quadrupole identification results at Guthrie Road; (a) Recovered aspect-ratios and diameters; and (b) Histogram of recovered diameters.

summarizes the results of the quadrupole identification. There appears to be some identification ability but there are a significant number of ordnance items where the recovered dimensions are inaccurate. In particular, there is a tendency to either recover too low an aspect ratio and hence too large a diameter or vice-versa.

There are two conclusions that can be drawn from the quadrupole discrimination results. Firstly, the quadrupole may be unable to provide the required constraints on the ordnance orientation. Alternatively, there may be enough remnant magnetization in the body so that our model is not an accurate reflection of reality.

With these issues in mind we trialed one last method for identification using the quadrupole. This time we allow the dipole moment to vary independently of the quadrupole; i.e. in place of F_1 and F_2 in Equation (38) we solve for $\mathbf{m} = (m_1, m_2, m_3)$. Thus there are twelve parameters to find. Our intent is to determine if unmodelled quadrupole components bias the estimation of the dipole moment.

We applied the method to the Guthrie Road data and then used the recovered dipole moment to achieve ordnance identification in the usual way. We found that the method was slightly inferior to the original dipole identification routine. In particular for the 81-mm mortar 23 of the 48 anomalies were identified correctly (compared to 25 of 48), while for the 76-mm projectile only 16 of 34 cases were correct (compared to 20 of 34). Thus, we conclude that unmodelled quadrupole components do not negatively affect our ability to identify using the dipole moment.

7 Error Analysis

The dipole identification results for Guthrie Road indicate that around 55% of the time we correctly identify the ordnance type. The 45% misidentifications must be due to either an incorrect model, remnant magnetism or uncertainty in the recovered dipole moments. In this section we analyze the uncertainty in recovered dipole moment using linearized error analysis.

Estimating the covariance matrix of the model parameters

To derive the covariance matrix of the model parameters we follow the development given in Bard (1974). At the minimum of the objective function the gradient is zero

$$\nabla\phi(\mathbf{m},\mathbf{d}) = 0 \tag{40}$$

where ∇ is with respect to the model parameters. If we change the data to $\mathbf{d}+\boldsymbol{\delta}\mathbf{d}$ we will change the objective function and hence the position of the minimum will vary to $\mathbf{m}+\boldsymbol{\delta}\mathbf{m}$. The gradient of the new objective function at the new minimum will be zero.

$$\nabla\phi(\mathbf{m}+\boldsymbol{\delta}\mathbf{m},\mathbf{d}+\boldsymbol{\delta}\mathbf{d}) = 0 \tag{41}$$

If we expand this gradient in a Taylor series and only keep first order terms we find

$$\nabla\phi(\mathbf{m}+\boldsymbol{\delta}\mathbf{m},\mathbf{d}+\boldsymbol{\delta}\mathbf{d}) = \nabla\phi(\mathbf{m},\mathbf{d}) + \nabla^2\phi(\mathbf{m},\mathbf{d})\boldsymbol{\delta}\mathbf{m} + \frac{\partial}{\partial\mathbf{d}}\nabla\phi(\mathbf{m},\mathbf{d})\boldsymbol{\delta}\mathbf{d} = 0 \tag{42}$$

Recognizing that the ∇^2 term is the Hessian and rearranging we find

$$\boldsymbol{\delta}\mathbf{m} = \mathbf{H}^{-1}\frac{\partial}{\partial\mathbf{d}}\nabla\phi(\mathbf{m},\mathbf{d})\boldsymbol{\delta}\mathbf{d} \tag{43}$$

The covariance matrix of the model parameters is

$$\mathbf{V}_m = \mathrm{E}[\boldsymbol{\delta}\mathbf{m}\boldsymbol{\delta}\mathbf{m}^T] \tag{44}$$

where $\mathrm{E}[\cdot]$ is the expectation operator. Substituting Equation (43) into (44), recognizing that the Hessian and gradient terms are constants (under expectation) and rearranging terms we find

$$\mathbf{V}_m = \mathbf{H}^{-1}\frac{\partial}{\partial\mathbf{d}}\nabla\phi(\mathbf{m},\mathbf{d})^T\mathrm{E}[\boldsymbol{\delta}\mathbf{d}\boldsymbol{\delta}\mathbf{d}^T]\frac{\partial}{\partial\mathbf{d}}\nabla\phi(\mathbf{m},\mathbf{d})\mathbf{H}^{-1} \tag{45}$$

The covariance matrix of the data is $\mathbf{V}_d = \mathrm{E}[\boldsymbol{\delta}\mathbf{d}\boldsymbol{\delta}\mathbf{d}^T]$. Assuming the data-weighting matrix in our formulation of the inverse problem is the same as the inverse covariance matrix of the data, the Gauss-Newton approximation to the Hessian is

$$\mathbf{H} = \mathbf{J}^T\mathbf{V}_d^{-1}\mathbf{J} \tag{46}$$

while

$$\frac{\partial}{\partial\mathbf{d}}\nabla\phi(\mathbf{m},\mathbf{d}) = \mathbf{V}_d^{-1}\mathbf{J} \tag{47}$$

Substitution of Equations (46) and (47) into Equation(45) and simplification reveals that the covariance matrix is the inverse of the Gauss-Newton approximation to the Hessian,

$$\mathbf{V}_m = (\mathbf{J}^T \mathbf{V}_d^{-1} \mathbf{J})^{-1} = \mathbf{H}^{-1} \tag{48}$$

The above equation can be used to estimate uncertainties in each of the model parameters and can also be used to define confidence ellipses of multiple parameters. The uncertainties obtained through this equation are linearized estimates of the true uncertainties. Before considering them further we investigate how closely these linearized estimates would match fully non-linear estimates. If the minimum of the objective function is $\hat{\mathbf{m}}$ then linearized estimates are equivalent to approximating the objective function with

$$\phi(\mathbf{m}) - \phi(\hat{\mathbf{m}}) \approx \frac{1}{2}(\mathbf{m} - \hat{\mathbf{m}})^T \mathbf{H} (\mathbf{m} - \hat{\mathbf{m}}) \tag{49}$$

If the above equation is a good approximation to the objective function about the minimum then the linearized uncertainties will be accurate estimates of the true uncertainties. We have compared the objective functions of many anomalies and usually find a situation such as that illustrated in Figure (16). The linear and non-linear estimates are very similar for parameters related to the dipole moment, and less so for parameters related to location (especially the depth). From the perspective of ordnance identification it is the uncertainties in the dipole moment that are important, so we can conclude that the linearized estimates should be accurate for our purposes. We note in passing that including the second order terms in the Hessian has very little impact on the accuracy of the linear approximation, even if the residuals at the solution are large. This is readily apparent for the dipole components in cartesian coordinates $\mathbf{m} = (m_x, m_y, m_z)$ because the second derivatives with respect to these parameters are zero (Equation 9).

Confidence ellipses of multiple parameters

We are principally interested in the joint-uncertainty in the dipole magnitude and angle relative to the Earth's field because these two parameters control our decisions on discrimination and identification. A good method for visualizing the joint-uncertainties is to calculate confidence ellipses; these are contours of equal confidence in the model parameters. They are usually defined to encompass a certain probability that the model lies within the defined region. For instance, a one-sigma (or 68.3%) confidence ellipse would delineate a region that has a 68.3% chance of containing the true model parameters (under the particular statistical assumptions used to define the objective function).

To define the confidence ellipse for r parameters requires that the uncertainties in the other $n - r$ parameters (assuming there are n parameters in total) are projected onto the r-dimensional hyperplane under consideration. In turns out (Bard, 1974) that this projection can be implicitly achieved by calculating the covariance matrix through inversion of the appropriate $r \times r$ subsection of the Hessian matrix. For example, if we are interested in the joint confidence ellipse for parameters 2 and 5 we would calculate

$$\mathbf{V}_m = \begin{bmatrix} H_{22} & H_{25} \\ H_{52} & H_{55} \end{bmatrix}^{-1} \tag{50}$$

The principal axes of the ellipse are then obtained by eigenvalue decomposition of $\mathbf{V}_m$,

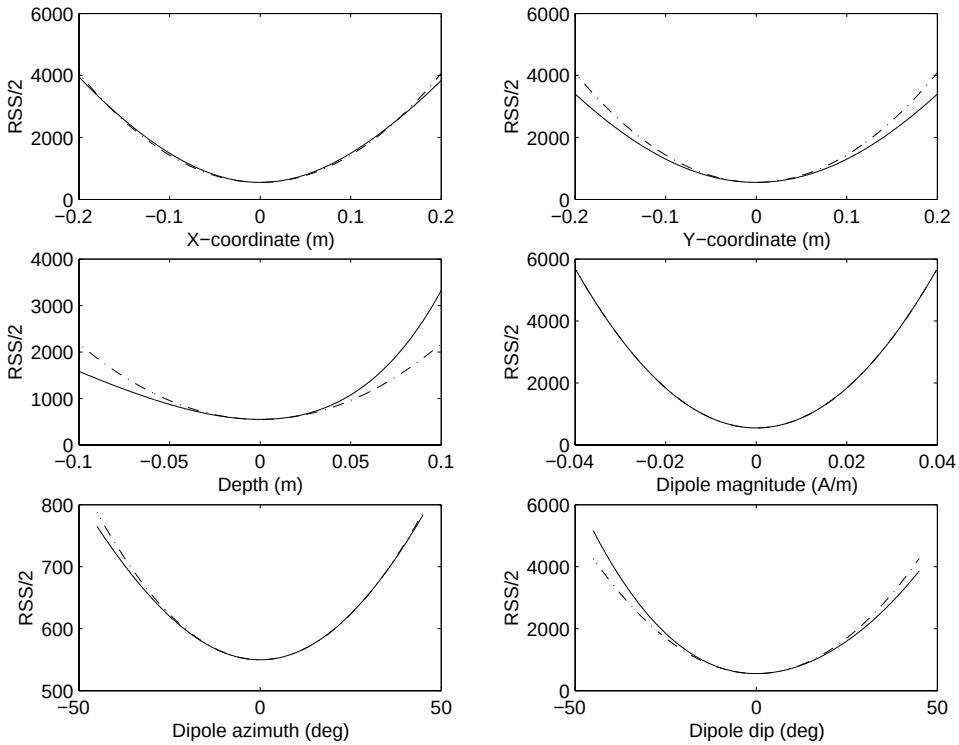

Figure 16: Objective function (solid line) and Gauss-Newton approximation to the Hessian (dashed line) about the inversion solution for Target 575, Fort Ord.

$$\mathbf{V}_m = \mathbf{U}\mathbf{S}\mathbf{U}^T \tag{51}$$

where $\mathbf{S}$ is a diagonal matrix of eigenvalues and $\mathbf{U}$ is an orthonormal matrix of eigenvectors; each eigenvector is a principal axis of the ellipse. The size of each principal axis is given by the reciprocal of the corresponding eigenvalue.

The final step is to find the ellipse that lies on the boundary of a specified confidence region (e.g. 68.3% or the one-sigma error). If the sampling distribution is normal, unbiased and we assume that the covariance matrix $\mathbf{V}_m$ is known, then $(\mathbf{m}-\hat{\mathbf{m}})^T\mathbf{V}_m^{-1}(\mathbf{m}-\hat{\mathbf{m}})$ is χ^2 distributed with r degrees of freedom (Bard, 1974). The boundary of the ellipse corresponding to a particular confidence level is found by calculating the value of the χ^2 distribution with r degrees of freedom that corresponds to that confidence. For example, with 2 degrees of freedom, the 68.3% confidence limit has $\chi^2 = 2.298$. The contour of $(\mathbf{m}-\hat{\mathbf{m}})^T\mathbf{V}_m^{-1}(\mathbf{m}-\hat{\mathbf{m}})$ with the value 2.298 corresponds to the boundary of the 68.3% confidence region.

Alternatively, if the covariance matrix is not known and we assume that all observations are independent (so that $\mathbf{V}_d = \sigma^2\mathbf{I}$) then the confidence level is obtained through the $F_{r,n-r}$ distribution (Bard, 1974). In that case the value of χ^2 calculated above would be replaced with

$$r\sigma^2 F_{r,n-r}(\gamma) \tag{52}$$

where γ is the desired confidence limit ($\gamma = 0.683$ for the 68.3% confidence level) and σ^2 is the sample variance. If the optimum model returned by the minimization routine is $\hat{\mathbf{m}}$ and there are K model parameters then the sample variance is obtained by calculating

$$\sigma^2 = \frac{1}{N-K} \sum_{i=1}^{N} \left[F_i(\hat{\mathbf{m}}) - d_i^{obs} \right]^2 \tag{53}$$

Finally, if the assumption of Gaussian statistics does not hold, conservative confidence limits can be calculated by recourse to the Bienaymê-Chebyshev inequality (Bard, 1974). For the γ confidence limit this replaces the value of χ^2 above with

$$\frac{r}{1-\gamma} \tag{54}$$

The Guthrie Road, Montana dataset

The distribution of residuals for the 660 anomalies at Guthrie Road with correlation coefficients greater than 0.8 are shown in Figure (17). The curves have been normalized so that they have an integral of one; thus we are approximating the posterior probability density function (posterior PDF) of the residuals. The best fitting Gaussian distribution (with $\sigma = 0.99$ nT) provides a poor fit to the residuals. In particular, large residuals are much more likely than predicted by a normal distribution. In Figure (17) we also show the best fitting Ekblom distribution (Ekblom, 1973) which has a probability density function equal to

$$Pr(x) = c \exp \left[\frac{(x^2 + \epsilon^2)^{p/2}}{\sigma^p} \right] \tag{55}$$

where c is a constant that ensures the PDF integrates to unity. This is a perturbed version of an Lp-norm and we found best fitting values of $\sigma = 1.16 \times 10^{-4}$ nT, $\epsilon = 0.609$ nT and $p = 0.224$. The correspondence between the observed distribution of residuals and the Ekblom PDF is excellent. We will consider the good fit of the Ekblom PDF further in the discussion section of this report.

As the residuals are clearly non-Gaussian, we must be cautious when interpreting confidence ellipses calculated under the normality assumption. The shape and relative size of the ellipses are likely to be correct but their absolute values are probably incorrect (i.e. the 68.3% confidence ellipse won't correspond to a confidence of 68.3%). However, the absolute confidence ellipses should provide a rough estimate of the uncertainties in the parameters. They should also provide a reliable means of comparison of the uncertainties in recovered parameters for different anomalies.

We calculated confidence ellipses for the dipole magnitude and angle relative to the Earth's field, for the anomalies due to 76-mm projectiles and 81-mm mortars at Guthrie Road (Figure 18). The data-weighting matrix was the identity matrix, with a sample standard deviation calculated from the residuals by Equation (53). The figures show the one-sigma (68.3%) and two-sigma (95.4%) confidence ellipses about each recovered dipole moment (assuming Gaussian statistics). For the 76-mm projectiles all except one anomaly have very small uncertainties. The one outlier was incorrectly identified as a 105-mm projectile. For the 81-mm mortars all anomalies have very small uncertainties.

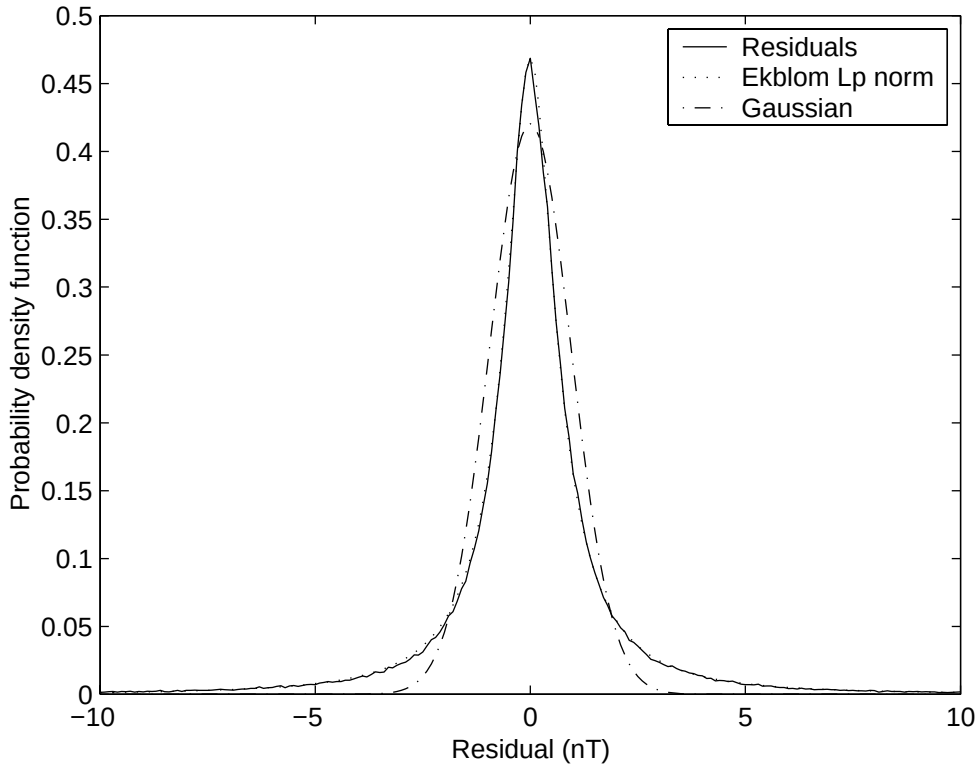

Figure 17: Distribution of residuals for the 660 anomalies at Guthrie Rd with correlation coefficient greater than 0.8.

We also calculated confidence ellipses using the very conservative Bienaymê-Chebyshev inequality (Figure 19). The confidence ellipses are significantly larger than those returned under the normal assumption. If the real confidence ellipses were this large, then uncertainty in the recovered moment would be a contributing factor in misidentifications (especially for 76-mm projectiles). However, the real confidence ellipses would have a size intermediate between the Gaussian and Bienaymê-Chebyshev estimates. This would imply that misidentification is sometimes, though probably not that often, caused by uncertainty in the recovered moment. Misidentifications are more likely to occur due to modelling deficiencies and/or remnant magnetization.

We also calculated confidence ellipses (under the normal assumption) for the anomalies due to metallic debris and geology (Figure 20). For the metallic debris many of the uncertainties are quite low but there are a few items with much higher uncertainties. For the anomalies due to geology the uncertainties are generally much higher. In many cases the recovered angle is around 60^o but the uncertainty is high. This is a critical area for making discrimination decisions so we can conclude that, for geological anomalies, uncertainty in dipole angle can have a significant impact on discrimination.

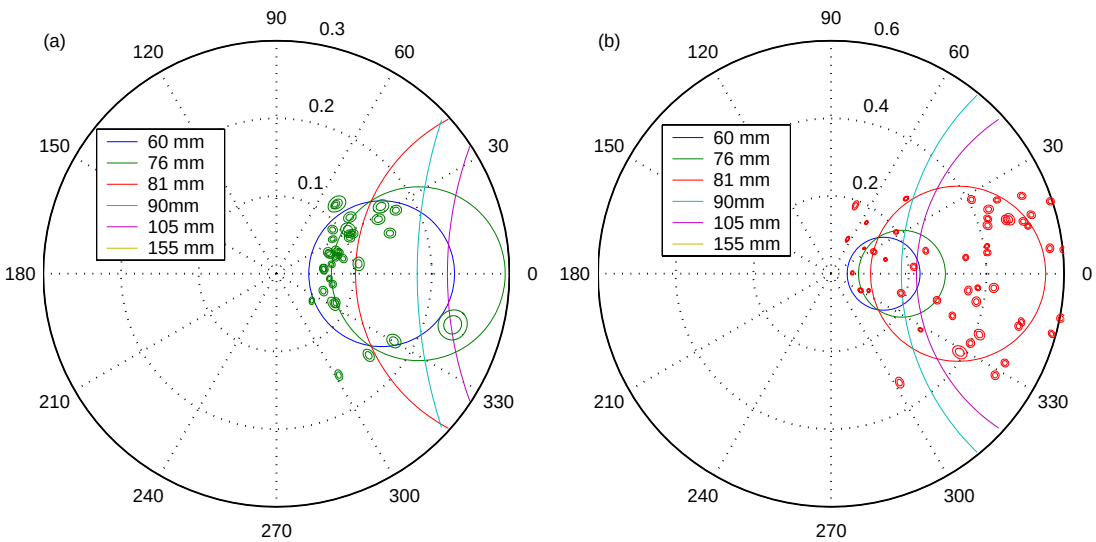

Figure 18: One sigma (68.3%) and two sigma (95.4%) confidence ellipses, assuming Gaussian statistics, about the recovered dipole moments for (a) 76-mm projectiles; and (b) 81-mm mortars.

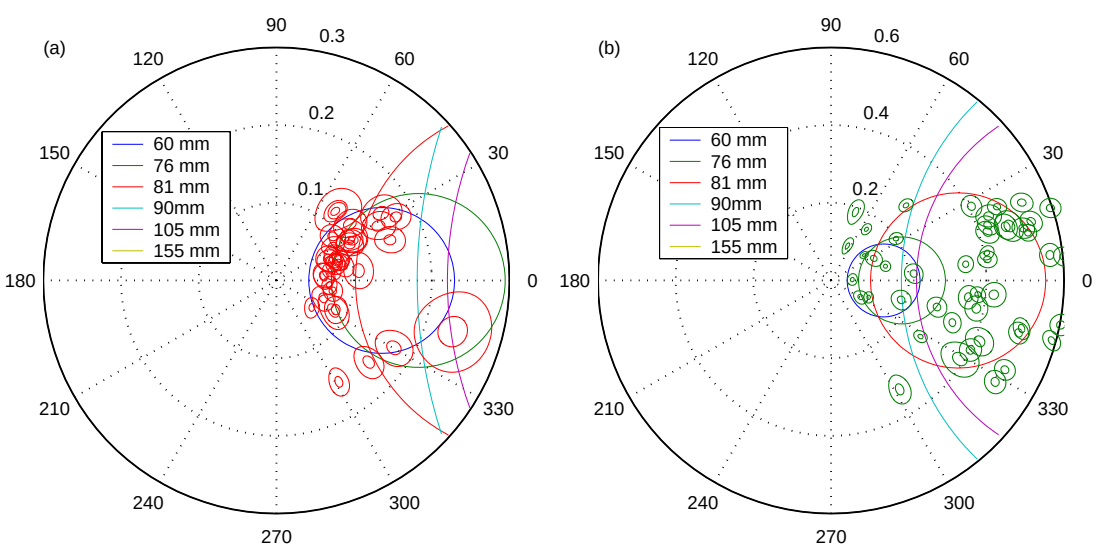

Figure 19: Worst case scenario for one sigma (68.3%) and two sigma (95.4%) confidence ellipses about the recovered dipole moments for (a) 76-mm projectiles; and (b) 81-mm mortars.

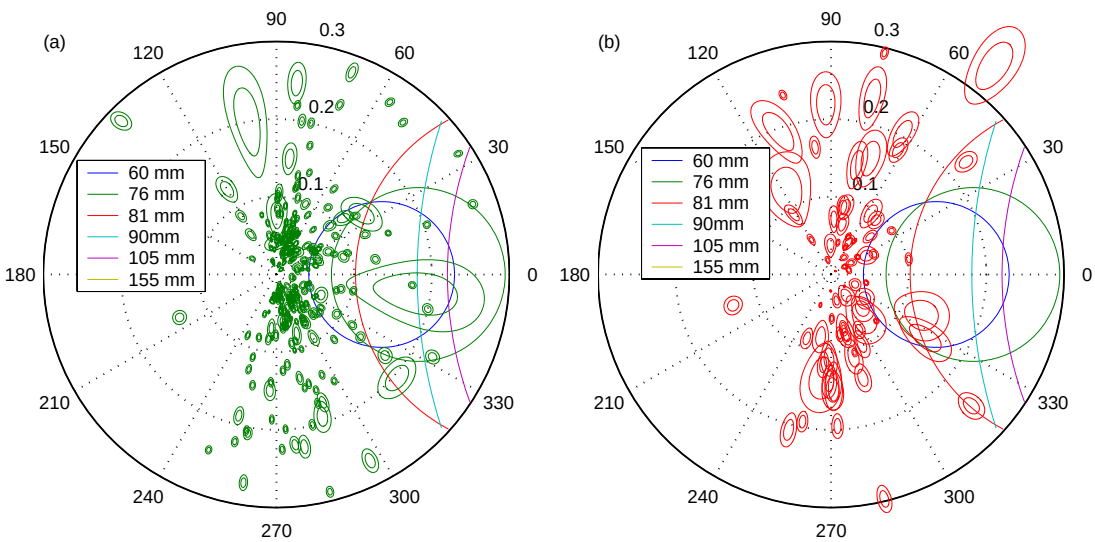

Figure 20: One sigma (68.3%) and two sigma (95.4%) confidence ellipses about the recovered dipole moments for (a) metallic debris; and (b) geological anomalies.

8 Discussion

In this report we have described a successful inversion method for recovering the position and dipole moment from a total-field magnetic anomaly. The inversion uses a least-squares formulation and an interior-reflective Newton method to minimize the objective function. A starting model is defined using an analytical method based on approximating the vertical component of the magnetic field. The inversion method is very fast and reliable; our Matlab implementation requires only a few seconds to recover the parameters for each anomaly.

The recovered dipole moments can be used to make discrimination decisions by recourse to the phenomena of shock demagnetization. Complete shock demagnetization may not occur for all ordnance items all the time. Additionally, non-ordnance, even though they may be remnantly magnetized, might be orientated so that their dipole moments lie close to the Earth's field. This means that it is not possible to make a definitive ordnance/non-ordnance decision. Rather, we prefer to rank anomalies, with items most likely to be UXO higher up the list. We investigated three such ranking procedures; (i) dipole angle, (ii) dipole angle and magnitude and (iii) percentage of remnant magnetism, and found that the remnant magnetization ranking was the best. With this method all ordnance would have been recovered after only half of the anomalies had been excavated. This included 85 anomalies with poor dipole fits that only yielded one UXO. The criterion used to select potential UXO may need to be revised to minimize the number of anomalies where we are unable to make reliable inferences about the bodies origin.

Linearized error analysis indicates that the angle between the recovered dipole moment and the Earth's field for ordnance items is relatively well constrained. Therefore, uncertainty in the recovered dipole moment is unlikely to strongly influence the discrimination ranking. For items identified as geology, the confidence ellipses were much larger. Consequently, the position of these items in the ranking is strongly influenced by uncertainty.

The discrimination method was very successful at Guthrie Road but could not be reliably applied to the seeded sites at Fort Ord. This is a consequence of remnant magnetization and emphasizes the importance of shock demagnetization to the viability of the method. Additional work needs to be undertaken to determine the circumstances where shock demagnetization occurs. For instance, the recovered dipole moments of several of the 81-mm mortars at Guthrie Road had relatively large dipole angles, indicating the presence of some remnant magnetism. Perhaps the lower impact velocity of mortars compared to artillery projectiles causes only partial shock demagnetization; this needs to be investigated further.

Identification of the ordnance type using the recovered dipole moment is difficult due to non-uniqueness. The dipole moment is the product of volume with the magnetization vector. When the volume changes, self-demagnetization as the orientation of the body is varied can change the magnetization vector and thus produce an identical or similar dipole moment. However, recognizing that there are only a finite number of ordnance types in an given area, makes identification using the recovered dipole moment feasible. At Guthrie Road correct identification could be achieved about 55% of the time.

One of the key factors that influences successful identification is obtaining the correct

trajectory of moment magnitude and angle for a given ordnance item. We use a spheroid approximation to calculate this trajectory. Modelling of shapes that more closely approximate real ordnance should be undertaken in order to determine the reliability of the spheroid approximation.

A significant cause of misidentification is the inability of the dipole moment to constrain the orientation of the causative body. In an attempt to overcome this problem we developed inversion routines that recover information on the quadrupole and octupole components of the body. The dipole/octupole method we developed uses a spheroid approximation of ordnance to estimate both the dipole and octupole moments. No significant improvement in identification over the dipole method was found. This could be due to one or more of the following: (i) remnant magnetization; (ii) rapid falloff of the octupole component with distance so that it is unable to constrain the orientation; and (iii) the spheroid provides a poor approximation to the octupole moment of real ordnance.

The quadrupole method relaxed the requirement of top-bottom symmetry enforced by a spheroid approximation and attempted to recover the dipole and quadrupole moments of an arbitrary axially symmetric body. The fits to the data were improved slightly but no advantages for identification were realized. The cause is likely due to one or more of the following: (i) remnant magnetization; (ii) the inability of the quadrupole component to constrain the orientation; and (iii) inadequacy of the model.

The failure of the quadrupole and octupole methods to improve identification may imply that analysis of magnetic data alone does not provide enough information to constrain the objects orientation. One possible method to provide this constraint is by joint inversion of magnetic and electromagnetic data; either single or multiple channel time domain EM or frequency domain EM. Most EM sensors illuminate the target from multiple directions and are consequently more sensitive to orientation (in contrast the direction of the Earth's field is fixed). In return, the magnetics may provide valuable depth constraints that are difficult to obtain with EM alone (Pasion and Oldenburg, 2001).

Linearized error analysis was used to estimate individual parameter uncertainties and joint confidence ellipses. The linear approximation provides an accurate model of the objective function about the minimum. However, the residuals do not follow a Gaussian distribution so that reliable confidence ellipses could not be defined. Additionally, the upper bound provided by the Bienaymê-Chebyshev inequality is very conservative and probably returns confidence ellipses that are much larger than required. A recommendation for future work is to attempt to calculate confidence ellipses using non-Gaussian statistics.

The residuals were found to follow an Ekblom distribution, yet we minimized a measure derived from Gaussian statistics. A reformulation of the problem using an Ekblom distribution as a measure of data misfit is therefore recommended. The resulting objective function would need to be solved by a different optimization algorithm than the one used here. Algorithms for the solution of this optimization problem are well known and include iteratively reweighted least squares and Newton's method (Watson, 1980; Ekblom, 1987). Implementation of the new optimization method would enable a thorough investigation to be made on the influence the choice of the measure of data misfit has on the recovered model. This is an issue often glossed over when solving inverse problems and this report was no exception.

9 Conclusions and Recommendations

A dipole inversion method was developed and successfully applied to the discrimination and identification of magnetic anomalies at Guthrie Road Montana. The discrimination method had the potential to reduce the number of excavations by half, yet still yielded all the ordnance. Identification of the causes of the anomalies is difficult using the recovered dipole moment due to non-uniqueness. However, by recognizing that there are a finite number of ordnance types, correct identification could be achieved in about 55% of cases. Extension of the inversion method to recover either quadrupole of octupole moments did not improve our ability to discriminate or identify.

We recommend the following areas as directions for future research.

1. Shock demagnetization: The extent to which this phenomena occurs should be investigated further because shock demagnetization is central to the success of discrimination using magnetic data.

2. Magnetic modelling of ordnance: The trajectory of the modelled dipole moment magnitude and angle determines our identification decisions. Therefore, the agreement between the moments returned by a spheroid approximation and a more realistic ordnance shape should be investigated further.

3. Joint inversion of magnetics and electromagnetics: Identification difficulties in magnetics are caused by an inability to constrain the orientation of the causative body. The ability of time or frequency domain electromagnetics to constrain the orientation needs to be investigated. Conversely, magnetics may provide valuable depth information that can be exploited by the EM inversion.

4. Error analysis using non-Gaussian statistics: The residuals do not follow a Gaussian distribution so uncertainty estimates based on a more realistic statistical distribution should be investigated.

5. Robust measures of data misfit: The problem should be reformulated using a more realistic measure of data misfit (the Ekblom norm), and methods implemented to solve the modified inversion problem.

10 Bibliography

Altshuler, T. W., 1996, Shape and orientation effects on magnetic signature prediction for unexploded ordnance: Proc. 1996 UXO Forum, 282–291.

Asch, T., and Staes, E. G., 2001, An Ordnance Detection and Discrimination Study at former Fort Ord, CA: Proc. 2001 UXO Forum.

Bard, Y., 1974, Non-linear parameter estimation: Academic Press.

Blakely, R. J., 1996, Potential theory in gravity and magnetic applications: Cambridge University Press.

Branch, M. A., Coleman, T. F., and Li, Y., 1999, A subspace, interior, and conjugate gradient method for large-scale bound-constrained minimization problems: SIAM J. Sci. Comput., **21**, no. 1, 1–23.

Bulter, D. K., Cespedes, E. R., B.Cox, C., and Wolfe, P. J., September 1998, Multisensor methods for buried unexploded ordnance detection, discrimination and identification:, Technical Report 98-10, SERDP.

Clark, P. J., Donaldson, M. W., and Schwartz, T., 1999, ATV Towed magnetometer system for ordnance detection: Proc. 1999 UXO Forum.

Ekblom, H., 1973, Calculation of linear best Lp approximations: BIT, **13**, 293–300.

Ekblom, H., 1987, The L1-estimate as limiting case of an Lp- or Huber-estimate *in* Dodge, Y., Ed., Statistical data analysis based on the L1-norm and related methods:: Elsevier, 109–116.

FAC, 1996, Unexploded ordnance (UXO); An overview: Federal Advisory Committee for the Development of Innovative Technologies.

GAO, 2001, Environmental liabilities, DoD training range cleanup cost estimates are likely underestimated: United States General Accounting Office, Report to the Chairman, Committee on the Budget, House of Representatives, April 2001.

Klaff, T. L., Asch, T., Murray, C., Cormier, M., Staes, E. G., and Peterson, G., 2002, An evaluation of UXO detection instruments through profile comparisons from the Ordnance Detection and Discrimination study at the Former Fort Ord, CA: Proc. SAGEEP.

Lide, D. R., 2001, CRC hanbook of chemistry and physics: CRC Press, 82 edition.

Marquardt, D., 1963, An algorithm for least squares estimation of nonlinear parameters: SIAM J. Appl. Math., **11**, 431–441.

McFee, J. E., and Das, Y., 1986, Fast non-recursive method for estimating location and dipole moment components of a static magnetic dipole: IEEE Trans. Geosci. Rem. Sens., **24**, 663–673.

McFee, J. E., January 1989, Electromagnetic remote sensing; Low Frequency Electromagnetics:, Technical Report 124, Defence Research Establishment Suffield.

Nelson, H. H., Altshuler, T. W., Rosen, E. M., McDonald, J. R., Barrow, B., and Khadr, N., 1998, Magnetic modeling Of UXO And UXO-like targets and comparison with signatures measured by MTADS: Proc. 1998 UXO Forum, 282–291.

Pasion, L. R., and Oldenburg, D. W., 2001, Characterizing unexploded ordnance using time domain electromagnetic induction:, Technical Report ERDC/GSL TR-01-10, U.S. Army Corps of Engineers, Engineer Research and Development Center.

Putnam, J., 2001, Kaho'olawe program management and technology: Proc. UXO Forum.

Roest, W. E., Verhoef, J., and Pilkington, M., 2001, Magnetic interpretation using the 3-D analytic signal: Geophysics, **57**, 116–125.

Stratton, J., 1941, Electromagnetic theory: McGraw Hill.

Watson, G. A., 1980, Approximation theory and numerical methods: John Wiley.

Youmans, C., and Daehn, L., 1999, Quality assurance and quality control in UXO remediation: A case study from Montana: Proc. 1999 UXO Forum.

Appendix A: Multipole Expansion

In this appendix we give a brief derivation of the multipole expansion of a magnetic body, and in particular derive the equations relevant to a spheroid. Our derivations closely follow those given in McFee (1989).

The scalar potential, $\phi(\mathbf{r})$ of a body with magnetization $\mathbf{M}$ is given by

$$\phi(\mathbf{r}) = \frac{1}{4\pi}\int_V \mathbf{M}\cdot\nabla(\frac{1}{r'})dV \tag{A-1}$$

where r' is the distance from the source to the observation point (Figure 1). Expanding the gradient and using the divergence theorem we find

$$\phi(\mathbf{r}) = \frac{1}{4\pi}\left(\int_S \frac{1}{r'}\mathbf{M}\cdot\mathbf{dS} - \int_V \frac{1}{r'}\nabla\cdot\mathbf{M}dV\right) \tag{A-2}$$

If the induced field inside the body is uniform and parallel (which it is for a spheroid), which eliminates the second term in the above equation because then $\nabla\cdot\mathbf{M}=0$. The multipole method proceeds by expanding $\frac{1}{r'}$ as a Taylor series about the origin,

$$\begin{aligned}\phi(\mathbf{r}) \;=\; & \frac{1}{4\pi r}\int_S \mathbf{M}\cdot\mathbf{dS} + \left[\frac{\partial}{\partial x_i}\frac{1}{4\pi r}\right]\int_s x_i\mathbf{M}\cdot\mathbf{dS} + \\ & \left[\frac{\partial^2}{\partial x_i\partial x_j}\frac{1}{4\pi r}\right]\frac{1}{2!}\int_S x_i x_j\mathbf{M}\cdot\mathbf{dS} + \\ & \left[\frac{\partial^3}{\partial x_i\partial x_j\partial x_k}\frac{1}{4\pi r}\right]\frac{1}{3!}\int_S x_i x_j x_k\mathbf{M}\cdot\mathbf{dS} + ...)\end{aligned} \tag{A-3}$$

where repeated indices imply that summation convention is to be used. The scalar potential from a 2^n pole with moment $m^{(n)}_{ij\ldots}$ is given by the expression

$$\phi^{(2^n)} = \frac{m^{(n)}_{ij\ldots}}{4\pi n!}\frac{\partial^n}{\partial x_i\partial x_j\ldots}\left[\frac{1}{r}\right] \tag{A-4}$$

from which it follows that the first four moments are

$$m^{(0)} = \int_S \mathbf{M}\cdot\mathbf{dS} \tag{A-5}$$

$$m^{(1)}_i = \int_S x_i\mathbf{M}\cdot\mathbf{dS} \tag{A-6}$$

$$m^{(2)}_{ij} = \int_S x_i x_j\mathbf{M}\cdot\mathbf{dS} \tag{A-7}$$

$$m^{(3)}_{ijk} = \int_S x_i x_j x_k\mathbf{M}\cdot\mathbf{dS} \tag{A-8}$$

In order the moments are the scalar monopole $m^{(0)}$, the vector dipole $m^{(1)}$, the rank 2 tensor quadrupole $m^{(2)}$, and the rank 3 tensor octupole $m^{(3)}$. Magnetic monopoles do

not exist which means that the monopole term is zero. Expansion of the dipole term reveals that the dipole moment is the product of the magnetization with the volume,

$$\mathbf{m^{(1)}} = \mathbf{M}V \tag{A-9}$$

Due to the symmetry of the spheroid the quadrupole term is zero. After the dipole, the next non-zero term is the octupole; specification of the octupole components is tedious so we refer the interested reader to McFee (1989).

The magnetic field (in the i-th direction) due to the dipole component is given by the expression

$$B_i^{(1)} = \frac{\mu_o}{4\pi r^3}\left(\frac{3}{r^2}[\mathbf{x}\cdot\mathbf{m}^{(1)}]x_i - m_i\right) \tag{A-10}$$

Although zero for the spheroid we will use the quadrupole term later, its field is,

$$B_i^{(2)} = \frac{3\mu_o}{8\pi r^5}\left(-x_i m_{jj}^{(2)} - x_j(m_{ij}^{(2)} + m_{ji}^{(2)}) + 5r^{-2}x_i x_j x_k m_{jk}^{(2)}\right) \tag{A-11}$$

and for the octupole the field is,

$$B_i^{(3)} = \frac{\mu_o}{8\pi r^5}\left(3m_{ijj}^{(3)} - 15r^{-2}\left[x_i x_j m_{jkk}^{(3)} + x_j x_k m_{ijk}^{(3)}\right] + 35r^{-4}x_i x_j x_k x_l m_{jkl}^{(3)}\right) \tag{A-12}$$

It remains to find the magnetization vector for a spheriod. A solution of the boundary value problem (Stratton, 1941) shows that the demagnetization factors are

$$F_i = \frac{\mu_r - 1}{1 + \alpha_i(\mu_r - 1)/2} \tag{A-13}$$

where μ_r is the relative permeability ($\mu = \mu_r\mu_o$),

$$\alpha_1 = \alpha_2 = \frac{e(e+E)}{e^2-1} \tag{A-14}$$

and

$$\alpha_3 = \frac{-2e(e^{-1}+E)}{e^2-1} \tag{A-15}$$

with

$$E = \frac{\log(e - \sqrt{e^2-1})}{\sqrt{e^2-1}} \tag{A-16}$$

for a prolate spheroid ($e > 1$) and

$$E = \frac{\arctan(\frac{e}{\sqrt{1-e^2}}) - \pi/2}{\sqrt{1-e^2}} \tag{A-17}$$

for an oblate spheroid ($e < 1$). For the special case of a sphere ($e = 1$) then

$$\alpha_1 = \alpha_2 = \alpha_3 = \frac{2}{3} \tag{A-18}$$

The demagnetization factors together with the Earth's field $\mathbf{B_o}$ (in spheroid centered coordinates), determine the strength of the induced magnetization,

$$\mathbf{M} = \mu_o^{-1}\mathbf{F}\mathbf{B_o} \tag{A-19}$$

where we have written $\mathbf{F}$ as a 3×3 diagonal matrix with (F_2, F_2, F_3) along the diagonal (because $F_1 = F_2$).

Multipole expansion for an axi-symmetric body

In going from the general equation (A-2) for a magnetized body to that for a spheroid, we used the fact that the magnetization inside the body was constant so that $\nabla \cdot \mathbf{M} = 0$. For a general axi-symmetric body this is no longer true and there is an extra contribution to each of the moments. For the dipole,

$$m_i^{(1)} = \int_S x_i \mathbf{M} \cdot \mathbf{dS} - \int_V x_i \nabla \cdot \mathbf{M} dV \tag{A-20}$$

and using the identity

$$\int_V \phi \mathbf{M} \cdot \nabla \phi dV = \int_S \phi \mathbf{M} \cdot \mathbf{dS} - \int_V \phi \nabla \cdot \mathbf{M} dV, \tag{A-21}$$

we find

$$\begin{aligned} m_i^{(1)} &= \int_V \mathbf{M} \cdot \nabla x_i dV \\ &= \int_V M_i dV \end{aligned} \tag{A-22}$$

Thus the dipole moment is just the integration of the magnetization over the volume of the body. Most ordnance items are either cylinder like with a pointed front (e.g. most artillery projectiles) or close to a spheroid shape (e.g. mortars, the fins can be ignored as they are usually aluminum). For an infinite cylinder the field lines are constant within the body. Therefore, for a projectile any changes in magnetization will be concentrated at the ends of the body, and will generally make only a small contribution to the multipole moments. For a mortar, the shape is close to second order (Stratton, 1941) and hence the magnetization direction will be approximately constant. Thus, changes in magnetization direction should not make a significant contribution to the observed magnetic anomaly.

Using an analogous development to the dipole, the quadrupole moment can be shown to be equal to

$$\begin{aligned} m_{ij}^{(2)} &= \int_V \mathbf{M} \cdot \nabla (x_i x_j) dV \\ &= \int_V (M_i x_j + M_j x_i) dV \end{aligned} \tag{A-23}$$

Assuming that changes in magnetization can be ignored implies that

$$m_{ij}^{(2)} = M_i \int_L dx_3 \int_{S(x_3)} x_j dS + M_j \int_L dx_3 \int_{S(x_3)} x_i dS \tag{A-24}$$

where L is the length of the body parallel to the symmetry axis, $z = x_3$ and $S(x_3)$ is a slice of the body perpendicular to the axis of symmetry. Due to symmetry each of the integrals over $S(x_3)$ are zero for i or $j = 1$ or 2, from which it follows that

$$m_{ij}^{(2)} = 0 \quad \text{for any } i, j = 1 \text{ or } 2 \tag{A-25}$$

The quadrupole moment is symmetric $m_{ij}^{(2)} = m_{ji}^{(2)}$ so that the full moment tensor can then be written as (where we have dropped the (2) subscript),

$$\mathbf{M} = \begin{bmatrix} 0 & 0 & m_{13} \\ 0 & 0 & m_{23} \\ m_{13} & m_{23} & m_{33} \end{bmatrix} \tag{A-26}$$

Appendix B: Constraints on Dipole Orientation

The angle the induced dipole moment in a spheroid makes with the Earth's field cannot exceed a certain value. In this appendix we derive the equations which specify this upper bound. We assume the Earth's field is at an angle θ to the spheroid symmetry axis and align the z-axis of our coordinate system with the symmetry axis. We can then choose the x-axis so that it is perpendicular to the Earth's field. In this coordinate system

$$\mathbf{b_o} = b_o(0, \sin\theta, \cos\theta)^T \tag{B-1}$$

The spheroid diameter a and aspect ratio e determine the demagnetization factors, F_2 and F_3, so that the induced dipole moment $\mathbf{m}$ is,

$$\mathbf{m} = V\ b_o(0, F_2 \sin\theta, F_3 \cos\theta)^T \tag{B-2}$$

where V is the volume of the spheroid. The angle ψ between the Earth's field and the dipole moment is

$$\cos\psi = \frac{\mathbf{b_o} \cdot \mathbf{m}}{\|\mathbf{b_o}\|\|\mathbf{m}\|} \tag{B-3}$$

which, on substitution of Equations (B-1) and (B-2), becomes

$$\cos\psi = \frac{F_2 \sin^2\theta + F_3 \cos^2\theta}{\sqrt{F_2^2 \sin^2\theta + F_3^2 \cos^2\theta}} \tag{B-4}$$

After differentiating this equation by θ, setting the result to zero and extensive algebraic manipulation we find

$$\theta = \arctan\left(\sqrt{\frac{F_3^3 + F_3 F_2^2 - 2F_2 F_3^2}{F_2^3 + F_2 F_3^2 - 2F_3 F_2^2}}\right) \tag{B-5}$$

This orientation of the spheroid symmetry axis relative to the Earth's field makes the angle between the induced dipole and the Earth's field a maximum. This maximum angle is obtained by substituting Equation (B-5) into Equation (B-4).

Appendix C: Ambiguity in the Dipole Solution

Once the sensor distance exceeds a few body lengths distance away from the spheroid, the field is essentially dipolar. In such cases, inversion for spheroid dimensions has an inherent ambiguity: many different spheroid diameters and aspect-ratios can reproduce the observed dipole. To characterize this ambiguity we chose our coordinate system so that the z-axis is aligned with the Earth's field,

$$\mathbf{B_o} = (0, 0, B_o)^T \tag{C-1}$$

We want to determine if the dipole $\hat{\mathbf{m}}$ from a particular spheroid (diameter a and aspect-ratio e) can match an observed dipole moment $\mathbf{m}$. Now the induced dipole for the spheroid is given by the following equation

$$\hat{\mathbf{m}} = V\mathbf{A}^T\mathbf{F}\mathbf{A}\mathbf{B_o} \tag{C-2}$$

Expanding this equation we find

$$\hat{\mathbf{m}} = \frac{B_o \pi e a^3}{6\mu_o} \begin{bmatrix} (F_2 - F_3)\cos\theta\sin\theta\sin\psi \\ (F_2 - F_3)\cos\theta\sin\theta\cos\psi \\ F_2\cos^2\theta + F_3\sin^2\theta \end{bmatrix} \tag{C-3}$$

Now we want to find a, e, θ and ψ so that $\hat{\mathbf{m}} = \mathbf{m}$. We can find an expression for the spheroid diameter by equating the norms of the two dipole moments, resulting in

$$a^3 = \frac{6\mu_o\|\mathbf{m}\|}{B_o\pi e\sqrt{F_2^2\cos^2\theta + F_3^2\sin^2\theta}} \tag{C-4}$$

For ψ we use,

$$\frac{m_1}{m_2} = \frac{\hat{m}_1}{\hat{m}_2} = \frac{\sin\psi}{\cos\psi} = \tan\psi \tag{C-5}$$

which leads to

$$\psi = \arctan\left(\frac{m_1}{m_2}\right) \tag{C-6}$$

This implies that the spheroid has the same azimuth as the dipole moment.

Determination of θ is a little more difficult. We start by using the second row of Equation (C-3) and substitute in Equation (C-4) for the diameter,

$$\frac{m_2}{\cos\psi\|\mathbf{m}\|} = \frac{(F_2 - F_3)\cos\theta\sin\theta}{\sqrt{F_2^2\cos^2\theta + F_3^2\sin^2\theta}} \tag{C-7}$$

Note that if $\cos\psi = 0$ we would use the first row of Equation (C-3) to derive an equation in terms of m_1 and $\sin\psi$. Let the LHS of Equation (C-7) be ω, expand out the square-root on the denominator of the RHS, and use the substitution

$$\sin^2\theta = 1 - \cos^2\theta \tag{C-8}$$

After some algebraic manipulation Equation (C-7) reduces to

$$(F_2 - F_3)^2 \cos^4\theta \left[\omega^2(F_2^2 - F_3^2) - (F_2 - F_3)^2\right] \cos^2\theta + \omega^2 F_3^2 \tag{C-9}$$

This is a quadratic equation in $\cos^2\theta$ which has a real solution if

$$\Delta = \hat{b}^2 - 4\hat{a}\hat{c} \geq 0 \tag{C-10}$$

where

$$\hat{a} = (F_2 - F_3)^2 \tag{C-11}$$
$$\hat{b} = \omega^2(F_2^2 - F_3^2) - (F_2 - F_3)^2 \tag{C-12}$$
$$\hat{c} = \omega^2 F_3^2 \tag{C-13}$$

The solution in terms of θ is then

$$\theta = \pm \arccos\left(\sqrt{\frac{-\hat{b} \pm \sqrt{\Delta}}{2\hat{a}}}\right) \tag{C-14}$$

The $\pm$ terms in the above equation emphasize that when $\Delta > 0$ there are actually two possible solutions.

Determination of which spheroids can reproduce the observed dipole proceeds as follows. Firstly, we chose an aspect-ratio e and calculate the demagnetization factors in the usual way. We then substitute Equations (C-11) to (C-13) into Equation (C-10) to determine if a solution can be found for this aspect-ratio. If it can, we calculate θ by Equation (C-14), and finally we calculate the spheroid diameters (usually there will be two) by Equation (C-4).

REPORT DOCUMENTATION PAGE

Form Approved
OMB No. 0704-0188

1. REPORT DATE *(DD-MM-YYYY)*	2. REPORT TYPE	3. DATES COVERED *(From - To)*
September 2002	Final report	

4. TITLE AND SUBTITLE

Discrimination and Identification of UXO by Geophysical Inversion of Total-Field Magnetic Data

5a. CONTRACT NUMBER

5b. GRANT NUMBER
41262-ev

5c. PROGRAM ELEMENT NUMBER

6. AUTHOR(S)

Stephen D. Billings, Leonard R. Pasion, and Douglas W. Oldenburg

5d. PROJECT NUMBER

5e. TASK NUMBER

5f. WORK UNIT NUMBER
AF25, 6.2

7. PERFORMING ORGANIZATION NAME(S) AND ADDRESS(ES)

Geophysical Inversion Facility
Department of Earth and Ocean Sciences
University of British Columbia
Vancouver, B.C., V6T 1Z4, Canada

8. PERFORMING ORGANIZATION REPORT NUMBER

ERDC/GSL TR-02-16

9. SPONSORING / MONITORING AGENCY NAME(S) AND ADDRESS(ES)

U.S. Army Engineer Research and Development Center
Geotechnical and Structures Laboratory
3909 Halls Ferry Road, Vicksburg, MS 39180-6199;
U.S. Army Corps of Engineers
Washington, DC 20314-1000

10. SPONSOR/MONITOR'S ACRONYM(S)

11. SPONSOR/MONITOR'S REPORT NUMBER(S)

12. DISTRIBUTION / AVAILABILITY STATEMENT

Approved for public release; distribution is unlimited.

13. SUPPLEMENTARY NOTES

14. ABSTRACT

A dipole inversion method was developed and successfully applied to the discrimination and identification of unexploded ordnance using total-field magnetometry. A black-white classification of anomalies as ordnance/nonordnance is not possible using magnetics because some nonordnance items are indistinguishable from UXO. We found that the best strategy is to rank items according to the likelihood they are UXO. This ranking can be achieved by several methods: the best was to rank on the basis of the amount of remnant magnetization required to make the anomaly match one of the ordnance items in a predefined library. The discrimination method had the potential to reduce the number of excavations at an impact site in Montana (Guthrie Road) by half, yet still yielded all the ordnance. The method requires complete or a least partial shock demagnetization of ordnance, otherwise it is not possible to reliably rank the anomalies.

Error analysis indicated that recovered dipole moments are relatively well constrained. However, identification of the anomaly source is difficult using the recovered dipole moment due to nonuniqueness. The dipole moment is the product of magnetization with volume, and a change in volume can be compensated by a change in magnetization by varying the orientation of the item relative to the

(Continued)

15. SUBJECT TERMS

Discrimination
Geophysics
Inversion
Unexploded ordnance

16. SECURITY CLASSIFICATION OF:			17. LIMITATION OF ABSTRACT	18. NUMBER OF PAGES	19a. NAME OF RESPONSIBLE PERSON
a. REPORT	b. ABSTRACT	c. THIS PAGE			19b. TELEPHONE NUMBER *(include area code)*
UNCLASSIFIED	UNCLASSIFIED	UNCLASSIFIED		56	

14. (Concluded)

Earth's field. By recognizing that there is a finite number of ordnance types, correct identification at Guthrie Road could by achieved about 55 percent of the time. Attempts to constrain the orientation (and hence ordnance dimension) by recovering higher-order moments (quadrupole and octupole) of the body did not improve our ability to discriminate or identify.

Destroy this report when no longer needed. Do not return it to the originator.

1 Introduction

Unexploded ordnance pose a significant public safety hazard in many parts of the world. They occur on or near the surface and down to depths of several meters below the ground. One source of UXO's are armed conflicts both old and more recent in regions such as Europe (World Wars I and II), South-East Asia, Afghanistan, Yugoslavia and parts of Africa. They are also a significant problem in countries such as Canada and the United States, where they are present in areas used for military training and firing ranges; largely as vestiges of World War II and the Cold War. It is estimated that 15 million acres of the United States are contaminated by UXO (FAC, 1996), with a clean-up time-frame in the decades and a staggering cost estimate, using existing technology, in the tens to hundreds of billions of dollars (GAO, 2001).

The most well established techniques for ordnance detection are magnetics and electromagnetics (Bulter et al., 1998). These methods are very effective at locating buried metallic objects such as UXO. However, discriminating between intact UXOs and uninteresting objects such as metallic debris and shrapnel is a significant challenge (Bulter et al., 1998). Often little or no effort is invested in discrimination and, consequently, many holes are excavated for each ordnance item recovered. For example, Putnam (2001) reports that from 49,521 anomalies excavated at Kaho'olawe, Hawaii, only 3% (or 1,486) turned out to be UXO. In this report we analyze magnetics data collected at Guthrie Road, Helana Valley, Montana (Youmans and Daehn, 1999). 840 holes were excavated with 83 UXOs recovered, thus there was a 10% success rate. It is perhaps a reflection of the state of our ability to discriminate that this survey was considered a success by all parties involved.

The simplest form of discrimination is to threshold the collected data in some way (for magnetics this is usually achieved by first calculating the analytic signal and then thresholding, Roest et al. (2001)). As the threshold level is decreased, the number of items that need to be excavated increases. As demonstrated by the Ordnance Detection and Discrimination Study at the Former Fort Ord (Asch and Staes, 2001), for such techniques to yield a high probability of detection, a very high false alarm rate results.

Location of UXOs involves the successful detection and identification of compact metallic objects. Therefore, a better method for discrimination is to parameterize the characteristics of the target in some way (e.g. by its location, orientation, shape, size and material properties) and develop a good forward model that allows predicted data to be generated from a given target realization. Inversion can then be used to find the set of target parameters that best fits the data. The target parameters are then used to make decisions regarding discrimination (UXO versus non-UXO) and identification (what is the ordnance type).

A previous report (Pasion and Oldenburg, 2001) considered the development of an inversion methodology for time-domain electromagnetic data. In this report, we consider the development of a methodology for total-field magnetics data. Previous work in this area has been conducted by (amongst others) the Canadian Defence Research Establishment (McFee, 1989) and the Naval Research Laboratory (Nelson et al., 1998) and private companies.

Spheroids have been proposed as an approximate parameterization of ordnance by several authors (McFee, 1989; Altshuler, 1996; Bulter et al., 1998). While the spheroid

does not capture the top-bottom asymmetry of many ordnance items, close agreement between observed anomalies over test stands and spheroid fits have been demonstrated (McFee, 1989; Bulter et al., 1998). Furthermore, the magnetic anomaly from a solid spheroid has been shown to be very similar to a hollow spheroid (Altshuler, 1996). Therefore, we will use solid spheroids as the basis of our magnetic modelling of UXO's.

The response of a spheroid (in fact any compact body) can be decomposed into a series of moments by a multipole expansion (Stratton, 1941). The response of the dipole component dominates the anomalies caused by most buried ordnance due to the rapid falloff with distance of the other components. Consequently, the main inversion routine developed in this report attempts to recover the dipole moment and position that best matches an observed anomaly. The recovered dipole moment is then used to rank items according to the likelihood they are UXO. We prefer such a ranking over a definitive statement such as ordnance or non-ordnance because it is not possible to make such a black and white distinction.

The recovered dipole moment can also be used for ordnance identification. There is some ambiguity in this process because the dipole moment is the product of magnetization with volume. Due to self-demagnetization effects the magnetization can change significantly as the orientation of the body relative to the Earth's field changes. Thus orientation can be traded with volume to produce the same or similar dipole moment. By recognizing that there are a finite number of ordnance types present in an area (we build up a library), this ambiguity can be reduced significantly.

To attempt to constrain the orientation we develop two further inversion routines. The first uses the octupole component of the spheroid, and finds the optimum orientation and fit for each of the items in our library. That item with the best fit is assumed to be the source of the anomaly. The second method aims to recover the dipole and quadrupole moments of an arbitrary axially symmetric body.

No inversion methodology would be complete without an analysis of the uncertainties in the recovered parameters. The last section of the report considers the development of a linearized error analysis. We also investigate the distribution of the residuals so that we can test our assumption of Gaussian statistics.

2 Magnetic field of a spheroid

The forward modelling task may be stated as follows; calculate the magnetic anomaly at the arbitrary point $(\hat{x}, \hat{y}, \hat{z})$ given a spheroid of diameter a, aspect ratio e (i.e. $length = ae$) and permeability μ oriented at an angle of θ degrees to the horizontal with an azimuth of ϕ degrees clockwise from North, at a depth z below the surface and at the horizontal position (x, y). The geometry of this situation is shown in Figure 1. Full characterization of the anomaly caused by a spheroid requires the Earth's field plus the eight parameters $(x, y, z, \theta, \phi, a, e, \mu)$. For the Earth's field we use geographical coordinates; $\mathbf{B_o} = (B_{ox}, B_{oy}, B_{oz})$, i.e. x is positive to the East, y is positive to the North and z is positive upwards. Note that this differs from the definition used to specify the International Geomagnetic Reference Field (IGRF) where x is positive to the North, y is positive to the East and z is positive downwards.

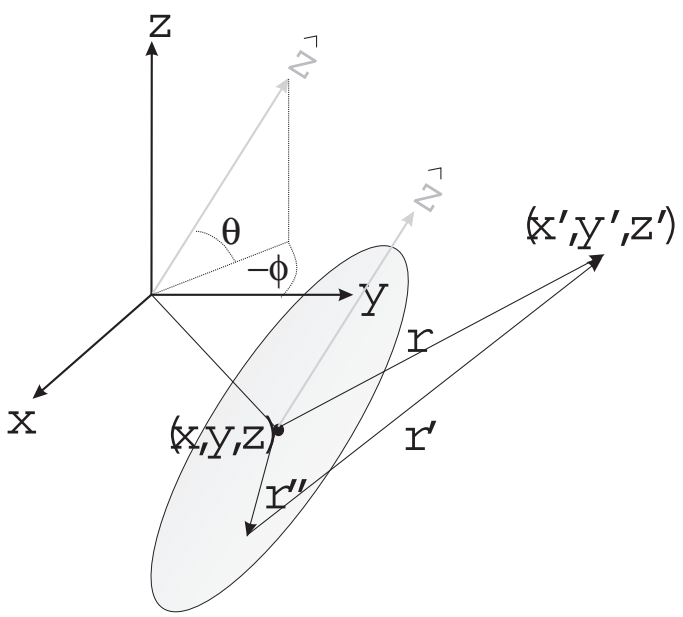

Figure 1: Geometry for modelling the response of a spheroid.

The magnetic anomaly of a buried ferrous item arises from both remnant $\mathbf{M}_{rem}$ and induced magnetization $\mathbf{M}_{in}$; the total magnetization $\mathbf{M}$ is then

$$\mathbf{M} = \mathbf{M}_{rem} + \mathbf{M}_{in} \tag{1}$$

Remnant magnetism is present even in the absence of an inducing field and is due to magnetic moments being locked into alignment once the steel casing cools to below the Curie temperature in the presence of an external field. We will discuss this type of magnetism latter but for now we will concentrate on the induced magnetism that arises because magnetic domains in a ferrous material tend to align with the direction of the Earth's field. The ease with which the moments align, and hence the strength of the magnetism, depends on the magnetic permeability of the steel. For a compact body such as a spheroid, demagnetization effects become important. This phenomena refers

to the extent that the induced field is reduced due to the shape of the spheroid. It arises due to the boundary conditions that the field must satisfy across a discontinuity in magnetic permeability. A solution of the boundary value problem (Stratton, 1941) shows that the demagnetization factors are

$$F_i = \frac{\mu_r - 1}{1 + \alpha_i(\mu_r - 1)/2} \tag{2}$$

where μ_r is the relative permeability ($\mu = \mu_r \mu_o$, where $\mu_o = 4\pi \times 10^{-7}$ H/m is the permeability of free space) and the α_i's are factors which depend on the shape of the spheroid (see Appendix A). Once the relative permeability exceeds a few hundred units, the induced magnetization becomes virtually independent of susceptibility. This can easily be seen from Equation 2 with large μ_r because then

$$F_i \approx \frac{2}{\alpha_i} \tag{3}$$

This allows us to eliminate μ_r from our calculations because steel typically has susceptibilities of several hundred to over a thousand (Lide, 2001).

The demagnetization factors, together with the Earth's field $\hat{\mathbf{B}}_\mathbf{o}$ (in spheroid centered coordinates), determine the strength of the induced magnetization,

$$\hat{\mathbf{M}}_{in} = \mu_o^{-1} \mathbf{F} \hat{\mathbf{B}}_\mathbf{o} \tag{4}$$

where we have written $\mathbf{F}$ as a 3×3 diagonal matrix with (F_2, F_2, F_3) along the diagonal (remember $F_1 = F_2$). An important consequence of demagnetization is that the induced magnetism can change significantly with orientation. For instance, with $e = 4$ we find $F_2 = 2.1$ and $F_3 = 12.7$, so that the magnetization when the spheroid semi-major axis is aligned with the field is approximately 6 times greater than when it is perpendicular.

Equation 4 returns $\hat{\mathbf{M}}_{in}$ in spheroid centered coordinates and assumes $\hat{\mathbf{B}}_\mathbf{o}$ is also spheroid centered. To use geographical coordinates we utilize the Euler rotation tensor

$$\mathbf{A} = \begin{bmatrix} \cos\psi & -\sin\psi & 0 \\ \sin\theta\sin\psi & \sin\theta\cos\psi & \cos\theta \\ \cos\theta\sin\psi & \cos\theta\cos\psi & -\sin\theta \end{bmatrix} \tag{5}$$

to rotate $\mathbf{B_o}$ to spheroid centered coordinates and then use its inverse $\mathbf{A}^T$ to rotate $\hat{\mathbf{M}}_{in}$ to geographical coordinates,

$$\mathbf{M}_{in} = \mu_o^{-1} \mathbf{A}^T \mathbf{F} \mathbf{A} \mathbf{B_o} \tag{6}$$

With this uniform magnetization, the magnetic field of the spheroid is given by the expression

$$\mathbf{B} = \frac{1}{4\pi} \int_S \frac{1}{r'} \mathbf{M}_{in} \cdot \mathbf{dS} \tag{7}$$

where r' is the distance from the source to the observation point (Figure 1). An exact solution of this equation using prolate spheroidal harmonics is known (Stratton, 1941) but we chose to use a multipole expansion; the details can be found in Appendix A and McFee (1989). The first non-zero moment is the dipole $\mathbf{m}$ which is given by

$$\mathbf{m} = V \mathbf{M}_{in} = \frac{\pi}{6} e a^3 \mathbf{M}_{in} \tag{8}$$

where V is the volume of the spheroid. The magnetic field from the dipole term is then

$$\mathbf{B} = \frac{\mu_o}{4\pi r^3}\left(\frac{3}{r^2}[\mathbf{x}\cdot\mathbf{m}]\mathbf{x} - \mathbf{m}\right) \tag{9}$$

The octupole is the next non-zero moment and is a rank 3 tensor with 27 components. Symmetry reduces the number of independent components to 6. The specification of the octupole term is quite complicated, so we leave the details to Appendix A and just note that its field dies off as r^{-5}.

The rapid falloff of the octupole term with distance means that once the sensor distance exceeds a few body lengths, the field is essentially dipolar. For example, Figure 2a plots the dipole and octupole fields from a spheroid model of a 105-mm ordnance ($a = 0.105$ m, $e = 3.7$) orientated at 45^o to the vertical, along horizontal lines at a height of ae and $2ae$ above the ordnance. The responses are normalized by the maximum dipole response at that height. At a height of ae the peak of the octupole term is a little over 15% of the peak of the dipole term. For the height $2ae$ the octupole peak is less than 5% the size of the dipole peak. Figure 2b shows how this ratio rapidly decreases with increasing height above the ordnance.

Considering that real magnetic profiles are contaminated by noise, observing the octupole response in the presence of the dipole response will generally be very difficult. It may be possible when the sensor is very close to the ordnance, or when the noise levels are low and the spatial positioning extremely accurate. We now examine the consequence of the dipolar nature of the observed fields on both discrimination and identification.

Discrimination using magnetometry

The induced dipole moment of a sphere is constrained to lie in the direction of the applied field. On the other hand, the angle the induced dipole moment of a spheroid makes with the Earth's field will vary with its orientation. The angle ψ between the induced moment and the applied field will be (see Appendix B)

$$\psi = \arccos\left[\frac{F_2\sin^2\theta + F_3\cos^2\theta}{\sqrt{F_2^2\sin^2\theta + F_3^2\cos^2\theta}}\right] \tag{10}$$

where θ is the angle of the spheroid semi-major axis with the Earth's field and F_2 and F_3 are the demagnetization factors of the spheroid. In Figure 3a we show the variation in the angle ψ as the orientation θ changes for a spheroid with an aspect-ratio of 5. The angle ψ achieves a maximum value that depends on the shape of the spheroid. For a given aspect ratio, the spheroid orientation θ that results in the maximum value for ψ is (see Appendix B)

$$\theta = \arctan\left(\sqrt{\frac{F_3^3 + F_3F_2^2 - 2F_2F_3^2}{F_2^3 + F_2F_3^2 - 2F_3F_2^2}}\right) \tag{11}$$

The maximum angle for a given aspect ratio is then obtained by substituting Equation (11) into (10). The variation of this maximum angle with shape is shown in Figure 3b. Most UXO's have eccentricities between 3 and 7, so that 55^o is an upper bound on the angle. This suggests a possible method for discrimination (Altshuler, 1996).

When an ordnance hits the ground but does not explode, the impact is usually sufficient to cause shock demagnetization; the shock of impact causes magnetic domains

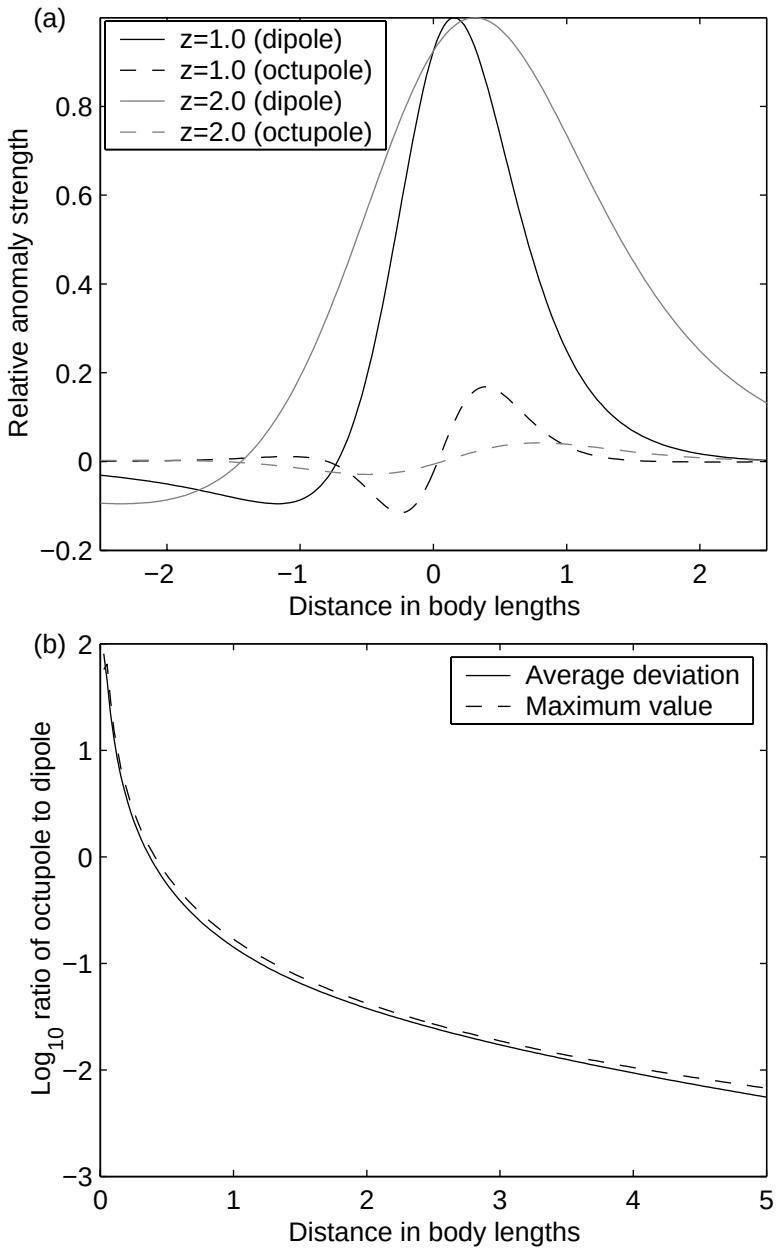

Figure 2: (a) Dipole and octupole terms at one and two body lengths distance; (b) Log_{10} of the ratio of the octupole to dipole terms for a 105-mm projectile at 45^o inclination

within the ordnance to become randomly aligned, thus erasing any remnant magnetization. On the other hand, when the ordnance explodes, the shrapnel is heated, deformed and cooled in the presence of the Earth's field and can acquire permanent magnetism. Putting all of the above together, it is conjectured that ordnance should not have a dipole moment that exceeds an angle of 60^o from the Earth's field. The success of this method of discrimination in reducing false alarms has been demonstrated in Nelson et al. (1998). However, they did note that subsequent events (such as lightning strikes)

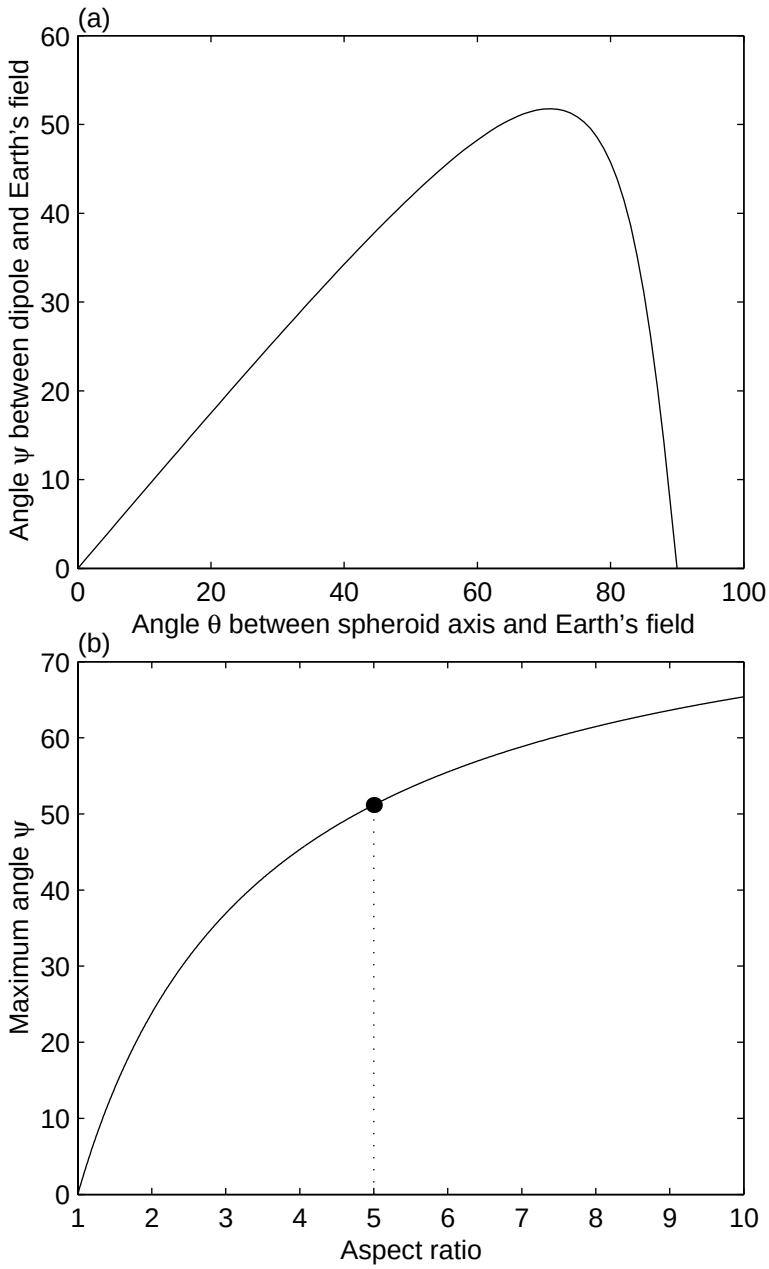

Figure 3: (a) Change in the moment angle as the orientation varies for an aspect ratio of 5; and (b) Maximum angle between the induced dipole moment of a spheroid and the Earth's field

can cause the ordnance to acquire a remnant magnetization and hence degrade the performance of the discrimination method. Also, the assumption that ordnance are fully demagnetized on impact may be violated in practice. We shall return to this point later, but for now assume that the initial conjecture is valid.

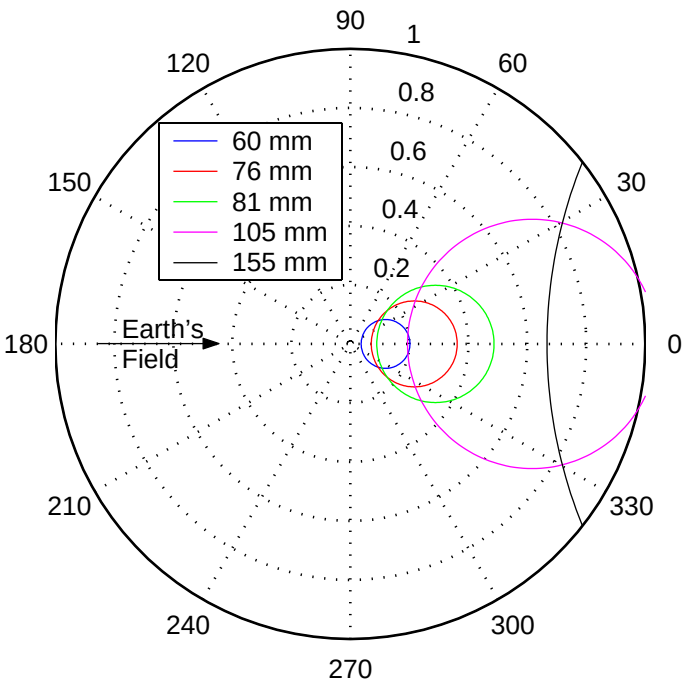

Figure 4: Magnitude of dipole moment (Am^2) and angle from Earth's field for 60, 76, 81, 105 and 155-mm projectiles

Ordnance identification using magnetometry

We now turn to the issue of identifying (or classifying) ordnance items from their dipole field. For a given spheroid, the induced dipole moment will be dependent on the angle θ that the spheroid axis makes with the Earth's field. There is no azimuthal dependence due to the spheroid's symmetry. By varying the orientation θ we are able to trace the change in dipole magnitude and angle with respect to the applied field. Figure 4 shows these curves as polar plots for five different ordnance items; a 60-mm mortar, a 76-mm projectile, an 81-mm mortar, a 105-mm projectile and a 155-mm projectile. Fitting a dipole to observed data will produce a single point in this polar plot that needs to be matched to an ordnance item. The curves for the 76-mm projectile and the 81-mm mortar are very similar in certain parts of the plot, indicating that discriminating between these items may be very difficult. Further, certain orientations lead to identical dipole moments of both these items to the 60-mm mortar and the 105-mm projectile.

The analysis in the last paragraph indicates that there can be ambiguity in identification using magnetometry. This fact is rigorously established in Appendix C where it is shown that for a given spheroid at a particular orientation, there are an infinite number of other spheroids that could have produced the same dipole moment. For example, Figure 5 and Table 1 show the family of spheroids that can produce the same dipole moment as a 105-mm projectile orientated at 45^o to the Earth's field. The 90-mm projectile lies very close to this curve emphasizing the difficulty in separating these two items. The folding over of this curve to encompass spheroids of larger dimension is of more concern to classification; the 155-mm lies quite close to this branch of the curve.

There is also a family of oblate spheroids that could produce the same dipole moment; as could objects of different shapes. This inherent ambiguity has a significant impact on the methods we develop for ordnance classification in the remainder of this report.

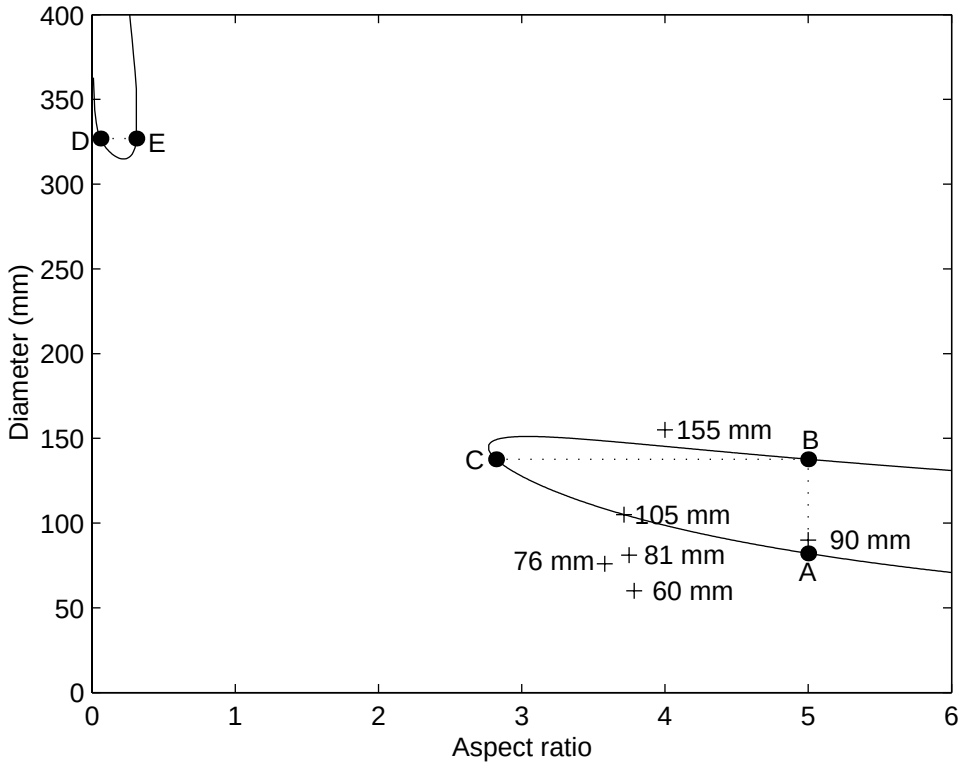

Figure 5: Spheroid dimensions that can produce the same dipole as a 105-mm shell at 45^o inclination to the Earth's field. The dimensions and orientation angles corresponding to the labelled points are shown in Table 1.

	Diameter (mm)	**Aspect ratio**	**Angle (degrees)**
A	82	5	40.5
B	138	5	84.0
C	138	2.82	57.2
D	327	0.06	53.4
E	327	0.31	33.4

Table 1: Spheroid dimensions, and their angles relative to the Earth's field, that produce the same dipole moment as a 105-mm projectile at 45^o inclination.

3 Inversion method for parameter estimation

The previous section demonstrated that, in many situations, it would be difficult to recover more than the dipole component of a spheroid's magnetic anomaly. Therefore, rather than attempting a direct inversion for the spheroid location and dimension, we apply a two-step procedure:

1. Invert for the best-fitting dipole moment and location;
2. Use the recovered dipole moment for discrimination and ordnance identification.

Due to possible difficulties in properly removing the regional and local geologically derived fields from a magnetic survey, we also allow for a dc-shift in our dipole model; this means that seven parameters are required to characterize each anomaly.

Inversion goal: Find the location $\mathbf{x} = (x, y, z)$, dipole moment $\mathbf{m} = (m_x, m_y, m_z)$ and dc-shift d, that produces the best fit to a set of N total-field observations, $\{d^{obs}(\mathbf{x}_i), i = 1, \ldots, N\}$.

We follow the usual convention in inverse problems and use $\mathbf{m}$ to specify the seven model parameters (it should be clear from the context whether $\mathbf{m}$ refers to the model parameters or the dipole moment). We formulate the inverse problem as a weighted, least-squares optimization procedure where the goal is to solve

$$\min_{\mathbf{m} \in \Re^n} \phi(\mathbf{m}) \tag{12}$$

The objective function is

$$\phi(\mathbf{m}) = \frac{1}{2}(F(\mathbf{m}) - \mathbf{d}^{obs})^T W (F(\mathbf{m}) - \mathbf{d}^{obs}) \tag{13}$$

where $F(\mathbf{m})$ is the forward model that produces the predicted data, $\mathbf{d}^{obs}$ is the observed data and W is the data-weighting matrix (ideally the data weighting matrix is the inverse covariance matrix of the errors). We assume independent, gaussian errors, so that the data-weighting matrix is diagonal with entries $W_{ii} = 1/\sigma_i^2$. The objective function may then be rewritten as

$$\phi(\mathbf{m}) = \frac{1}{2} \sum_{i=1}^{N} \left[\frac{F_i(\mathbf{m}) - \mathbf{d}_i^{obs}}{\sigma_i} \right]^2 = \frac{1}{2} \sum_{i=1}^{N} r_i(\mathbf{m})^2 \tag{14}$$

where $r_i(\mathbf{m})$ is the i-th normalized residual, and we are assuming that there are N observations.

Inversion method

We use the interior-reflective Newton method (Branch et al., 1999) to find the best fitting model parameters. The algorithm is a trust region method which means that the vector $\mathbf{s}_k$ that updates the current model, i.e.,

$$\mathbf{m}_{k+1} = \mathbf{m}_k + \mathbf{s}_k \tag{15}$$

is chosen from a quadratic model of the objective function within a region where this model can be trusted (hence the term trust region method). A quadratic approximation to $\phi(\mathbf{m})$ is

$$\phi(\mathbf{m}_k + \mathbf{s}_k) \approx \phi(\mathbf{m}_k) + \nabla\phi(\mathbf{m}_k)\mathbf{s}_k + \frac{1}{2}\mathbf{s}_k^T\nabla^2\phi(\mathbf{m}_k)\mathbf{s}_k \tag{16}$$

For a least squares problem we have

$$\nabla\phi(\mathbf{m}) = J^T(\mathbf{m})\mathbf{r}(\mathbf{m}) \tag{17}$$

where J is the Jacobian matrix which expresses the gradient of the residuals with respect to each model parameter,

$$J_{ij}(\mathbf{m}) = \frac{\partial r_i(\mathbf{m})}{\partial m_j} \tag{18}$$

and the Hessian matrix, H, is given by

$$H(\mathbf{m}) = \nabla^2\phi(\mathbf{m}) = J^T(\mathbf{m})J(\mathbf{m}) + \sum_{i=1}^{N}\mathbf{r}_i(\mathbf{m})\nabla^2\mathbf{r}_i(\mathbf{m}) \tag{19}$$

The Hessian can be difficult to calculate because it requires second-order derivatives. In least-squares problems a Gauss-Newton approximation is often used, whereby the second term in the above equation is ignored. This is a good approximation when the residuals are small and means that the Hessian can be obtained essentially for free once the Jacobian has been calculated.

The trust region method involves finding the $\mathbf{s}$ (we drop the subscripts denoting iteration number and the dependence on $\mathbf{m}$ for clarity), that satisfies

$$\min\left\{\frac{1}{2}\mathbf{s}^T J^T J\mathbf{s} + \mathbf{s}^T J^T\mathbf{r}\right\} \quad \text{such that} \quad \|D\mathbf{s}\| \leq \Delta \tag{20}$$

where D is a diagonal scaling matrix and Δ is a positive scalar that controls the trust-region size. Without the trust region constraint the solution of the above equation can be found from the normal equations

$$J^T J\mathbf{s} = -J^T\mathbf{r} \tag{21}$$

The usual trust-region approach is the Levenburg-Marquart algorithm (Marquardt, 1963) where we solve

$$(J^T J + \lambda I)\mathbf{s} = -J^T\mathbf{r} \tag{22}$$

The positive parameter λ ensures that the solution meets the constraint $\|D\mathbf{s}\| \leq \Delta$ and also improves the condition number of the normal equations.

Instead of minimizing Equation (20) over the full space, the algorithm we use minimizes over a two-dimensional subspace, span$(\mathbf{s}_1, \mathbf{s}_2)$. The first basis of the subspace is chosen as the steepest descent direction

$$\mathbf{s}_1 = -J^T \mathbf{r} \tag{23}$$

and the second is obtained by applying preconditioned conjugate gradients (PCG) to Equation (21). The PCG iterations are terminated when a negative curvature direction is discovered, i.e.,

$$\mathbf{s}_2^T J^T J \mathbf{s}_2 < 0 \tag{24}$$

or until the residual is sufficiently small; this would be an approximate Gauss-Newton step. The philosophy behind the method is to force global convergence (by the steepest descent or negative curvature) while still achieving rapid local convergence (by the Gauss-Newton step).

Bounds on model parameters

The Interior-reflective Newton Method allows bounds to be placed on the model parameters by the user if they are required. We typically impose bounds on the spatial location of the dipole, e.g.

$$-2 < x < 2,\ -2 < y < 2 \text{ and } -4 < z < 0 \tag{25}$$

but do not bound the dipole moment or dc-shift. With lower and upper bounds of $[l_i, u_i]$, the minimization problem of Equation (12) is changed to

$$\min_{\mathbf{m} \in \Re^n} \{\phi(\mathbf{m}) :\ l_i \leq m_i \leq u_i\} \tag{26}$$

This constrained minimization problem can be solved using a modification of the formulation presented above (Branch et al., 1999).

Starting model

Due to the possible presence of local minima it is important to obtain a good first guess of the model parameters. To achieve this goal, we use the approach of McFee and Das (1986), whereby the dipole parameters are analytically obtained from the z-component of the vector field. Typically, the data available comprise the total-field and we first need to estimate the z-component. Most anomalies from ordnance have peak amplitudes of less than 1,000 nT, whereas the Earth's field is on the order of 50,000 nT. The anomalous total field ΔB_t is then approximately,

$$\Delta B_t \simeq \alpha_x \Delta B_x + \alpha_y \Delta B_y + \alpha_z \Delta B_z \tag{27}$$

where $\boldsymbol{\alpha} = (\alpha_x, \alpha_y, \alpha_z)$ is a unit vector in the direction of the Earth's field and $\boldsymbol{\Delta B} = (\Delta B_x, \Delta B_y, \Delta B_z)$ is the vector magnetic anomaly. Almost all of the continental USA and Canada has inclinations exceeding 60^o so that $\alpha_z > 0.85$ and to a first approximation

$$\Delta B_z \simeq \frac{\Delta B_t}{\alpha_z} \tag{28}$$

In regions where the z-component of the field is not so dominant, ΔB_z can be obtained from ΔB_t using well known Fourier transformation techniques (Blakely, 1996).

The McFee and Das (1986) technique involves first locating the maximum and minimum values of the field. Then

- The line joining these two points gives the azimuth of the dipole;
- The distance between the two points is related to the depth of the dipole;
- The locations of the extremum and their relative amplitude can be used to infer the horizontal location (assumed to lie on the line joining the points);
- The relative amplitudes of the extremum are related to the dipole dip angle;
- The maximum anomaly amplitude is proportional to the dipole magnitude; and
- Comparing the fit of the dipole to the observed data, estimates the dc-shift.

For a nearly vertical dipole there is only a well defined maximum (or minimum). In that case, the maximum gives the horizontal location, the half-width relates to the depth and the maximum amplitude scales with the magnitude of the vertical dipole.

Data weighting matrix

For the least-squares data fitting, we weight each data-point d_i^{obs}, with an estimate of the standard deviation at that point, σ_i, through the data-weighting matrix,

$$W_{ii} = \frac{1}{\sigma_i^2} = \frac{1}{(\epsilon + \gamma |d_i^{obs}|)^2} \tag{29}$$

The parameter γ is a percentage error that down-weights the influence of the large data values; typically we chose $1\% \leq \gamma \leq 5\%$. The parameter ϵ ensures that the denominator in the above equation does not get too close to zero when d_i^{obs} approaches zero; typically we choose $\epsilon \sim 1$ nT.

Model parameter scaling

If different model parameters have significantly different scale lengths and typical values (e.g. position ~ 1 m; dipole moment ~ 0.01 Am^2), then small favorable changes in some model parameters may be hidden by the large changes required in others. The ideal is to have a non-dimensionalized model space, where unit changes in each model parameter have about the same impact on the objective function. We therefore scale each model parameter by dividing by the following values,

$$\mathbf{x}_{typ} = (1, 1, 1)\text{m}, \; \mathbf{m}_{typ} = (0.1, 0.1, 0.1)\text{Am}^2 \text{ and } d_{typ} = 5 \text{ n}T \tag{30}$$

4 Application of the inversion method

Currently, the inversion algorithms are implemented in Matlab and comprise part of a GUI driven toolbox for geophysical processing developed at The University of British Columbia. Anomalies are first identified in a data-set using a combination of automatic and manual interpretation. Then, the inversion algorithm is applied to a user specified area about each anomaly (typically around 2×2 m^2 to 3×3 m^2). The algorithm is terminated when the objective function decreases by less than a specified tolerance, or when the gradient falls below a specified value. Both these parameters are user controlled.

Summary reports can be generated, and the results visually inspected as demonstrated in Figure 6. We will illustrate the performance of the inversion algorithm on a large magnetics survey collected as part of an clearance project in the Helana Valley, Montana.

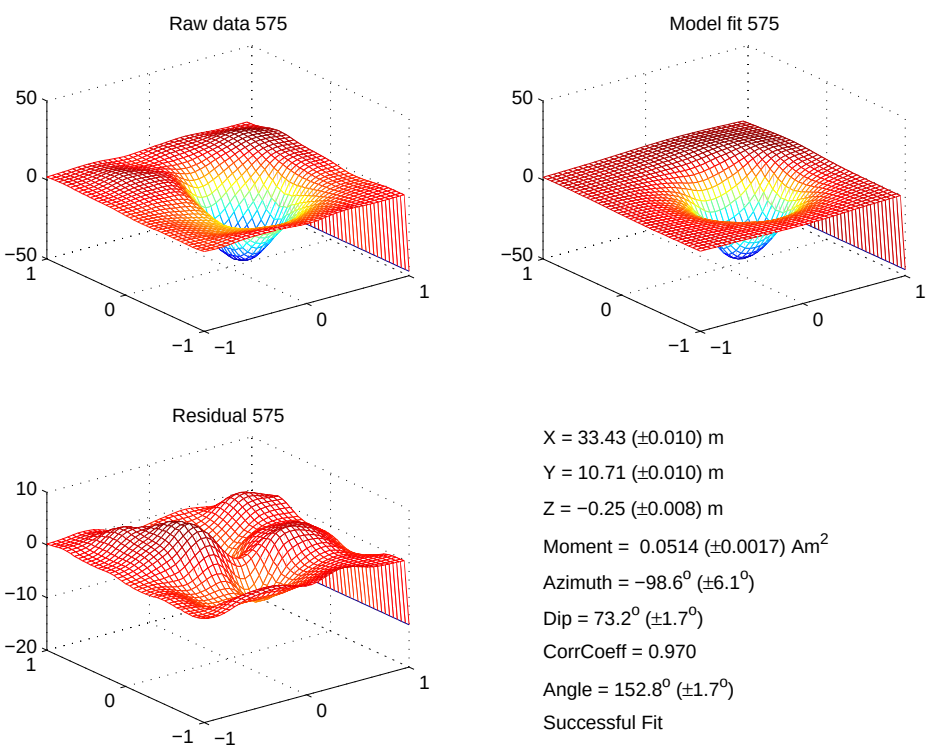

Figure 6: Example result of dipole moment inversion; the numbers in brackets are the estimated standard deviations of the recovered parameters. *Azimuth* and *Dip* refer to the orientation of the dipole in geographic coordinates, while *Angle* is measured between the dipole moment and the Earth's field.

Figure 7: Some of the 81-mm mortars recovered at Guthrie Rd.

The Guthrie Road, Montana dataset

Once open fields, portions of the Helena Valley were used in the 1950s for military training by Montana Army National Guard (MTARNG). The National Guard Bureau funded the remediation project which was divided into two phases focusing on different impact areas: Diamond Springs and Guthrie Road. We consider the data collected in the Guthrie Road area in the summer of 1998. G-tek Australia, conducted a magnetometer survey of the area using an all-terrain vehicle towing an array of eight cesium vapor magnetometers (Clark et al., 1999). The system was equipped with a real-time global positioning system that allowed anomalies to be positioned to within about 20 centimeters.

G-tek found 840 anomalies that were tagged as potential UXO, and these were excavated in the summer of 1999. We analyze 822 of the anomalies (we couldn't locate the data for the remaining 18 anomalies). Table 2 partitions the dig-sheet identifications into six categories; 76-mm projectiles, 81-mm mortars, large pieces of ordnance, shrapnel, metallic debris and geology (including anomalies where no metallic items were found).

A selection of the 81-mm mortars recovered at Guthrie Rd are shown in Figure 7. Most are intact and have not been substantially deformed by the force of impact. However, there are a number of deformed but intact items. These tend to have been practice rounds that were deformed when the black spotter charge detonated on impact. There are also a number of items that have been split into pieces, these were not classified as UXO.

We fitted dipole moments using a percentage error of $\gamma = 5\%$ and a base error of $\epsilon = 1$ nT. The entire run of inversions took around $\frac{1}{2}$ hour on a fairly standard desktop

computer (Pentium Pro Processor with 800 MHz processor and 1 Gb RAM). We use the correlation coefficient c between fitted and observed data to determine the goodness of fit. We found that 85, or around 10% of anomalies had fits with $c < 0.7$ and 162, or around 20% had $c < 0.8$. A break-down according to the dig-sheets of the failed fits is given in Table 2. Most of the failed fits are from items identified as shrapnel, geology or metallic debris, with only one ordnance item having a failed fit. We did not visually inspect every failure, but those we did inspect generally had some type of data issue. These included overlapping acquisition lines that we couldn't remove without undue effort; levelling problems between adjacent lines; and overlapping anomalies. In no case did the inversion algorithm fail where the data quality was good. In the next sections we will describe methods for discrimination and identification and apply them to this data-set.

	76-mm	**81-mm**	**Large pieces**	**Shrapnel**	**Metal**	**Geology**	**Total**
All items	34	49	19	217	377	126	822
Failed fits	0	1	1	13	41	29	85

Table 2: Number of items found during excavation, and the number of fits with $c < 0.7$ (failed fits)

5 UXO Discrimination

The last section described how dipole moments and position are fit to each anomaly. If the data-fit is unsatisfactory the anomaly is marked as such and in a production clean-up would be excavated as potential UXO. From the viewpoint of data interpreters, we are unable to provide any reliable information on the target characteristics. On the other hand, if the fit is satisfactory we attempt to use the recovered dipole moment to discriminate UXO's from non-UXO's. For those items classified as potential UXO the additional step of ordnance identification is attempted as described in the following section.

Our method for ordnance discrimination is based on that described earlier in this report, and is due to Nelson et al. (1998). Briefly, the method relies on the following two factors;

1. Shock demagnetization causes the remnant magnetism of an ordnance to be virtually eliminated;

2. The induced magnetization in a spheroid with $e < 7$ is constrained to lie within about 60^o of the Earth's field (Figure 3).

With a recovered dipole moment of $\mathbf{m}$, our discrimination routine is to calculate the angle between it and the Earth's field, $\mathbf{B}_o$,

$$\psi = \arccos\left(\frac{\mathbf{m} \cdot \mathbf{B}_o}{\|\mathbf{m}\|\|\mathbf{B}_o\|}\right) \tag{31}$$

We can never be certain that all remnant magnetization has been erased by the shock of impact. Additionally, non-ordnance items, whether remnantly magnetized or not, may have dipole angles close to the Earth's field. Consequently, it is not possible to make a definitive ordnance/non-ordnance distinction for all anomalies. Our preferred discrimination method is to rank items according to the likelihood they are due to ordnance. We do this on the basis of the angle ψ; the items with smaller ψ are ranked higher up the list. In a clean-up operation one then excavates according to the list. If resources are available to dig 50% of the anomalies then the first 50% of items in the list are excavated. As a quality control measure a certain number of the lower ranked items should also be excavated.

The Guthrie Road, Montana dataset

In Figure (8a) we plot the dipole magnitude and angle relative to the Earth's field of all the non-ordnance anomalies. Most of the dipoles lie within $\pm 90^o$ of the Earth's field but a large number have angles exceeding 60^o. On the other hand, the dipole angles for the ordnance and large ordnance fragments almost all lie within $\pm 60^o$ of the Earth's field Figure (8b). These results indicate that significant shock demagnetization has occurred to the ordnance. There is only one significant outlier, with an angle of around 70^o.

In Figure (9a) we give a normalized histogram of the angles for the different categories of items. There is a clear concentration of ordnance with dipole angles close to the Earth's field (we include the significant sized ordnance fragments in this category).

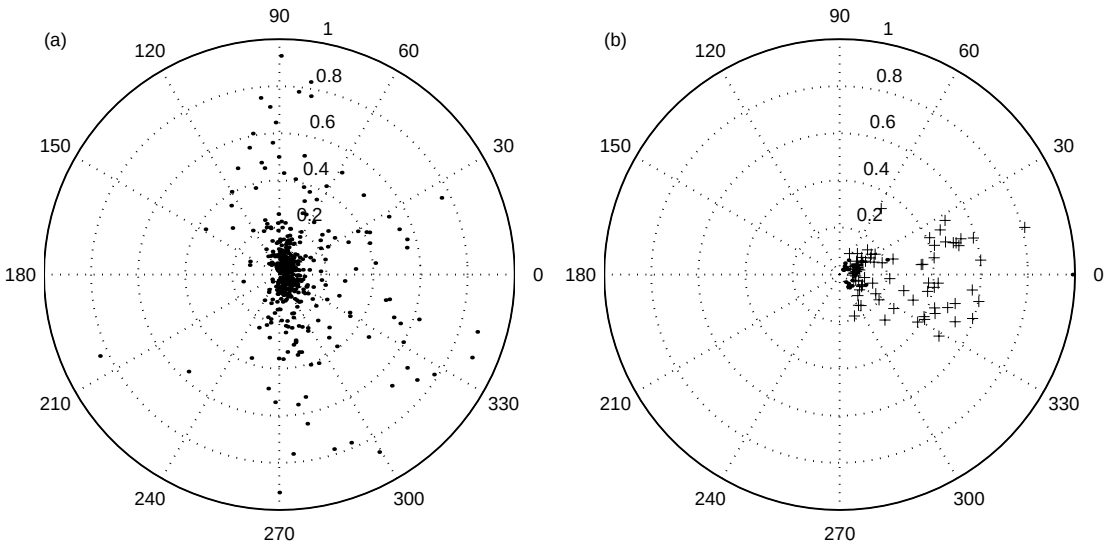

Figure 8: (a) Polar plot of dipole angle and magnitude (Am^2) of non-ordnance items; (b) Same for ordnance (cross) and significant ordnance fragments (dots).

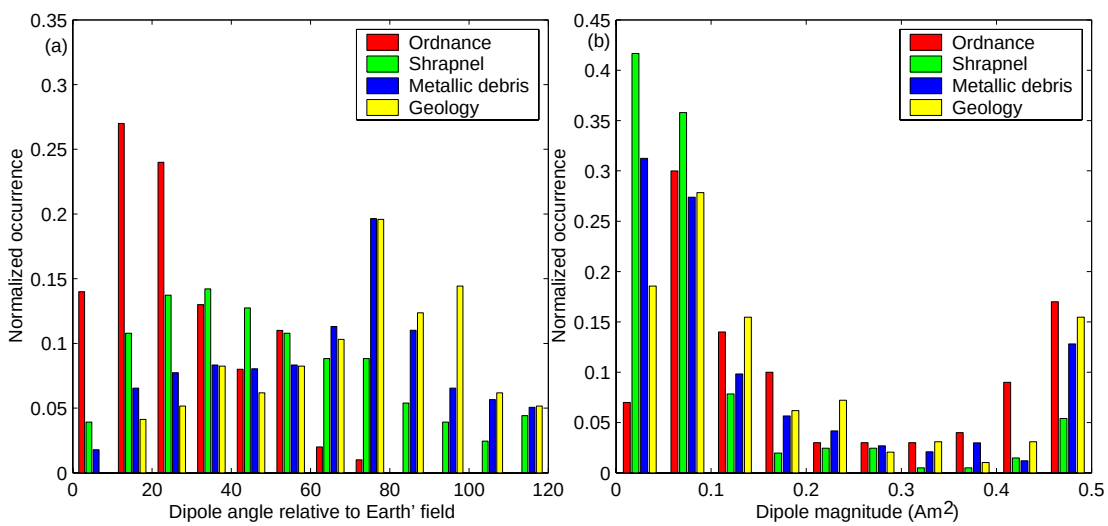

Figure 9: Breakdown of dig-sheets identifications and their (a) dipole angle relative to the Earth's magnetic field; and (b) dipole magntitude.

Shrapnel tends to have relatively low angles, but there are a significant number of items with larger angles. There are two simple mechanisms that could explain this distribution:

1. Shock demagnetization sometimes occurs with shrapnel but not always;

2. Shrapnel acquires a remnant magnetization after impact, in the presence of the Earth's field.

Metallic debris and geological anomalies can have significant remnant magnetism, with a definite peak in the distribution between 60^o and 100^o. We can think of no plausible explanation for this peak in the distribution of dipole angles.

Angle	Dig	Leave	Ordnance found	Ordnance missed	False alarms
55	449	373	78	5	371
60	485	337	81	2	404
65	522	300	82	1	440
70	553	269	82	1	471
75	605	217	83	0	522

Table 3: Guthrie Road discrimination results for intact ordnance items. Discrimination used the dipole angle only.

Angle	Dig	Leave	Ordnance found	Ordnance missed	False alarms
55	449	373	91	11	358
60	485	337	99	3	386
65	522	300	101	1	421
70	553	269	101	1	452
75	605	217	102	0	503

Table 4: Guthrie Road discrimination results, including large pieces of ordnance items. Discrimination used the dipole angle only.

The results of discrimination using different cut-off angles, for intact ordnance items are summarized in Table 3, and for ordnance items and large fragments in Table 4. The tables give the number of items to dig (including the 85 anomalies with poor fits), the number left in the ground, the ordnance found, the ordnance left and the number of false alarms. Figure (10) plots the proportion of items recovered versus the number of holes that need to be excavated. Once the 85 anomalies with poor fits have been dug, there is a high yield of ordnance as the number of holes increases. However, once about 80% of items have been recovered there is a noticeable slow-down in the ordnance yield; a lot of holes need to be dug to recover the last few ordnance items. A total of 560 (68%) of holes are required to recover all ordnance items; this number also recovers all the large ordnance pieces.

Many of the dipole fits for shrapnel and metallic debris have moments with low magnitude (Figure 9b). None of the intact ordnance items has a dipole magnitude less than 0.05 Am^2. However, seven of the large ordnance fragments have dipole moments less than this value. The results of rejecting items as non-ordnance based on the dipole magnitude (as well as a cutoff angle of 75^o) are summarized in Tables 5 (for ordnance only) and 6 (for large fragments as well). With a dipole cutoff of 0.05 Am^2 no intact ordnance items are missed and we can leave 379 items in the ground (46% saving). If we make the reasonable assumption (for this area) that the smallest item likely to be found is a 60-mm mortar, the 0.05 Am^2 cutoff is quite sensible; the minimum dipole moment expected from a 60-mm mortar is around 0.055 Am^2. Ranking items by their magnitude results in a lower initial yield of ordnance (Figure 10) than ranking them by angle. However, the magnitude ranking does not suffer as significant a slow-down in yield, with a crossover occurring once about 80% of items have been recovered. A total of 443 (54%) holes need to be excavated to recover all the ordnance.

One additional discrimination method is examined. It uses the idea of remnant magnetism and requires information on the ordnance items likely to be found in the area. For the Guthrie Rd data we assume that 60 and 81-mm mortars and 76, 90, 105 and 155-mm projectiles may be present in the area and we use the ordnance dimensions

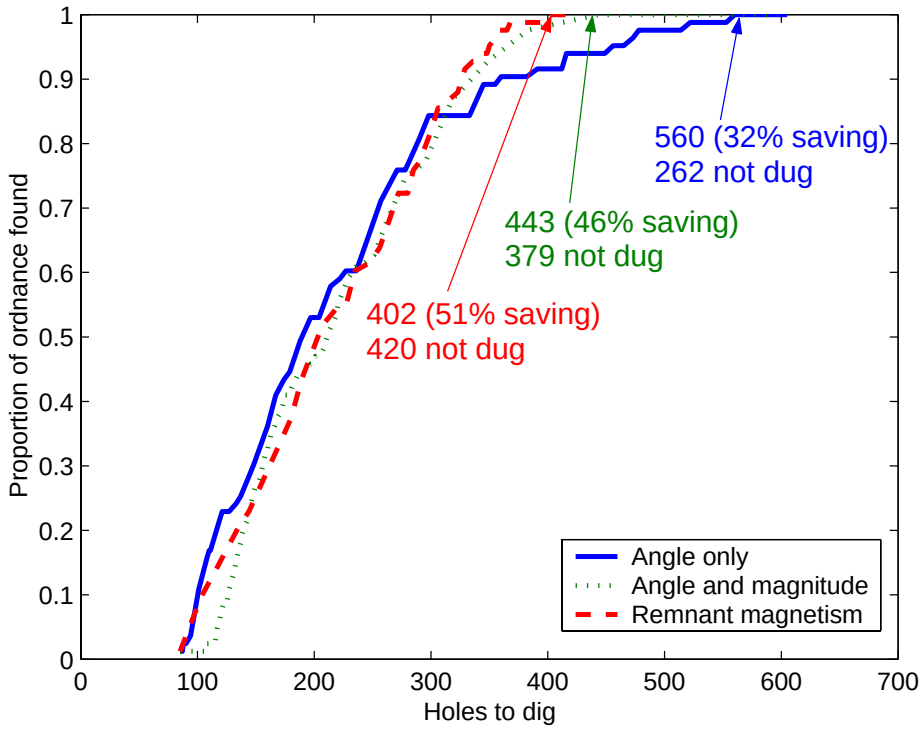

Figure 10: Yield of ordnance with number of holes dug for the three discrimination methods. For all methods it is assumed the 85 anomalies with poor fits are excavated first.

Mag. (A/m)	Dig	Leave	Ordnance found	Ordnance missed	False alarms
0.06	383	439	81	2	302
0.05	443	379	83	0	360

Table 5: Guthrie Road discrimination results for intact ordnance items. Discrimination used the dipole angle (75^o) and magnitude.

listed in Table 7. The method is described in more detail in the next section. Briefly, we determine the minimum percentage of remnant magnetization required to make the recovered dipole moment match of the ordnance items. We then rank the items according to the percentage of remnant magnetism, with lower percentages higher up the list. The method does not apply to large ordnance fragments as these are not considered in our modelling.

The results of discriminating by remnant magnetism are summarized in Table 8. Note, that we also incorporate the angle constraint ($< 75^o$) and the magnitude constraint (> 0.05 Am^2). Allowing up to half of the dipole anomaly to be due to remnant magnetization, we can identify all ordnance items and leave 420 anomalies in the ground (51% saving). The ordnance versus number of holes curve for remnant magnetization (Figure 10) reveals a high yield of ordnance with increasing number of excavations. There is only a very slight slowdown in yield once about 95% of ordnance items have been found. Once 402 (49%) of anomalies are excavated all ordnance items are recovered.

Mag. (Am^2)	Dig	Leave	Ordnance found	Ordnance missed	False alarms
0.06	383	439	90	12	293
0.05	443	379	95	7	348
0.04	493	329	98	4	395
0.03	558	264	100	2	458
0.02	597	225	102	0	495

Table 6: Guthrie Road discrimination results, including large pieces of ordnance items. Discrimination used the dipole angle (75^o) and magnitude.

Item	Diameter (mm)	Aspect ratio
60-mm mortar	60	3.78
76-mm projectile	76	3.57
81-mm mortar	81	3.54
90-mm projectile	90	5.0
105-mm projectile	105	3.71
155-mm projectile	155	4.0

Table 7: Ordnance sizes used for the Guthrie Road identification results.

Remnant (%)	Dig	Leave	Ordnance found	Ordnance missed	False alarms
10	228	594	46	37	182
20	306	516	71	12	235
30	350	472	79	4	271
40	384	438	82	1	302
50	415	407	83	0	332

Table 8: Guthrie Road discrimination results for intact ordnance items. Discrimination used the dipole angle (75^o), magnitude (< 0.05 Am^2) and remnant magnetism.

6 Ordnance identfication

Identification using the recovered dipole moment

For those anomalies classified as potential ordnance, the next step is to try to identify the ordnance type. We established in Appendix B and an earlier part of the report that a given dipole anomaly could have been produced by an infinite number of spheroids (Figure 5). However, for any given site, there are only a finite number of ordnance types that are likely to be found. This is the key observation that allows us to identify ordnance type in the presence of ambiguity.

The dipole induced in a spheroid depends on the angle between the spheroids semi-major axis and the Earth's field. There is no azimuthal dependence due to symmetry. As the ordnance is rotated about the Earth's field the induced dipole moment will trace out a curve such as that shown in Figure (4). This represents all dipole moments that can be produced by the given ordnance item in the absence of remnant magnetism. This mapping procedure can be repeated for all ordnance items suspected of occurring in the area. With N_o ordnance items, a series of curves, $\{\mathbf{m}_k(\theta),\ k = 1, \ldots, N_o\}$, will be generated. For a particular recovered dipole moment $\mathbf{m}$, we calculate the minimum distance between it and each of the dipole curves

$$\Delta m_k = \min_{0 \le \theta < 2\pi} \|\mathbf{m} - \mathbf{m}_k(\theta)\| \tag{32}$$

We assume that any discrepancy is due to remnant magnetism which, as a percentage of the observed moment, will be

$$\gamma_k = 100 \frac{\Delta m_k}{\|\mathbf{m}\|} \tag{33}$$

This allows us to rank the ordnance items according to the likelihood they produced the observed anomaly. The most likely item is that with the lowest percentage remnant magnetism.

The success of the procedure will depend on;

1. The accuracy of the recovered dipole moment (see the error analysis section);
2. The orientation of the ordnance, because some orientations produce dipoles that are close to dipoles potentially produced by other ordnance items;
3. How closely the spheroid approximation matches that for real ordnance; and
4. How much remnant magnetism the ordnance maintains after the shock of impact.

The Guthrie Road, Montana dataset

The dipole moments for those anomalies due to 76-mm projectiles are shown in Figure (11a) and for 81-mm mortars in Figure (11b). Misidentifications for both types of ordnance appear likely due to the overlapping curves for the difference ordnance types. In particular the moments for almost all the 76-mm projectiles are in a region where the

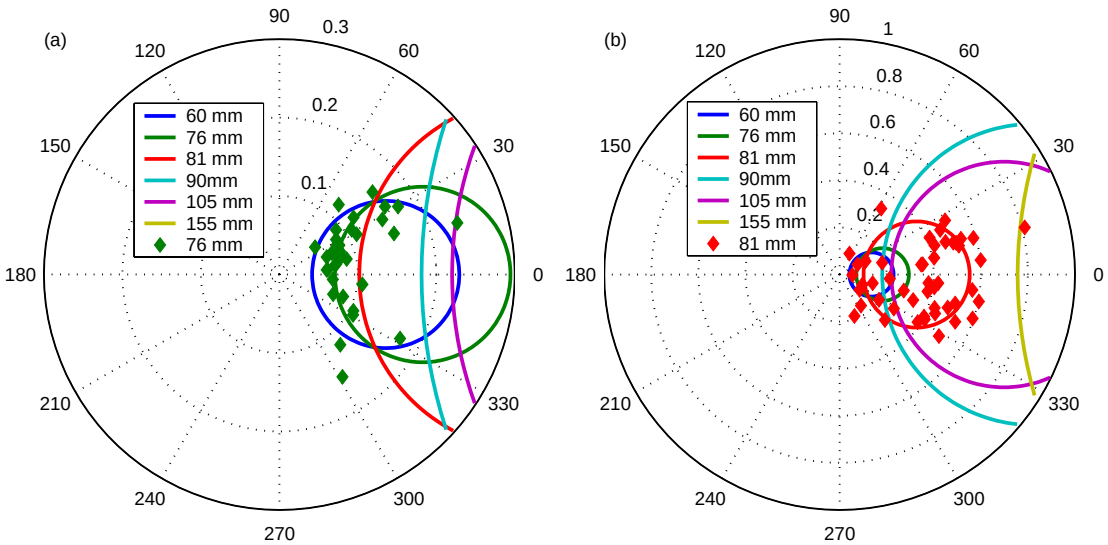

Figure 11: Dipole moments of the Guthrie Road ordnance items for (a) 76-mm projectiles; and (b) 81-mm mortars.

60, 76 and 81-mm calibre ordnances have similar dipole moments. For the 81-mm mortars about half the moments are in a region with only the curve for the 81-mm nearby, while the other half are in the more complex part of the plot. Our dipole identification routine involves finding the ordnance curve that is closest to each recovered moment.

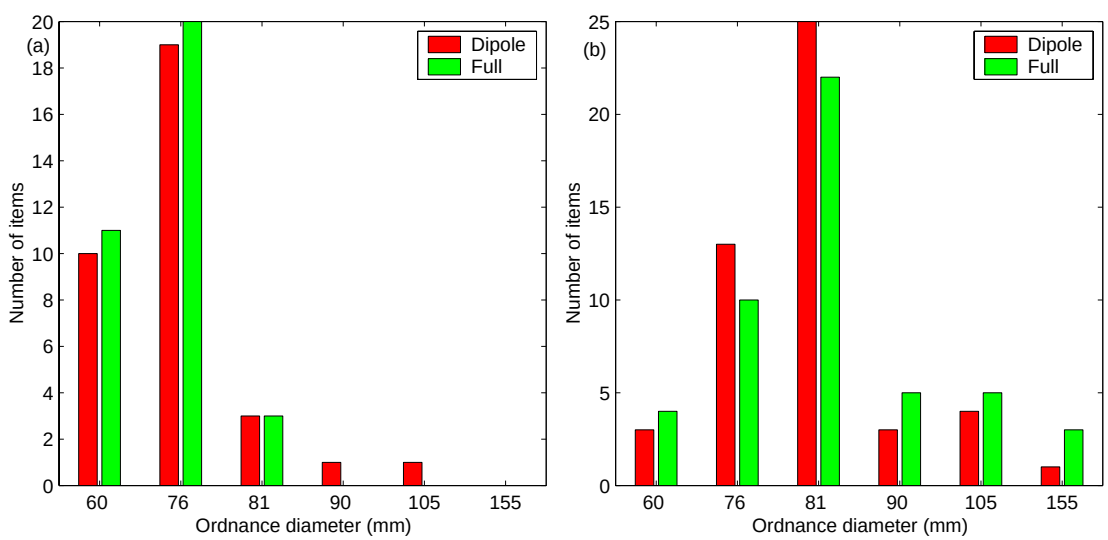

Figure 12: Identification results for the Guthrie Road data using both the dipole and dipole plus octupole methods for (a) 76-mm projectiles; and (b) 81-mm mortars.

Dipole identification results for 76-mm projectiles are given in (Figure 12a) and for 81-mm mortars in Figure (12b). In 19 out of 34 cases (56%) the 76-mm projectile is identified correctly. The most common case of misidentification is as a 60-mm mortar; from Figure (4) we see that this is due to overlapping moments between the 60 and 76-mm ordnances. For 81-mm mortars the identification routine is correct in 25 of 48 cases (52%), so that overall we achieve correct identifications 54% of the time.

Figure 13: One of the practice 81-mm mortars deformed due to the detonation of the spotting charge.

The most common misidentification for the 81-mm mortar is as a 76-mm projectile (13 times). Some of the errors in misidentification could relate to the deformation of certain of the 81-mm practice mortars that occurred when the spotter charge detonated (Figure 13). A spheroid is unlikely to give a very good approximation to this item. Unfortunately, while recovered ordnance items were retained after excavation no records of the anomaly number were kept. Thus, we cannot determine which recovered dipole moments correspond to deformed ordnance.

Assuming we are using the remnant magnetization method for discrimination and use a cutoff of 50%, there will be 235 false alarms; items incorrectly identified as ordnance. Applying the identification method to these false alarms (Figure 14a) is most likely to cause a misidentification as a 60-mm mortar (the moments are generally quite low). Metallic debris is more likely to give a false identification as a large ordnance item than any of the other categories of items (shrapnel, large ordnance pieces and geology).

Seeded test site at The Former Fort Ord, California

The former Fort Ord is located near Monterey Bay in northwestern Monterey County, California. Since 1917, portions of Fort Ord were used by Army units for maneuvers, target ranges, and other purposes. Investigation and ordnance removal actions have been conducted at the former Fort Ord since 1994 when the base closed. In November 1998, the United States Department of the Army instigated an Ordnance Detection and Discrimination Study (ODDS) at Fort Ord (Asch and Staes, 2001).

The purpose of the Seeded Test was to evaluate the detection and discrimination capabilities of selected geophysical instruments when ordnance items are buried or "seeded" below the ground surface in a local site-specific geologic conditions. The seeded test area consists of five separate, adjacent grids, which were cleared of anomalies to pro-

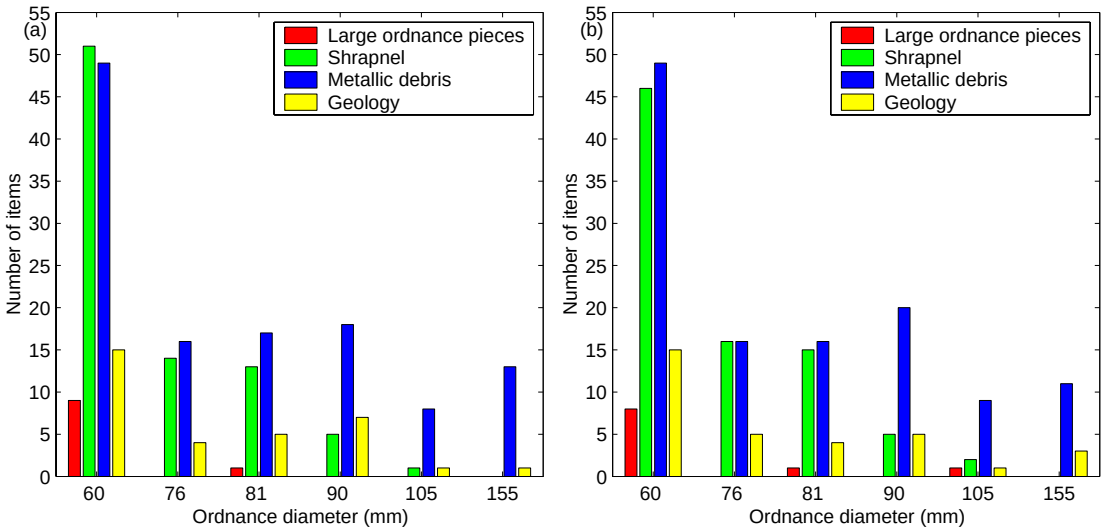

Figure 14: Identification results for the Guthrie Road data for (a) dipole method; and (b) dipole plus octupole method.

vide a controlled testing environment. Two grids are "known" plots where the items, depths and orientations of items are made known to all participants. It is these two known sites (K1 and K2) that we analyze here.

Seventeen different types of ordnance items were buried in the seeded test plots. Some ordnance scrap and other items were also seeded to allow evaluation of discrimination capabilities. Additional areas of the plots were excavated and back-filled without any buried items.

For K1, 5 of the 7 "empty hole" items (618, 619, 621 to 623) did not produce acceptable fits, so they would not have been declared as potential ordnance. The other two "empty holes" had poorly fitting dipoles and would have been identified as scrap. A fragment (595) and a signal illumination flare (612) also produced unacceptable fits.

Discrimination and identification results for the remaining items are summarized in Table 9. Note, that the column marked *Interp* lists the first choice interpretation for each item (e.g. scrap, 22 mm projectile, 60 mm ordnance etc). The column marked *Rank* shows where the actual ordnance item was ranked. For instance, consider the 2.36" rockets. If the *rank* was 1 then the item was identified correctly as a 2.36" rocket (e.g. anomaly 613). If the *rank* was greater than 1 (say 3), then the 2.36" rocket was ranked as the third most likely cause of the anomaly (e.g. anomaly 602).

Two of the four fragments were correctly identified as non-ordnance (using a discrimination cutoff of 60^o). Six of the twelve 35-mm projectiles were incorrectly classified as scrap; this may be due to remnant magnetism. Five of the remaining 35-mm projectiles had the correct identification ranked as one of the top three choices. One of the 2.36" rockets was classified as scrap, the other three had a 2.36" identification ranked in the top three (one was correct). The six signal illumination flares could not be identified correctly, neither could any of the grenades. Overall, the discrimination/identification results for K1 are not very impressive. We believe part of the reason could be due to remnant magnetism (the items were not shock demagnetized prior to emplacement). It may also be a reflection of the generally poor performance of magnetics for small calibre items (Klaff et al., 2002).

Number	Item	z_a (m)	z_r (m)	c	Angle	Interp	Rank
620	Empty Hole	0.00	0.47	0.79	127.4	Scrap	
617	Empty Hole	0.00	0.29	0.75	97.0	Scrap	
599	Fragment	0.30	0.92	0.88	86.1	Scrap	
598	Fragment	0.30	0.62	0.90	114.4	Scrap	
597	Fragment	0.15	0.28	0.97	48.8	Signals	
596	Fragment	0.30	0.41	0.91	55.2	22 mm	
616	35-mm	0.61	0.56	0.93	74.0	Scrap	
608	35-mm	0.46	0.23	0.85	59.0	22 mm	2
607	35-mm	0.30	0.23	0.82	150.1	Scrap	
606	35mm	0.15	0.25	0.98	33.6	37-mm	6
605	35-mm	0.46	0.95	0.91	52.4	Signals	3
604	35-mm	0.61	1.50	0.81	65.3	Scrap	
603	35-mm	0.15	0.37	0.90	55.2	22 mm	2
600	35-mm	0.30	0.43	0.86	68.8	Scrap	
593	35-mm	0.61	0.53	0.92	38.0	22 mm	3
592	35-mm	0.30	0.44	0.97	87.1	Scrap	
591	35-mm	0.61	0.34	0.95	105.6	Scrap	
590	35-mm	0.46	0.38	0.96	37.5	60-mm mortar	2
613	2.36" rocket	0.61	0.65	0.96	57.1	Rocket 2 .36"	1
602	2.36" rocket	0.46	0.59	0.98	55.1	Signals	3
594	2.36" rocket	0.61	0.89	0.96	50.8	Rocket 3 .5"	4
586	2.36" rocket	0.61	2.79	0.96	118.2	Scrap	
615	Signals	0.15	0.26	0.97	39.7	37-mm	2
614	Signals	0.30	0.61	0.82	82.6	Scrap	
611	Signals	0.15	0.33	0.89	43.3	22 mm	3
589	Signals	0.30	1.08	0.89	20.1	22 mm	8
588	Signals	0.30	1.51	0.95	31.6	81-mm mortar	6
610	Hand grenade	0.15	0.08	0.93	49.9	22 mm	12
609	Hand grenade	0.30	0.58	0.77	38.6	22 mm	12
587	Hand grenade	0.30	0.88	0.99	121.5	Scrap	
601	Rifle grenade	0.46	1.33	0.78	77.9	Scrap	

Table 9: Fort Ord identification results for K1, where z_a is the actual burial depth, z_r is the recovered depth, c is the correlation coefficient between observed and predicted data and *angle* is the angle between the Earth's field and the recovered dipole moment.

For the K2 plot, good dipole fits could not be obtained for four items, 555, 556 (both, 25-mm projectiles at 46 cm), 569 (fragment at 30 cm) and 574 (signals at 30 cm). The results for the rest of the items are summarized in Table 10. There were seventeen items correctly identified as ordnance. Six of these were identified as the correct ordnance type and five others had the correct ordnance listed in the top three possibilities. The other six identifications were a long way off and we believe that several of these were remnantly magnetized; in particular all the stokes mortars and the hand grenade.

Identification using the dipole and octupole

Magnetic anomalies from ordnance are usually dominated by the dipole component; however, with high quality data we may be able to obtain useable information from the octupole term. Due to the dipole dominance it would probably not be a good idea to attempt a direct inversion for ordnance dimensions (local minima, non-uniqueness etc). Rather, a better method is to obtain an optimum fit for each ordnance item in

Number	Item	z_a (m)	z_r (m)	c	Angle	Interp	Rank
565	Fragment	0.15	0.14	0.93	92.1	Scrap	
566	Fragment	0.30	0.34	0.98	113.5	Scrap	
567	Fragment	0.15	0.14	0.95	52.3	22 mm	
568	Fragment	0.30	0.28	0.89	37.3	37-mm	
578	Fragment	0.15	0.22	0.92	32.5	60-mm mortar	
579	Fragment	0.30	1.82	0.86	90.1	Scrap	
581	Fragment	0.30	0.57	0.90	36.4	22 mm	
580	25-mm	0.61	0.59	0.82	72.1	Scrap	
553	35-mm	0.61	0.67	0.95	29.1	35-mm	1
559	35-mm	0.61	0.77	0.89	33.2	75-mm	8
575	35-mm	0.30	0.26	0.97	154.0	Scrap	
563	37-mm	0.46	0.20	0.81	55.6	22 mm	3
583	37-mm	0.61	0.93	0.85	47.7	35-mm	5
584	37-mm	0.61	1.03	0.89	61.8	Scrap	
554	2.36" rocket	0.61	0.89	0.97	21.6	90-mm	9
558	2.36" rocket	0.61	0.81	0.94	49.5	105-mm	3
564	75-mm	0.76	0.67	0.96	12.6	75-mm	1
572	75-mm	0.91	1.85	0.86	85.6	Scrap	
560	Signals	0.30	0.50	0.81	124.4	Scrap	
576	Signals	0.15	0.16	0.95	99.8	Scrap	
573	3" Stokes	1.02	0.63	0.86	60.0	35-mm	10
577	3" Stokes	1.02	1.22	0.89	19.2	155-mm	2
585	3" Stokes	0.91	0.66	0.87	16.2	35-mm	9
561	81-mm	0.91	1.13	0.96	39.5	81-mm mortar	1
571	81-mm	0.91	0.85	0.94	34.8	90-mm	2
557	90-mm	0.76	0.82	0.97	21.3	90-mm	1
570	90-mm	0.76	0.73	0.97	20.2	90-mm	1
562	105-mm	1.22	1.16	0.94	59.7	Rocket 2.36"	3
582	105-mm	1.22	1.50	0.96	17.8	105-mm	1
552	Hand grenade	0.30	0.44	0.92	44.4	Signals	12

Table 10: Fort Ord identification results for K2, where z_a is the actual burial depth, z_r is the recovered depth, c is the correlation coefficient between observed and predicted data and *angle* is the angle between the Earth's field and the recovered dipole moment

our library, and declare the ordnance with the best fit as the most likely source of the anomaly. For each item in the library this procedure involves determination of six model parameters $(x, y, z, \theta, \phi, d)$, where (x, y, z) is location, θ is the ordnance dip angle relative to horizontal, ϕ is the azimuth angle relative to geographic North and d is the dc-shift.

We again use a least-squares formulation and the interior-reflective Newton method. The data-weighting and parameter bounds are identical to that used for the dipole inversion (i.e. we only bound the spatial location). For scale factors we use

$$\mathbf{x}_{typ} = (1, 1, 1)\text{m}, (\theta_{typ}, \phi_{typ}) = (\pi/2, \pi/2)\ radians\ and\ d_{typ} = 5\text{n}T \tag{34}$$

To determine the starting model, we first do a dipole inversion and go through the dipole identification process. For each ordnance item, the identification process will return the dip angle θ and azimuth ϕ that achieved the closest fit to the dipole. These can be used as the starting orientation with the dipole location used as the starting location, similarly for the dc-shift. Rather than doing an inversion for every item in the library we only consider those 3-5 ordnance items with the best dipole fits.

The Guthrie Road, Montana dataset

We only apply the dipole/octupole identification procedure to those anomalies flagged as potential UXO by the remnant magnetization technique (with a cutoff of 50% remnant magnetism). The quality of the fits obtained for the optimum ordnance were around the same as the dipole fits; sometimes they were slightly worse and sometimes slightly better.

Identification results for the dipole/octupole method for 76-mm projectiles are given in Figure (12a) and for 81-mm mortars in Figure (12b). For 76-mm projectiles the correct identification is achieved for 20 of 34 cases, one better than the dipole method. However, for the 81-mm mortar correct identification is only achieved for 22 of 48 cases, three less than the dipole method.

Misidentification results for false alarms are given in Figure (14b). The distribution of items is very similar to that achieved with the dipole method.

We believe that there are three reasons why the dipole/octupole identification method does not improve the original dipole identification method.

1. The octupole response is quite small and does not provide significant additional constraints on the the geometry;

2. The equivalent spheroid is not an accurate enough approximation of an ordnance item for the octupole contribution to have a positive effect; and

3. The ordnance items are slightly remnantly magnetized which changes the relationship between ordnance orientation and the direction of magnetization.

Identification using the dipole and quadrupole

Thus far, the identification routines we have developed have relied solely on a spheroid model of ordnance. However, this assumption is overly simplistic since most ordnance items do not have that degree of symmetry. In particular, the front and tail ends of ordnance tend to be different: the front is often tapered to provide better aerodynamics and target penetration, while the tail end is often flat (the tails of mortars don't matter because they are usually made of aluminum). Therefore, a more realistic model of ordnance is an axially symmetric body without front-back symmetry; such a body has a multipole expansion with both a dipole term and a non-zero quadrupole term (recall that the quadrupole was zero for a spheroid due to symmetry).

Our intent with this new identification method is to try to use the information in the quadrupole to constrain the orientation of the body (ϕ, θ). As we discovered when using the dipole method, the principal source of ambiguity in identification is our inability to constrain the orientation of the body. In particular, when the object's dimension is changed, one can compensate by changing the object orientation and produce the same or a very similar dipole moment. If we could constrain the orientation then we could better constrain the ordnance dimension.

The basis of the idea is that there will be no quadrupole contributions perpendicular to the axis of symmetry but there will be contributions along the symmetry axis. We therefore construct a model with these characteristics and use an inversion procedure to recover a model with the best orientation. Concomitant with this process we also recover parameters that depend on the shape of the body, as we now explain.

The dipole moment of an axially symmetric body can be written in the form,

$$\mathbf{m} = \mu_o^{-1}\mathbf{A}^T\mathbf{F}\mathbf{A}\mathbf{B_o} \tag{35}$$

where $\mathbf{A}$ is the usual Euler rotation tensor and $\mathbf{F}$ is a 3×3 diagonal matrix with (F_2, F_2, F_3) along the diagonal. We are assuming axial-symmetry so that $F_1 = F_2$. The demagnetization factors, F_i, given in the above equation, are VF_i times those previously given in Equation 2, where V is the volume of the body. These volume modified demagnetization factors contain all the information on the body's dimensions that we are attempting to recover.

We are assuming the body is axially symmetric (about the z-axis), therefore the quadrupole tensor components in the x-y plane are zero (see Appendix A for a derivation). The body is asymmetric about the x-y plane so that the quadrupole tensor has non-zero components in the z-direction. The tensor is symmetric $\hat{\mathbf{M}}_q = \hat{\mathbf{M}}_q^T$ and is therefore defined by the equation,

$$\hat{\mathbf{M}}_q = \begin{bmatrix} 0 & 0 & m_{q1} \\ 0 & 0 & m_{q2} \\ m_{q1} & m_{q2} & m_{q3} \end{bmatrix} \tag{36}$$

where m_{q1}, m_{q2} and m_{q3} are dependent on the shape and magnetization of the body. The above equation is in body-centered coordinates. The quadrupole tensor may be rotated into the Earth's frame of reference using the following equation,

$$\mathbf{M}_q = \mathbf{A}\hat{\mathbf{M}}_q\mathbf{A}^T \tag{37}$$

The magnetic field due to this quadrupole tensor can be calculated using Equation (A-11). Ignoring the octupole and any higher order moments, full specification of an axially-symmetric body therefore involves the following 11 parameters

$$[x, y, z, \phi, \theta, F_2, F_3, m_{q1}, m_{q2}, m_{q3}, d] \tag{38}$$

where we have again allowed a dc-shift, d.

To invert for the 11 parameter model we use the same least-squares formulation and Interior-reflective Newton method described previously. The parameter scalings are the same as those given in Equation (34), with the additional parameters scaled as

$$\mathbf{F}_{typ} = (0.01, 0.01)\mathrm{m}^3 \; and \; m_{qtyp} = (0.01, .01, .01)\mathrm{A}m^3 \tag{39}$$

Once the model parameters have been recovered we return to our spheroid model of ordnance and find the object dimensions that reproduce the recovered volume demagnetization factors, F_2 and F_3. This is straightforward because the aspect ratio, e solely determines the ratio F_2/F_3, while the diameter and aspect ratio together determine the magnitudes of F_2 and F_3. On occasion we find that F_2 converges towards zero while F_3 appears to converge to a sensible value. In that case, we fix the aspect ratio at a typical value $3 < e < 5$ and just solve for the diameter.

The Guthrie Road, Montana dataset

We applied the quadrupole inversion method to all 737 anomalies at Guthrie Rd that had good dipole fits. Perhaps self-evidently the fits and correlation coefficients for the dipole/quadrupole model were better than for the dipole model alone. Figure 15

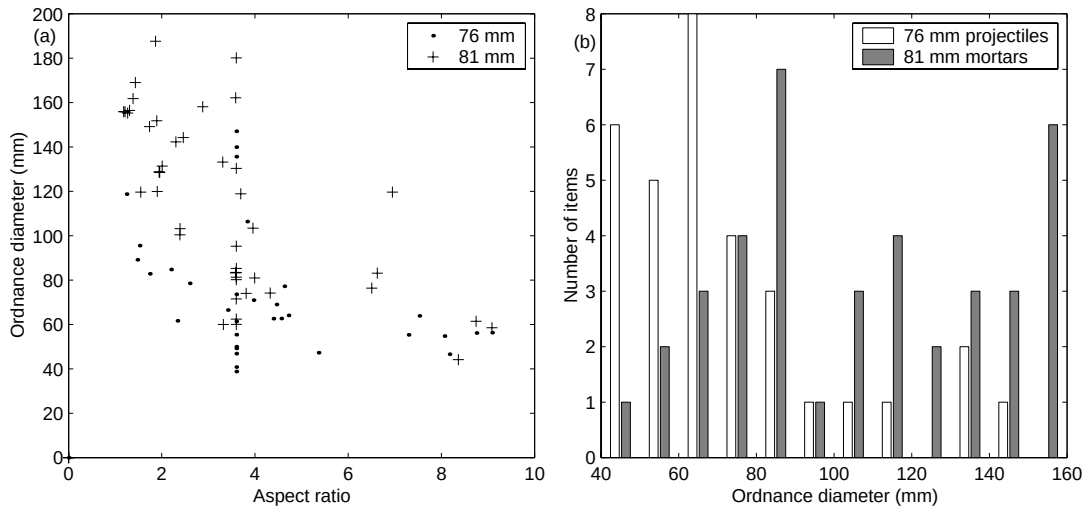

Figure 15: Quadrupole identification results at Guthrie Road; (a) Recovered aspect-ratios and diameters; and (b) Histogram of recovered diameters.

summarizes the results of the quadrupole identification. There appears to be some identification ability but there are a significant number of ordnance items where the recovered dimensions are inaccurate. In particular, there is a tendency to either recover too low an aspect ratio and hence too large a diameter or vice-versa.

There are two conclusions that can be drawn from the quadrupole discrimination results. Firstly, the quadrupole may be unable to provide the required constraints on the ordnance orientation. Alternatively, there may be enough remnant magnetization in the body so that our model is not an accurate reflection of reality.

With these issues in mind we trialed one last method for identification using the quadrupole. This time we allow the dipole moment to vary independently of the quadrupole; i.e. in place of F_1 and F_2 in Equation (38) we solve for $\mathbf{m} = (m_1, m_2, m_3)$. Thus there are twelve parameters to find. Our intent is to determine if unmodelled quadrupole components bias the estimation of the dipole moment.

We applied the method to the Guthrie Road data and then used the recovered dipole moment to achieve ordnance identification in the usual way. We found that the method was slightly inferior to the original dipole identification routine. In particular for the 81-mm mortar 23 of the 48 anomalies were identified correctly (compared to 25 of 48), while for the 76-mm projectile only 16 of 34 cases were correct (compared to 20 of 34). Thus, we conclude that unmodelled quadrupole components do not negatively affect our ability to identify using the dipole moment.

7 Error Analysis

The dipole identification results for Guthrie Road indicate that around 55% of the time we correctly identify the ordnance type. The 45% misidentifications must be due to either an incorrect model, remnant magnetism or uncertainty in the recovered dipole moments. In this section we analyze the uncertainty in recovered dipole moment using linearized error analysis.

Estimating the covariance matrix of the model parameters

To derive the covariance matrix of the model parameters we follow the development given in Bard (1974). At the minimum of the objective function the gradient is zero

$$\nabla\phi(\mathbf{m},\mathbf{d}) = 0 \tag{40}$$

where ∇ is with respect to the model parameters. If we change the data to $\mathbf{d}+\boldsymbol{\delta}\mathbf{d}$ we will change the objective function and hence the position of the minimum will vary to $\mathbf{m}+\boldsymbol{\delta}\mathbf{m}$. The gradient of the new objective function at the new minimum will be zero.

$$\nabla\phi(\mathbf{m}+\boldsymbol{\delta}\mathbf{m},\mathbf{d}+\boldsymbol{\delta}\mathbf{d}) = 0 \tag{41}$$

If we expand this gradient in a Taylor series and only keep first order terms we find

$$\nabla\phi(\mathbf{m}+\boldsymbol{\delta}\mathbf{m},\mathbf{d}+\boldsymbol{\delta}\mathbf{d}) = \nabla\phi(\mathbf{m},\mathbf{d}) + \nabla^2\phi(\mathbf{m},\mathbf{d})\boldsymbol{\delta}\mathbf{m} + \frac{\partial}{\partial\mathbf{d}}\nabla\phi(\mathbf{m},\mathbf{d})\boldsymbol{\delta}\mathbf{d} = 0 \tag{42}$$

Recognizing that the ∇^2 term is the Hessian and rearranging we find

$$\boldsymbol{\delta}\mathbf{m} = \mathbf{H}^{-1}\frac{\partial}{\partial\mathbf{d}}\nabla\phi(\mathbf{m},\mathbf{d})\boldsymbol{\delta}\mathbf{d} \tag{43}$$

The covariance matrix of the model parameters is

$$\mathbf{V}_m = \mathrm{E}[\boldsymbol{\delta}\mathbf{m}\boldsymbol{\delta}\mathbf{m}^T] \tag{44}$$

where $\mathrm{E}[\cdot]$ is the expectation operator. Substituting Equation (43) into (44), recognizing that the Hessian and gradient terms are constants (under expectation) and rearranging terms we find

$$\mathbf{V}_m = \mathbf{H}^{-1}\frac{\partial}{\partial\mathbf{d}}\nabla\phi(\mathbf{m},\mathbf{d})^T\mathrm{E}[\boldsymbol{\delta}\mathbf{d}\boldsymbol{\delta}\mathbf{d}^T]\frac{\partial}{\partial\mathbf{d}}\nabla\phi(\mathbf{m},\mathbf{d})\mathbf{H}^{-1} \tag{45}$$

The covariance matrix of the data is $\mathbf{V}_d = \mathrm{E}[\boldsymbol{\delta}\mathbf{d}\boldsymbol{\delta}\mathbf{d}^T]$. Assuming the data-weighting matrix in our formulation of the inverse problem is the same as the inverse covariance matrix of the data, the Gauss-Newton approximation to the Hessian is

$$\mathbf{H} = \mathbf{J}^T\mathbf{V}_d^{-1}\mathbf{J} \tag{46}$$

while

$$\frac{\partial}{\partial\mathbf{d}}\nabla\phi(\mathbf{m},\mathbf{d}) = \mathbf{V}_d^{-1}\mathbf{J} \tag{47}$$

Substitution of Equations (46) and (47) into Equation(45) and simplification reveals that the covariance matrix is the inverse of the Gauss-Newton approximation to the Hessian,

$$\mathbf{V}_m = (\mathbf{J}^T \mathbf{V}_d^{-1} \mathbf{J})^{-1} = \mathbf{H}^{-1} \tag{48}$$

The above equation can be used to estimate uncertainties in each of the model parameters and can also be used to define confidence ellipses of multiple parameters. The uncertainties obtained through this equation are linearized estimates of the true uncertainties. Before considering them further we investigate how closely these linearized estimates would match fully non-linear estimates. If the minimum of the objective function is $\hat{\mathbf{m}}$ then linearized estimates are equivalent to approximating the objective function with

$$\phi(\mathbf{m}) - \phi(\hat{\mathbf{m}}) \approx \frac{1}{2}(\mathbf{m} - \hat{\mathbf{m}})^T \mathbf{H} (\mathbf{m} - \hat{\mathbf{m}}) \tag{49}$$

If the above equation is a good approximation to the objective function about the minimum then the linearized uncertainties will be accurate estimates of the true uncertainties. We have compared the objective functions of many anomalies and usually find a situation such as that illustrated in Figure (16). The linear and non-linear estimates are very similar for parameters related to the dipole moment, and less so for parameters related to location (especially the depth). From the perspective of ordnance identification it is the uncertainties in the dipole moment that are important, so we can conclude that the linearized estimates should be accurate for our purposes. We note in passing that including the second order terms in the Hessian has very little impact on the accuracy of the linear approximation, even if the residuals at the solution are large. This is readily apparent for the dipole components in cartesian coordinates $\mathbf{m} = (m_x, m_y, m_z)$ because the second derivatives with respect to these parameters are zero (Equation 9).

Confidence ellipses of multiple parameters

We are principally interested in the joint-uncertainty in the dipole magnitude and angle relative to the Earth's field because these two parameters control our decisions on discrimination and identification. A good method for visualizing the joint-uncertainties is to calculate confidence ellipses; these are contours of equal confidence in the model parameters. They are usually defined to encompass a certain probability that the model lies within the defined region. For instance, a one-sigma (or 68.3%) confidence ellipse would delineate a region that has a 68.3% chance of containing the true model parameters (under the particular statistical assumptions used to define the objective function).

To define the confidence ellipse for r parameters requires that the uncertainties in the other $n - r$ parameters (assuming there are n parameters in total) are projected onto the r-dimensional hyperplane under consideration. In turns out (Bard, 1974) that this projection can be implicitly achieved by calculating the covariance matrix through inversion of the appropriate $r \times r$ subsection of the Hessian matrix. For example, if we are interested in the joint confidence ellipse for parameters 2 and 5 we would calculate

$$\mathbf{V}_m = \begin{bmatrix} H_{22} & H_{25} \\ H_{52} & H_{55} \end{bmatrix}^{-1} \tag{50}$$

The principal axes of the ellipse are then obtained by eigenvalue decomposition of $\mathbf{V}_m$,

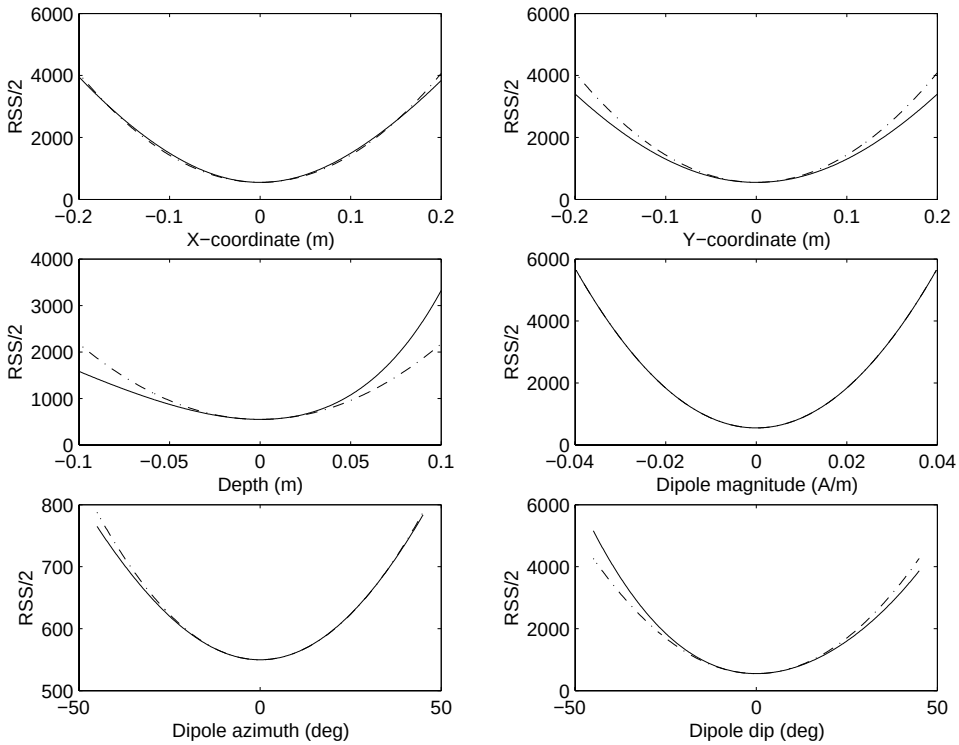

Figure 16: Objective function (solid line) and Gauss-Newton approximation to the Hessian (dashed line) about the inversion solution for Target 575, Fort Ord.

$$\mathbf{V}_m = \mathbf{U}\mathbf{S}\mathbf{U}^T \tag{51}$$

where $\mathbf{S}$ is a diagonal matrix of eigenvalues and $\mathbf{U}$ is an orthonormal matrix of eigenvectors; each eigenvector is a principal axis of the ellipse. The size of each principal axis is given by the reciprocal of the corresponding eigenvalue.

The final step is to find the ellipse that lies on the boundary of a specified confidence region (e.g. 68.3% or the one-sigma error). If the sampling distribution is normal, unbiased and we assume that the covariance matrix $\mathbf{V}_m$ is known, then $(\mathbf{m}-\hat{\mathbf{m}})^T\mathbf{V}_m^{-1}(\mathbf{m}-\hat{\mathbf{m}})$ is χ^2 distributed with r degrees of freedom (Bard, 1974). The boundary of the ellipse corresponding to a particular confidence level is found by calculating the value of the χ^2 distribution with r degrees of freedom that corresponds to that confidence. For example, with 2 degrees of freedom, the 68.3% confidence limit has $\chi^2 = 2.298$. The contour of $(\mathbf{m}-\hat{\mathbf{m}})^T\mathbf{V}_m^{-1}(\mathbf{m}-\hat{\mathbf{m}})$ with the value 2.298 corresponds to the boundary of the 68.3% confidence region.

Alternatively, if the covariance matrix is not known and we assume that all observations are independent (so that $\mathbf{V}_d = \sigma^2\mathbf{I}$) then the confidence level is obtained through the $F_{r,n-r}$ distribution (Bard, 1974). In that case the value of χ^2 calculated above would be replaced with

$$r\sigma^2 F_{r,n-r}(\gamma) \tag{52}$$

where γ is the desired confidence limit ($\gamma = 0.683$ for the 68.3% confidence level) and σ^2 is the sample variance. If the optimum model returned by the minimization routine is $\hat{\mathbf{m}}$ and there are K model parameters then the sample variance is obtained by calculating

$$\sigma^2 = \frac{1}{N-K} \sum_{i=1}^{N} \left[F_i(\hat{\mathbf{m}}) - d_i^{obs} \right]^2 \tag{53}$$

Finally, if the assumption of Gaussian statistics does not hold, conservative confidence limits can be calculated by recourse to the Bienaymê-Chebyshev inequality (Bard, 1974). For the γ confidence limit this replaces the value of χ^2 above with

$$\frac{r}{1-\gamma} \tag{54}$$

The Guthrie Road, Montana dataset

The distribution of residuals for the 660 anomalies at Guthrie Road with correlation coefficients greater than 0.8 are shown in Figure (17). The curves have been normalized so that they have an integral of one; thus we are approximating the posterior probability density function (posterior PDF) of the residuals. The best fitting Gaussian distribution (with $\sigma = 0.99$ nT) provides a poor fit to the residuals. In particular, large residuals are much more likely than predicted by a normal distribution. In Figure (17) we also show the best fitting Ekblom distribution (Ekblom, 1973) which has a probability density function equal to

$$Pr(x) = c \exp \left[\frac{(x^2 + \epsilon^2)^{p/2}}{\sigma^p} \right] \tag{55}$$

where c is a constant that ensures the PDF integrates to unity. This is a perturbed version of an Lp-norm and we found best fitting values of $\sigma = 1.16 \times 10^{-4}$ nT, $\epsilon = 0.609$ nT and $p = 0.224$. The correspondence between the observed distribution of residuals and the Ekblom PDF is excellent. We will consider the good fit of the Ekblom PDF further in the discussion section of this report.

As the residuals are clearly non-Gaussian, we must be cautious when interpreting confidence ellipses calculated under the normality assumption. The shape and relative size of the ellipses are likely to be correct but their absolute values are probably incorrect (i.e. the 68.3% confidence ellipse won't correspond to a confidence of 68.3%). However, the absolute confidence ellipses should provide a rough estimate of the uncertainties in the parameters. They should also provide a reliable means of comparison of the uncertainties in recovered parameters for different anomalies.

We calculated confidence ellipses for the dipole magnitude and angle relative to the Earth's field, for the anomalies due to 76-mm projectiles and 81-mm mortars at Guthrie Road (Figure 18). The data-weighting matrix was the identity matrix, with a sample standard deviation calculated from the residuals by Equation (53). The figures show the one-sigma (68.3%) and two-sigma (95.4%) confidence ellipses about each recovered dipole moment (assuming Gaussian statistics). For the 76-mm projectiles all except one anomaly have very small uncertainties. The one outlier was incorrectly identified as a 105-mm projectile. For the 81-mm mortars all anomalies have very small uncertainties.

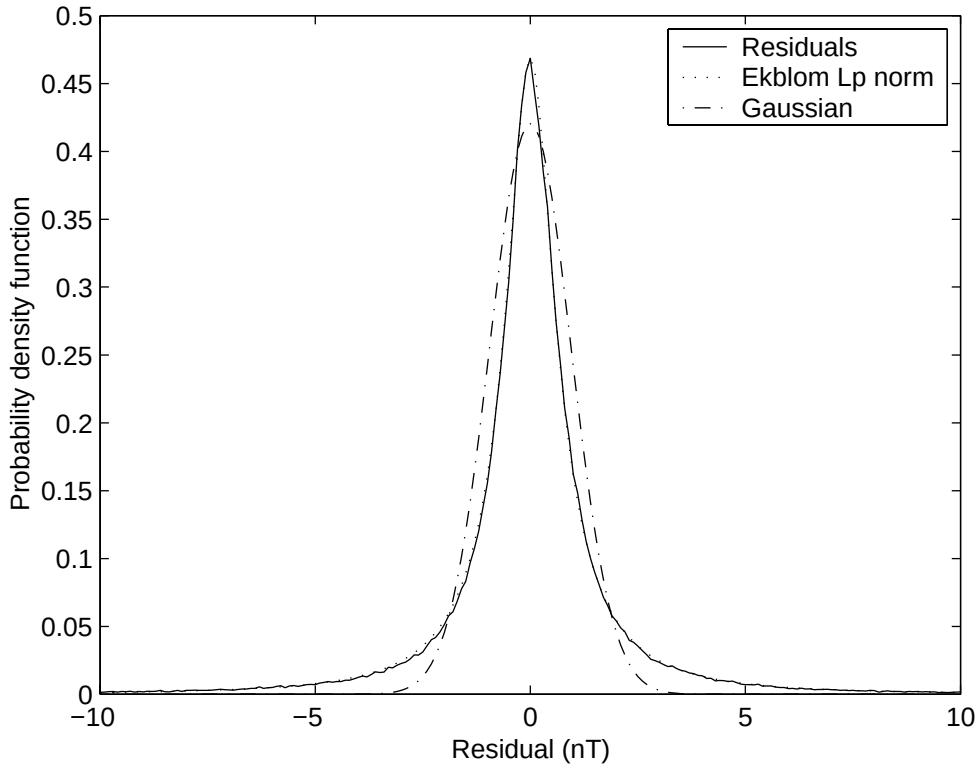

Figure 17: Distribution of residuals for the 660 anomalies at Guthrie Rd with correlation coefficient greater than 0.8.

We also calculated confidence ellipses using the very conservative Bienaymê-Chebyshev inequality (Figure 19). The confidence ellipses are significantly larger than those returned under the normal assumption. If the real confidence ellipses were this large, then uncertainty in the recovered moment would be a contributing factor in misidentifications (especially for 76-mm projectiles). However, the real confidence ellipses would have a size intermediate between the Gaussian and Bienaymê-Chebyshev estimates. This would imply that misidentification is sometimes, though probably not that often, caused by uncertainty in the recovered moment. Misidentifications are more likely to occur due to modelling deficiencies and/or remnant magnetization.

We also calculated confidence ellipses (under the normal assumption) for the anomalies due to metallic debris and geology (Figure 20). For the metallic debris many of the uncertainties are quite low but there are a few items with much higher uncertainties. For the anomalies due to geology the uncertainties are generally much higher. In many cases the recovered angle is around 60^o but the uncertainty is high. This is a critical area for making discrimination decisions so we can conclude that, for geological anomalies, uncertainty in dipole angle can have a significant impact on discrimination.

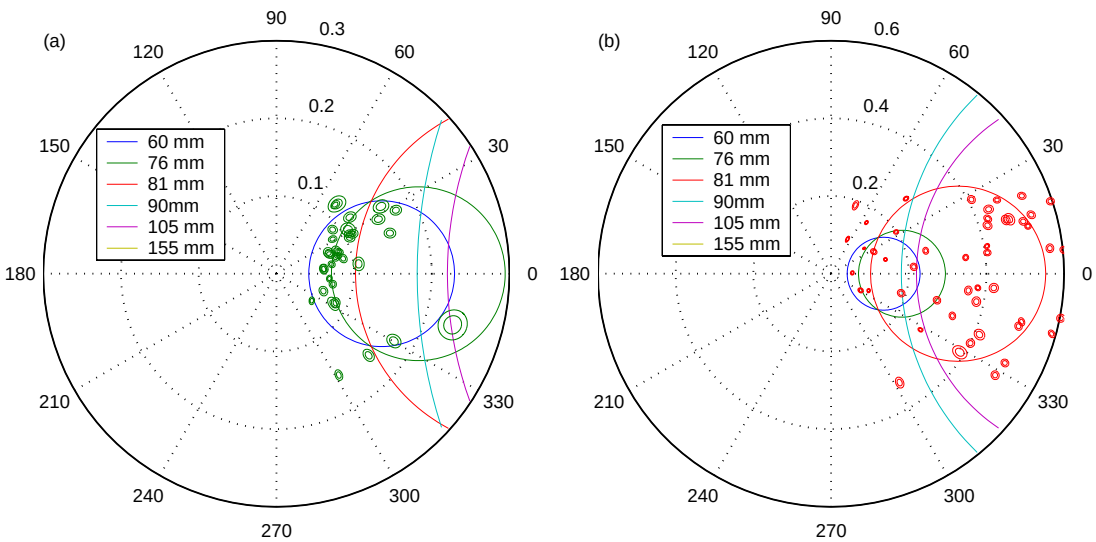

Figure 18: One sigma (68.3%) and two sigma (95.4%) confidence ellipses, assuming Gaussian statistics, about the recovered dipole moments for (a) 76-mm projectiles; and (b) 81-mm mortars.

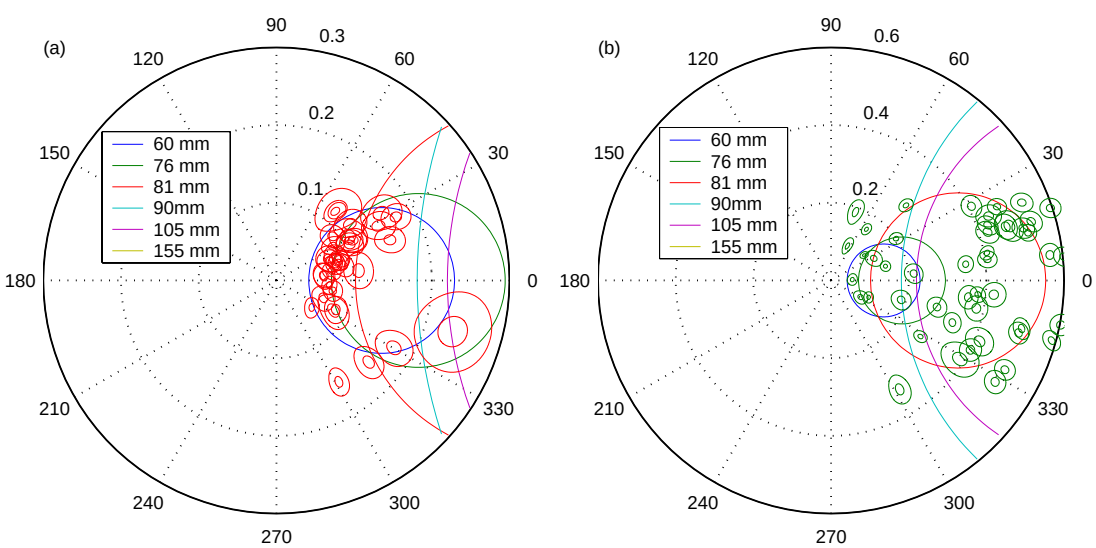

Figure 19: Worst case scenario for one sigma (68.3%) and two sigma (95.4%) confidence ellipses about the recovered dipole moments for (a) 76-mm projectiles; and (b) 81-mm mortars.

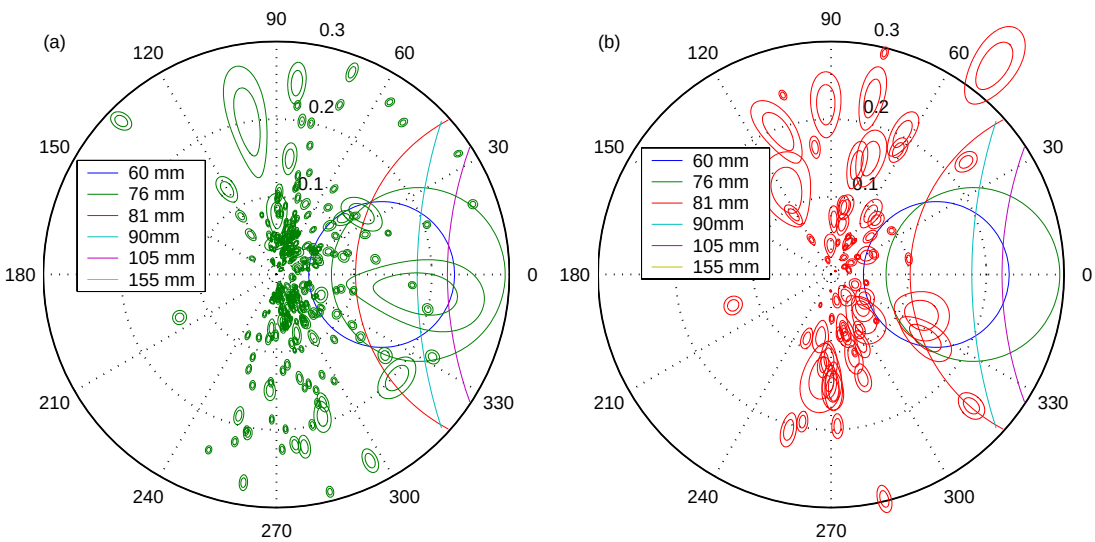

Figure 20: One sigma (68.3%) and two sigma (95.4%) confidence ellipses about the recovered dipole moments for (a) metallic debris; and (b) geological anomalies.

8 Discussion

In this report we have described a successful inversion method for recovering the position and dipole moment from a total-field magnetic anomaly. The inversion uses a least-squares formulation and an interior-reflective Newton method to minimize the objective function. A starting model is defined using an analytical method based on approximating the vertical component of the magnetic field. The inversion method is very fast and reliable; our Matlab implementation requires only a few seconds to recover the parameters for each anomaly.

The recovered dipole moments can be used to make discrimination decisions by recourse to the phenomena of shock demagnetization. Complete shock demagnetization may not occur for all ordnance items all the time. Additionally, non-ordnance, even though they may be remnantly magnetized, might be orientated so that their dipole moments lie close to the Earth's field. This means that it is not possible to make a definitive ordnance/non-ordnance decision. Rather, we prefer to rank anomalies, with items most likely to be UXO higher up the list. We investigated three such ranking procedures; (i) dipole angle, (ii) dipole angle and magnitude and (iii) percentage of remnant magnetism, and found that the remnant magnetization ranking was the best. With this method all ordnance would have been recovered after only half of the anomalies had been excavated. This included 85 anomalies with poor dipole fits that only yielded one UXO. The criterion used to select potential UXO may need to be revised to minimize the number of anomalies where we are unable to make reliable inferences about the bodies origin.

Linearized error analysis indicates that the angle between the recovered dipole moment and the Earth's field for ordnance items is relatively well constrained. Therefore, uncertainty in the recovered dipole moment is unlikely to strongly influence the discrimination ranking. For items identified as geology, the confidence ellipses were much larger. Consequently, the position of these items in the ranking is strongly influenced by uncertainty.

The discrimination method was very successful at Guthrie Road but could not be reliably applied to the seeded sites at Fort Ord. This is a consequence of remnant magnetization and emphasizes the importance of shock demagnetization to the viability of the method. Additional work needs to be undertaken to determine the circumstances where shock demagnetization occurs. For instance, the recovered dipole moments of several of the 81-mm mortars at Guthrie Road had relatively large dipole angles, indicating the presence of some remnant magnetism. Perhaps the lower impact velocity of mortars compared to artillery projectiles causes only partial shock demagnetization; this needs to be investigated further.

Identification of the ordnance type using the recovered dipole moment is difficult due to non-uniqueness. The dipole moment is the product of volume with the magnetization vector. When the volume changes, self-demagnetization as the orientation of the body is varied can change the magnetization vector and thus produce an identical or similar dipole moment. However, recognizing that there are only a finite number of ordnance types in an given area, makes identification using the recovered dipole moment feasible. At Guthrie Road correct identification could be achieved about 55% of the time.

One of the key factors that influences successful identification is obtaining the correct

trajectory of moment magnitude and angle for a given ordnance item. We use a spheroid approximation to calculate this trajectory. Modelling of shapes that more closely approximate real ordnance should be undertaken in order to determine the reliability of the spheroid approximation.

A significant cause of misidentification is the inability of the dipole moment to constrain the orientation of the causative body. In an attempt to overcome this problem we developed inversion routines that recover information on the quadrupole and octupole components of the body. The dipole/octupole method we developed uses a spheroid approximation of ordnance to estimate both the dipole and octupole moments. No significant improvement in identification over the dipole method was found. This could be due to one or more of the following: (i) remnant magnetization; (ii) rapid falloff of the octupole component with distance so that it is unable to constrain the orientation; and (iii) the spheroid provides a poor approximation to the octupole moment of real ordnance.

The quadrupole method relaxed the requirement of top-bottom symmetry enforced by a spheroid approximation and attempted to recover the dipole and quadrupole moments of an arbitrary axially symmetric body. The fits to the data were improved slightly but no advantages for identification were realized. The cause is likely due to one or more of the following: (i) remnant magnetization; (ii) the inability of the quadrupole component to constrain the orientation; and (iii) inadequacy of the model.

The failure of the quadrupole and octupole methods to improve identification may imply that analysis of magnetic data alone does not provide enough information to constrain the objects orientation. One possible method to provide this constraint is by joint inversion of magnetic and electromagnetic data; either single or multiple channel time domain EM or frequency domain EM. Most EM sensors illuminate the target from multiple directions and are consequently more sensitive to orientation (in contrast the direction of the Earth's field is fixed). In return, the magnetics may provide valuable depth constraints that are difficult to obtain with EM alone (Pasion and Oldenburg, 2001).

Linearized error analysis was used to estimate individual parameter uncertainties and joint confidence ellipses. The linear approximation provides an accurate model of the objective function about the minimum. However, the residuals do not follow a Gaussian distribution so that reliable confidence ellipses could not be defined. Additionally, the upper bound provided by the Bienaymê-Chebyshev inequality is very conservative and probably returns confidence ellipses that are much larger than required. A recommendation for future work is to attempt to calculate confidence ellipses using non-Gaussian statistics.

The residuals were found to follow an Ekblom distribution, yet we minimized a measure derived from Gaussian statistics. A reformulation of the problem using an Ekblom distribution as a measure of data misfit is therefore recommended. The resulting objective function would need to be solved by a different optimization algorithm than the one used here. Algorithms for the solution of this optimization problem are well known and include iteratively reweighted least squares and Newton's method (Watson, 1980; Ekblom, 1987). Implementation of the new optimization method would enable a thorough investigation to be made on the influence the choice of the measure of data misfit has on the recovered model. This is an issue often glossed over when solving inverse problems and this report was no exception.

9 Conclusions and Recommendations

A dipole inversion method was developed and successfully applied to the discrimination and identification of magnetic anomalies at Guthrie Road Montana. The discrimination method had the potential to reduce the number of excavations by half, yet still yielded all the ordnance. Identification of the causes of the anomalies is difficult using the recovered dipole moment due to non-uniqueness. However, by recognizing that there are a finite number of ordnance types, correct identification could be achieved in about 55% of cases. Extension of the inversion method to recover either quadrupole of octupole moments did not improve our ability to discriminate or identify.

We recommend the following areas as directions for future research.

1. Shock demagnetization: The extent to which this phenomena occurs should be investigated further because shock demagnetization is central to the success of discrimination using magnetic data.

2. Magnetic modelling of ordnance: The trajectory of the modelled dipole moment magnitude and angle determines our identification decisions. Therefore, the agreement between the moments returned by a spheroid approximation and a more realistic ordnance shape should be investigated further.

3. Joint inversion of magnetics and electromagnetics: Identification difficulties in magnetics are caused by an inability to constrain the orientation of the causative body. The ability of time or frequency domain electromagnetics to constrain the orientation needs to be investigated. Conversely, magnetics may provide valuable depth information that can be exploited by the EM inversion.

4. Error analysis using non-Gaussian statistics: The residuals do not follow a Gaussian distribution so uncertainty estimates based on a more realistic statistical distribution should be investigated.

5. Robust measures of data misfit: The problem should be reformulated using a more realistic measure of data misfit (the Ekblom norm), and methods implemented to solve the modified inversion problem.

10 Bibliography

Altshuler, T. W., 1996, Shape and orientation effects on magnetic signature prediction for unexploded ordnance: Proc. 1996 UXO Forum, 282–291.

Asch, T., and Staes, E. G., 2001, An Ordnance Detection and Discrimination Study at former Fort Ord, CA: Proc. 2001 UXO Forum.

Bard, Y., 1974, Non-linear parameter estimation: Academic Press.

Blakely, R. J., 1996, Potential theory in gravity and magnetic applications: Cambridge University Press.

Branch, M. A., Coleman, T. F., and Li, Y., 1999, A subspace, interior, and conjugate gradient method for large-scale bound-constrained minimization problems: SIAM J. Sci. Comput., **21**, no. 1, 1–23.

Bulter, D. K., Cespedes, E. R., B.Cox, C., and Wolfe, P. J., September 1998, Multisensor methods for buried unexploded ordnance detection, discrimination and identification:, Technical Report 98-10, SERDP.

Clark, P. J., Donaldson, M. W., and Schwartz, T., 1999, ATV Towed magnetometer system for ordnance detection: Proc. 1999 UXO Forum.

Ekblom, H., 1973, Calculation of linear best Lp approximations: BIT, **13**, 293–300.

Ekblom, H., 1987, The L1-estimate as limiting case of an Lp- or Huber-estimate *in* Dodge, Y., Ed., Statistical data analysis based on the L1-norm and related methods:: Elsevier, 109–116.

FAC, 1996, Unexploded ordnance (UXO); An overview: Federal Advisory Committee for the Development of Innovative Technologies.

GAO, 2001, Environmental liabilities, DoD training range cleanup cost estimates are likely underestimated: United States General Accounting Office, Report to the Chairman, Committee on the Budget, House of Representatives, April 2001.

Klaff, T. L., Asch, T., Murray, C., Cormier, M., Staes, E. G., and Peterson, G., 2002, An evaluation of UXO detection instruments through profile comparisons from the Ordnance Detection and Discrimination study at the Former Fort Ord, CA: Proc. SAGEEP.

Lide, D. R., 2001, CRC hanbook of chemistry and physics: CRC Press, 82 edition.

Marquardt, D., 1963, An algorithm for least squares estimation of nonlinear parameters: SIAM J. Appl. Math., **11**, 431–441.

McFee, J. E., and Das, Y., 1986, Fast non-recursive method for estimating location and dipole moment components of a static magnetic dipole: IEEE Trans. Geosci. Rem. Sens., **24**, 663–673.

McFee, J. E., January 1989, Electromagnetic remote sensing; Low Frequency Electromagnetics:, Technical Report 124, Defence Research Establishment Suffield.

Nelson, H. H., Altshuler, T. W., Rosen, E. M., McDonald, J. R., Barrow, B., and Khadr, N., 1998, Magnetic modeling Of UXO And UXO-like targets and comparison with signatures measured by MTADS: Proc. 1998 UXO Forum, 282–291.

Pasion, L. R., and Oldenburg, D. W., 2001, Characterizing unexploded ordnance using time domain electromagnetic induction:, Technical Report ERDC/GSL TR-01-10, U.S. Army Corps of Engineers, Engineer Research and Development Center.

Putnam, J., 2001, Kaho'olawe program management and technology: Proc. UXO Forum.

Roest, W. E., Verhoef, J., and Pilkington, M., 2001, Magnetic interpretation using the 3-D analytic signal: Geophysics, **57**, 116–125.

Stratton, J., 1941, Electromagnetic theory: McGraw Hill.

Watson, G. A., 1980, Approximation theory and numerical methods: John Wiley.

Youmans, C., and Daehn, L., 1999, Quality assurance and quality control in UXO remediation: A case study from Montana: Proc. 1999 UXO Forum.

Appendix A: Multipole Expansion

In this appendix we give a brief derivation of the multipole expansion of a magnetic body, and in particular derive the equations relevant to a spheroid. Our derivations closely follow those given in McFee (1989).

The scalar potential, $\phi(\mathbf{r})$ of a body with magnetization $\mathbf{M}$ is given by

$$\phi(\mathbf{r}) = \frac{1}{4\pi}\int_V \mathbf{M}\cdot\nabla(\frac{1}{r'})dV \tag{A-1}$$

where r' is the distance from the source to the observation point (Figure 1). Expanding the gradient and using the divergence theorem we find

$$\phi(\mathbf{r}) = \frac{1}{4\pi}\left(\int_S \frac{1}{r'}\mathbf{M}\cdot\mathbf{dS} - \int_V \frac{1}{r'}\nabla\cdot\mathbf{M}dV\right) \tag{A-2}$$

If the induced field inside the body is uniform and parallel (which it is for a spheroid), which eliminates the second term in the above equation because then $\nabla\cdot\mathbf{M}=0$. The multipole method proceeds by expanding $\frac{1}{r'}$ as a Taylor series about the origin,

$$\begin{aligned}\phi(\mathbf{r}) \;=\; & \frac{1}{4\pi r}\int_S \mathbf{M}\cdot\mathbf{dS} + \left[\frac{\partial}{\partial x_i}\frac{1}{4\pi r}\right]\int_s x_i\mathbf{M}\cdot\mathbf{dS} + \\ & \left[\frac{\partial^2}{\partial x_i\partial x_j}\frac{1}{4\pi r}\right]\frac{1}{2!}\int_S x_i x_j\mathbf{M}\cdot\mathbf{dS} + \\ & \left[\frac{\partial^3}{\partial x_i\partial x_j\partial x_k}\frac{1}{4\pi r}\right]\frac{1}{3!}\int_S x_i x_j x_k\mathbf{M}\cdot\mathbf{dS} + ...)\end{aligned} \tag{A-3}$$

where repeated indices imply that summation convention is to be used. The scalar potential from a 2^n pole with moment $m^{(n)}_{ij\ldots}$ is given by the expression

$$\phi^{(2^n)} = \frac{m^{(n)}_{ij\ldots}}{4\pi n!}\frac{\partial^n}{\partial x_i\partial x_j\ldots}\left[\frac{1}{r}\right] \tag{A-4}$$

from which it follows that the first four moments are

$$m^{(0)} = \int_S \mathbf{M}\cdot\mathbf{dS} \tag{A-5}$$

$$m^{(1)}_i = \int_S x_i\mathbf{M}\cdot\mathbf{dS} \tag{A-6}$$

$$m^{(2)}_{ij} = \int_S x_i x_j\mathbf{M}\cdot\mathbf{dS} \tag{A-7}$$

$$m^{(3)}_{ijk} = \int_S x_i x_j x_k\mathbf{M}\cdot\mathbf{dS} \tag{A-8}$$

In order the moments are the scalar monopole $m^{(0)}$, the vector dipole $m^{(1)}$, the rank 2 tensor quadrupole $m^{(2)}$, and the rank 3 tensor octupole $m^{(3)}$. Magnetic monopoles do

not exist which means that the monopole term is zero. Expansion of the dipole term reveals that the dipole moment is the product of the magnetization with the volume,

$$\mathbf{m^{(1)}} = \mathbf{M}V \tag{A-9}$$

Due to the symmetry of the spheroid the quadrupole term is zero. After the dipole, the next non-zero term is the octupole; specification of the octupole components is tedious so we refer the interested reader to McFee (1989).

The magnetic field (in the i-th direction) due to the dipole component is given by the expression

$$B_i^{(1)} = \frac{\mu_o}{4\pi r^3}\left(\frac{3}{r^2}[\mathbf{x}\cdot\mathbf{m}^{(1)}]x_i - m_i\right) \tag{A-10}$$

Although zero for the spheroid we will use the quadrupole term later, its field is,

$$B_i^{(2)} = \frac{3\mu_o}{8\pi r^5}\left(-x_i m_{jj}^{(2)} - x_j(m_{ij}^{(2)} + m_{ji}^{(2)}) + 5r^{-2}x_i x_j x_k m_{jk}^{(2)}\right) \tag{A-11}$$

and for the octupole the field is,

$$B_i^{(3)} = \frac{\mu_o}{8\pi r^5}\left(3m_{ijj}^{(3)} - 15r^{-2}\left[x_i x_j m_{jkk}^{(3)} + x_j x_k m_{ijk}^{(3)}\right] + 35r^{-4}x_i x_j x_k x_l m_{jkl}^{(3)}\right) \tag{A-12}$$

It remains to find the magnetization vector for a spheriod. A solution of the boundary value problem (Stratton, 1941) shows that the demagnetization factors are

$$F_i = \frac{\mu_r - 1}{1 + \alpha_i(\mu_r - 1)/2} \tag{A-13}$$

where μ_r is the relative permeability ($\mu = \mu_r\mu_o$),

$$\alpha_1 = \alpha_2 = \frac{e(e+E)}{e^2-1} \tag{A-14}$$

and

$$\alpha_3 = \frac{-2e(e^{-1}+E)}{e^2-1} \tag{A-15}$$

with

$$E = \frac{\log(e - \sqrt{e^2-1})}{\sqrt{e^2-1}} \tag{A-16}$$

for a prolate spheroid ($e > 1$) and

$$E = \frac{\arctan(\frac{e}{\sqrt{1-e^2}}) - \pi/2}{\sqrt{1-e^2}} \tag{A-17}$$

for an oblate spheroid ($e < 1$). For the special case of a sphere ($e = 1$) then

$$\alpha_1 = \alpha_2 = \alpha_3 = \frac{2}{3} \tag{A-18}$$

The demagnetization factors together with the Earth's field $\mathbf{B_o}$ (in spheroid centered coordinates), determine the strength of the induced magnetization,

$$\mathbf{M} = \mu_o^{-1}\mathbf{F}\mathbf{B_o} \tag{A-19}$$

where we have written $\mathbf{F}$ as a 3×3 diagonal matrix with (F_2, F_2, F_3) along the diagonal (because $F_1 = F_2$).

Multipole expansion for an axi-symmetric body

In going from the general equation (A-2) for a magnetized body to that for a spheroid, we used the fact that the magnetization inside the body was constant so that $\nabla \cdot \mathbf{M} = 0$. For a general axi-symmetric body this is no longer true and there is an extra contribution to each of the moments. For the dipole,

$$m_i^{(1)} = \int_S x_i \mathbf{M} \cdot \mathbf{dS} - \int_V x_i \nabla \cdot \mathbf{M} dV \tag{A-20}$$

and using the identity

$$\int_V \phi \mathbf{M} \cdot \nabla \phi dV = \int_S \phi \mathbf{M} \cdot \mathbf{dS} - \int_V \phi \nabla \cdot \mathbf{M} dV, \tag{A-21}$$

we find

$$\begin{aligned} m_i^{(1)} &= \int_V \mathbf{M} \cdot \nabla x_i dV \\ &= \int_V M_i dV \end{aligned} \tag{A-22}$$

Thus the dipole moment is just the integration of the magnetization over the volume of the body. Most ordnance items are either cylinder like with a pointed front (e.g. most artillery projectiles) or close to a spheroid shape (e.g. mortars, the fins can be ignored as they are usually aluminum). For an infinite cylinder the field lines are constant within the body. Therefore, for a projectile any changes in magnetization will be concentrated at the ends of the body, and will generally make only a small contribution to the multipole moments. For a mortar, the shape is close to second order (Stratton, 1941) and hence the magnetization direction will be approximately constant. Thus, changes in magnetization direction should not make a significant contribution to the observed magnetic anomaly.

Using an analogous development to the dipole, the quadrupole moment can be shown to be equal to

$$\begin{aligned} m_{ij}^{(2)} &= \int_V \mathbf{M} \cdot \nabla (x_i x_j) dV \\ &= \int_V (M_i x_j + M_j x_i) dV \end{aligned} \tag{A-23}$$

Assuming that changes in magnetization can be ignored implies that

$$m_{ij}^{(2)} = M_i \int_L dx_3 \int_{S(x_3)} x_j dS + M_j \int_L dx_3 \int_{S(x_3)} x_i dS \tag{A-24}$$

where L is the length of the body parallel to the symmetry axis, $z = x_3$ and $S(x_3)$ is a slice of the body perpendicular to the axis of symmetry. Due to symmetry each of the integrals over $S(x_3)$ are zero for i or $j = 1$ or 2, from which it follows that

$$m_{ij}^{(2)} = 0 \quad \text{for any } i, j = 1 \text{ or } 2 \tag{A-25}$$

The quadrupole moment is symmetric $m_{ij}^{(2)} = m_{ji}^{(2)}$ so that the full moment tensor can then be written as (where we have dropped the (2) subscript),

$$\mathbf{M} = \begin{bmatrix} 0 & 0 & m_{13} \\ 0 & 0 & m_{23} \\ m_{13} & m_{23} & m_{33} \end{bmatrix} \tag{A-26}$$

Appendix B: Constraints on Dipole Orientation

The angle the induced dipole moment in a spheroid makes with the Earth's field cannot exceed a certain value. In this appendix we derive the equations which specify this upper bound. We assume the Earth's field is at an angle θ to the spheroid symmetry axis and align the z-axis of our coordinate system with the symmetry axis. We can then choose the x-axis so that it is perpendicular to the Earth's field. In this coordinate system

$$\mathbf{b_o} = b_o(0, \sin\theta, \cos\theta)^T \tag{B-1}$$

The spheroid diameter a and aspect ratio e determine the demagnetization factors, F_2 and F_3, so that the induced dipole moment $\mathbf{m}$ is,

$$\mathbf{m} = V\ b_o(0, F_2 \sin\theta, F_3 \cos\theta)^T \tag{B-2}$$

where V is the volume of the spheroid. The angle ψ between the Earth's field and the dipole moment is

$$\cos\psi = \frac{\mathbf{b_o} \cdot \mathbf{m}}{\|\mathbf{b_o}\|\|\mathbf{m}\|} \tag{B-3}$$

which, on substitution of Equations (B-1) and (B-2), becomes

$$\cos\psi = \frac{F_2 \sin^2\theta + F_3 \cos^2\theta}{\sqrt{F_2^2 \sin^2\theta + F_3^2 \cos^2\theta}} \tag{B-4}$$

After differentiating this equation by θ, setting the result to zero and extensive algebraic manipulation we find

$$\theta = \arctan\left(\sqrt{\frac{F_3^3 + F_3 F_2^2 - 2F_2 F_3^2}{F_2^3 + F_2 F_3^2 - 2F_3 F_2^2}}\right) \tag{B-5}$$

This orientation of the spheroid symmetry axis relative to the Earth's field makes the angle between the induced dipole and the Earth's field a maximum. This maximum angle is obtained by substituting Equation (B-5) into Equation (B-4).

Appendix C: Ambiguity in the Dipole Solution

Once the sensor distance exceeds a few body lengths distance away from the spheroid, the field is essentially dipolar. In such cases, inversion for spheroid dimensions has an inherent ambiguity: many different spheroid diameters and aspect-ratios can reproduce the observed dipole. To characterize this ambiguity we chose our coordinate system so that the z-axis is aligned with the Earth's field,

$$\mathbf{B_o} = (0, 0, B_o)^T \tag{C-1}$$

We want to determine if the dipole $\hat{\mathbf{m}}$ from a particular spheroid (diameter a and aspect-ratio e) can match an observed dipole moment $\mathbf{m}$. Now the induced dipole for the spheroid is given by the following equation

$$\hat{\mathbf{m}} = V\mathbf{A}^T\mathbf{F}\mathbf{A}\mathbf{B_o} \tag{C-2}$$

Expanding this equation we find

$$\hat{\mathbf{m}} = \frac{B_o \pi e a^3}{6\mu_o} \begin{bmatrix} (F_2 - F_3)\cos\theta\sin\theta\sin\psi \\ (F_2 - F_3)\cos\theta\sin\theta\cos\psi \\ F_2\cos^2\theta + F_3\sin^2\theta \end{bmatrix} \tag{C-3}$$

Now we want to find a, e, θ and ψ so that $\hat{\mathbf{m}} = \mathbf{m}$. We can find an expression for the spheroid diameter by equating the norms of the two dipole moments, resulting in

$$a^3 = \frac{6\mu_o\|\mathbf{m}\|}{B_o\pi e\sqrt{F_2^2\cos^2\theta + F_3^2\sin^2\theta}} \tag{C-4}$$

For ψ we use,

$$\frac{m_1}{m_2} = \frac{\hat{m}_1}{\hat{m}_2} = \frac{\sin\psi}{\cos\psi} = \tan\psi \tag{C-5}$$

which leads to

$$\psi = \arctan\left(\frac{m_1}{m_2}\right) \tag{C-6}$$

This implies that the spheroid has the same azimuth as the dipole moment.

Determination of θ is a little more difficult. We start by using the second row of Equation (C-3) and substitute in Equation (C-4) for the diameter,

$$\frac{m_2}{\cos\psi\|\mathbf{m}\|} = \frac{(F_2 - F_3)\cos\theta\sin\theta}{\sqrt{F_2^2\cos^2\theta + F_3^2\sin^2\theta}} \tag{C-7}$$

Note that if $\cos\psi = 0$ we would use the first row of Equation (C-3) to derive an equation in terms of m_1 and $\sin\psi$. Let the LHS of Equation (C-7) be ω, expand out the square-root on the denominator of the RHS, and use the substitution

$$\sin^2\theta = 1 - \cos^2\theta \tag{C-8}$$

After some algebraic manipulation Equation (C-7) reduces to

$$(F_2 - F_3)^2 \cos^4\theta \left[\omega^2(F_2^2 - F_3^2) - (F_2 - F_3)^2\right] \cos^2\theta + \omega^2 F_3^2 \tag{C-9}$$

This is a quadratic equation in $\cos^2\theta$ which has a real solution if

$$\Delta = \hat{b}^2 - 4\hat{a}\hat{c} \geq 0 \tag{C-10}$$

where

$$\hat{a} = (F_2 - F_3)^2 \tag{C-11}$$
$$\hat{b} = \omega^2(F_2^2 - F_3^2) - (F_2 - F_3)^2 \tag{C-12}$$
$$\hat{c} = \omega^2 F_3^2 \tag{C-13}$$

The solution in terms of θ is then

$$\theta = \pm \arccos\left(\sqrt{\frac{-\hat{b} \pm \sqrt{\Delta}}{2\hat{a}}}\right) \tag{C-14}$$

The $\pm$ terms in the above equation emphasize that when $\Delta > 0$ there are actually two possible solutions.

Determination of which spheroids can reproduce the observed dipole proceeds as follows. Firstly, we chose an aspect-ratio e and calculate the demagnetization factors in the usual way. We then substitute Equations (C-11) to (C-13) into Equation (C-10) to determine if a solution can be found for this aspect-ratio. If it can, we calculate θ by Equation (C-14), and finally we calculate the spheroid diameters (usually there will be two) by Equation (C-4).